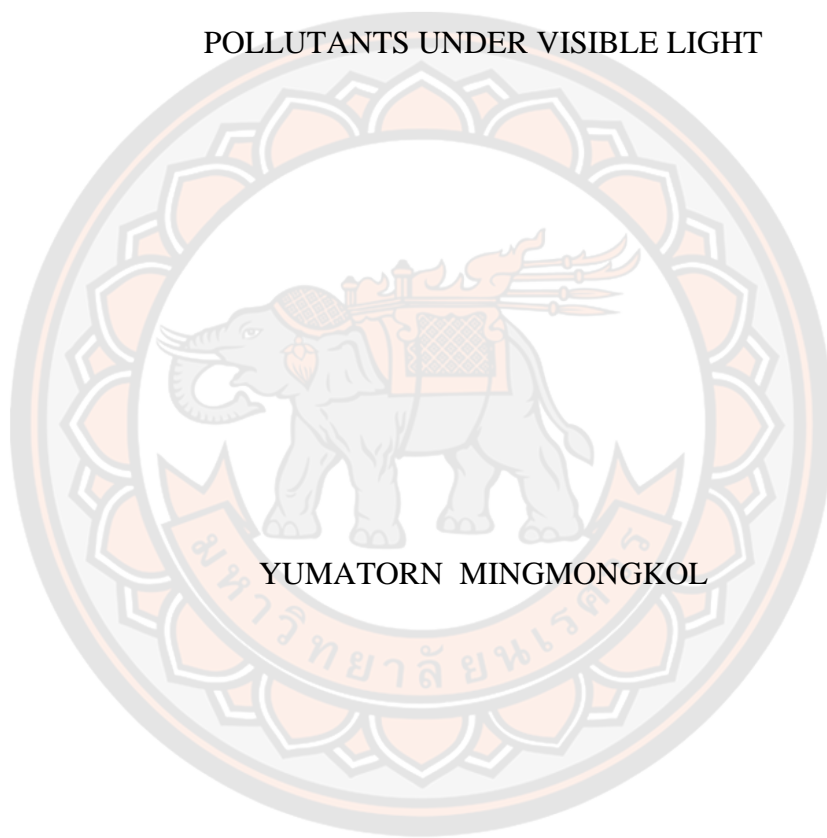




METAL DOPED TiO_2 NANOPARTICLES FOR PHOTODEGRADATION OF
POLLUTANTS UNDER VISIBLE LIGHT



YUMATORN MINGMONGKOL

A Thesis Submitted to the Graduate School of Naresuan University
in Partial Fulfillment of the Requirements
for the Doctor of Philosophy in Environmental Engineering
2022

Copyright by Naresuan University

METAL DOPED TiO₂ NANOPARTICLES FOR PHOTODEGRADATION OF
POLLUTANTS UNDER VISIBLE LIGHT



YUMATORN MINGMONGKOL

A Thesis Submitted to the Graduate School of Naresuan University
in Partial Fulfillment of the Requirements
for the Doctor of Philosophy in Environmental Engineering
2022

Copyright by Naresuan University

Thesis entitled "Metal doped TiO₂ nanoparticles for photodegradation of pollutants under visible light"

By Yumatorn Mingmongkol

has been approved by the Graduate School as partial fulfillment of the requirements for the Doctor of Philosophy in Environmental Engineering of Naresuan University

Oral Defense Committee

..... Chair
(Assistant Professor Khakhanang Ratananikom, Ph.D.)

..... Advisor
(Assistant Professor Wilawan Khanitchaidecha, Ph.D.)

..... Internal Examiner
(Associate Professor Duangdao Channei, Ph.D.)

..... Internal Examiner
(Assistant Professor Pajaree Thongsanit, Ph.D.)

..... Internal Examiner
(Pornnapa Sutawong, Ph.D.)

Approved

.....
(Associate Professor Krongkarn Chootip, Ph.D.)
Dean of the Graduate School

Title	METAL DOPED TiO ₂ NANOPARTICLES FOR PHOTODEGRADATION OF POLLUTANTS UNDER VISIBLE LIGHT
Author	Yumatorn Mingmongkol
Advisor	Assistant Professor Wilawan Khanitchaidecha, Ph.D.
Academic Paper	Ph.D. Dissertation in Environmental Engineering, Naresuan University, 2022
Keywords	TiO ₂ photocatalysts, Copper Oxide, Photocatalytic

ABSTRACT

Dyes are one of the major pollutants that concern around the world, which reduction of light penetration, photosynthetic activity of aquatic plants and dissolved oxygen in the water. The dye molecule itself is toxic to humans and fish and cause for water pollution. Recently, pharmaceutical and hormonal contaminants including paracetamol and antibiotics in the water are continuously increasing which can damage the living organisms via bioaccumulation and food chain. Not only these two pollutants, pathogenic microorganisms are other common pollutants which are found in the environment. The efficient treatment technology is important to improve the water quality and avoid the negative impacts to human and the environment. Since there are many pollutants contaminated in the water, the development of applicable treatment technology for various pollutants removal, simplicity, low cost and energy consumption is concerned in this study.

Among treatment technologies, photocatalysis of titanium dioxide (TiO₂) has a potential process for organic compound removal because of its nontoxicity and inexpensiveness. TiO₂ photocatalysts exhibit the decomposition of organic pollutants and the inhibition of microorganisms in the environment. However, TiO₂ has low utilization of the sunlight spectrum as a wide band gap (anatase: 3.2 eV, rutile: 3.0 eV). This limit needs to improve to enhance photocatalytic performance. Therefore, the aim of this study was to synthesize metal-doped TiO₂ to improve photocatalytic and antibacterial activities. TiO₂ was doped with copper (Cu) and manganese (Mn) in various content of 0.1 to 1.0% and 0.1 to 0.3%, respectively. The Cu-doped TiO₂

nanoparticles were synthesized by hydrothermal method. At the same time, the Mn-doped TiO₂ nanoparticles were synthesized by the sol-gel method. The physico-chemical properties of the synthesized nanoparticles were characterized by X-ray diffractometer (XRD), Brunauer–Emmett–Teller (BET), transmission electron microscopy (TEM), scanning electron microscopic (SEM) and energy dispersive X-ray (EDX). The photocatalysis performance of synthesized nanoparticles on methylene blue (MB) and salbutamol (SAL) degradation were examined. In addition, the antimicrobial activity of the nanoparticles also was observed.

The results revealed that the anatase phase of TiO₂ was well maintained in all undoped and Cu-doped TiO₂ nanoparticles. The crystal sizes were approximately 10 nm and the specific surface areas of the nanoparticles were approximately 180-182 m²/g. The band gap energy slightly decreased from 3.20 eV for undoped TiO₂ to 3.10 for Cu-doped TiO₂. However, the Cu-doped TiO₂ nanoparticles were agglomerated by increasing Cu doping. For MB degradation, the 0.10% Cu-doped TiO₂ obtained the best MB degradation efficiency (approximately 100% under 30 min UV-A irradiation) as similar as P25. The undoped TiO₂ obtained the lowest MB degradation efficiency of 70%. In addition, the best *E. coli* photocatalytic activity was obtained in the 0.1% Cu-doped TiO₂ nanoparticles which completely killed in 180 minutes under UV-A irradiation, whereas the undoped TiO₂ showed the lowest bacterial photokilling activity which many bacterial colony was still observed in 180 minutes under UV-A irradiation. The significant drawback of Cu-doped TiO₂ was that it required UV-A light, was higher energy than visible light, to activate the photocatalytic activity.

On the other hand, the another metal doped TiO₂ was Mn-doped TiO₂. Due to the physico-chemical properties, the anatase and rutile phases were observed on the undoped and Mn-doped TiO₂ nanoparticles. However, the major phase is the anatase phase. The specific surface was enhanced by Mn doping; the 0.1%Mn-doped TiO₂ obtained the highest specific surface area of 120.16 m²/g. The band gap energy of 0.1%Mn-doped TiO₂, 0.2%Mn-doped TiO₂ and 0.3%Mn-doped TiO₂ was 2.91, 2.80 and 2.88 eV which fell in the visible light region. The photocatalytic degradation of MB and SAL was tested under visible irradiation. The best MB removal efficiency

of 97% was obtained in the 0.2% Mn-doped TiO₂ after 60 minutes irradiation, followed by 0.3% Mn-doped TiO₂, 0.1% Mn-doped TiO₂, and undoped TiO₂ nanoparticles. In addition, the highest SAL removal efficiency of 95% was found in the 0.2% Mn-doped TiO₂ after 180 minutes. Moreover, the 0.2% Mn-doped TiO₂ nanoparticles also achieved the best **E.coli** photokilling activity; the complete killing was observed under visible light for 240 minutes whereas some **E.coli** colony was found in undoped TiO₂, 0.1% Mn-doped TiO₂ and 0.3% Mn-doped TiO₂.



ACKNOWLEDGEMENTS

This thesis could not be finished without great help from Asst. Prof. Dr. Wilawan Khanitchaidecha, my thesis advisor, and Assoc. Prof. Dr. Auppatham Nakaruk as well. I am grateful to them for all of their support, information and useful advice, which help me pass through my difficult times. I also thank them for their hard-working and effort in correcting my thesis and encouraging me to complete my work.

I specially thank to the chairperson, Asst. Prof. Dr. Khakhanang Ratananikom, for her valuable suggestions and encouragement to the end of this thesis.

I thanks to the committee; Assoc. Prof. Dr. Duangdao Channei, Asst. Prof. Dr. Pajaree Thongsanit and Dr. Pornnapa Sutawong for the valuable suggestions.

Importantly, I would like to express my deepest gratitude to my parents for their love, understanding, support and encouragement.

Finally, I specially thank Dr. Dang Trung Tri Trinh and Miss. Patcharaporn Phuinthiang for their help during the design experiments.

This study is financially supported by Naresuan University through the project R2566E002.

Yumatorn Mingmongkol

TABLE OF CONTENTS

	Page
ABSTRACT.....	C
ACKNOWLEDGEMENTS.....	F
TABLE OF CONTENTS.....	G
List of tables.....	I
List of figures.....	K
CHAPTER I INTRODUCTION.....	1
1.1 Background.....	1
1.2 Objectives of this study	3
1.3 Scope of this study.....	3
CHAPTER II LITERATURE REVIEW	5
2.1 Pollutants in the environment	5
2.2 Water treatment by advanced oxidation processes (AOPs).....	13
2.3 TiO ₂ Photocatalyst	18
2.4 Synthesis of TiO ₂ photocatalyst.....	19
2.5 Modification of TiO ₂	22
2.6 Operating factors on photocatalytic degradation.....	40
CHAPTER III RESEARCH METHODOLOGY	43
3.1 Synthesis of the nanoparticles	44
3.2 Characterization of the synthesized nanoparticles.....	46
3.3 Photocatalytic activity test.....	48
3.4 Calculation.....	51
CHAPTER IV RESULTS AND DISCUSSIONS	53
4.1 Characterization of Cu-doped TiO ₂ nanoparticles	53
4.2 Dyes degradation of Cu-doped TiO ₂ nanoparticles	60
4.3 Photokilling of Cu-doped TiO ₂ nanoparticles.....	62

4.4 Characterization of Mn-doped TiO ₂ nanoparticles	64
4.5 Dyes degradation of Mn-doped TiO ₂ nanoparticles	75
4.6 Drugs degradation of Mn-doped TiO ₂ nanoparticles	80
4.7 Photokilling of Mn-doped TiO ₂ nanoparticles	116
CHAPTER V CONCLUSIONS	118
REFERENCES	107
BIOGRAPHY	124



List of tables

	Page
Table 1 Properties of anatase and rutile of TiO ₂	19
Table 2 Degradation efficiency of undoped and Mn, Co, Zr doping with TiO ₂ under UV and visible light.....	28
Table 3 Specific surface area, pore volume and band gap values of TiO ₂ and CuO-TiO ₂	39
Table 4 Summary of synthesis of nanoparticles.	47
Table 5 Summary of the characterization of the synthesized nanoparticles.....	46
Table 6 Lattice parameters of undoped and Cu-doped TiO ₂ nanoparticles.....	54
Table 7 The specific surface area of undoped and Cu-doped TiO ₂	55
Table 8 EDX analytical data of undoped and Cu-doped TiO ₂	57
Table 9 Band gap energy of undoped and Cu-doped TiO ₂	60
Table 10 MB removal percentage of undoped and Cu-doped TiO ₂	61
Table 11 Percentage of anatase and rutile phases of undoped and Mn-doped TiO ₂ ...65	65
Table 12 Lattice parameters of undoped and Mn-doped TiO ₂	66
Table 13 The BET summarizes data of undoped and Mn-doped TiO ₂	68
Table 14 Band gap energy of undoped and Mn-doped TiO ₂	75
Table 15 MB photodegradation of Mn-doped TiO ₂ under UV-A irradiation.....	76
Table 16 Photodegradation of MB under visible light by undoped and Mn-doped TiO ₂	79
Table 17 Absorbance value of salbutamol in different concentrations at the wavelength of 276 nm.....	82
Table 18 SAL photodegradation of Mn-doped TiO ₂ under UV-A irradiation.	87
Table 19 SAL photodegradation of Mn-doped TiO ₂ under visible irradiation.....	94
Table 20 SAL degradation of 0.2% Mn-doped TiO ₂ data by LC-MS measuring.....	106
Table 21 Products during photocatalytic degradation of salbutamol.	112

Table 22 Average E. coli number of undoped and Mn-doped TiO ₂ under visible light.	116
Table 23 The intensity of products during photocatalytic degradation of salbutamol.	117



List of figures

	Page
Figure 1 Dyes classification based on molecular structure.....	5
Figure 2 Industries responsible for the presence of dye effluent in the environment...6	6
Figure 3 The chemical structure of methylene blue ($C_{16}H_{18}N_3SCl$).....	7
Figure 4 UV adsorption spectra of methylene blue	7
Figure 5 Antibiotics spread in the environment.....	9
Figure 6 Asthma and other allergic respiratory diseases treated by salbutamol.....	10
Figure 7 The chemical structure of salbutamol.....	11
Figure 8 UV adsorption spectra of salbutamol.	11
Figure 9 Schematic of gram-negative and gram-positive bacteria.	12
Figure 10 SEM images of E. coli cells on (a) large and (b) small scales.	13
Figure 11 Numbers of research papers on advanced oxygenation processes (AOPs) for water treatment (Web of Science, May 2017).....	14
Figure 12 General photocatalysis process of the semiconductor particle.....	17
Figure 13 Crystal structures of rutile, anatase, and brookite titanium dioxide.	18
Figure 14 Principle of sol–gel method; (a) films from a colloidal sol and (b) powder from a colloidal sol transformed into a gel (Znaidi, 2010).	20
Figure 15 Schematic of autoclave used for hydrothermal method.	21
Figure 16 Schematic of band structure of undoped TiO_2 , metal doped TiO_2 and	22
Figure 17 (a) Schematic, (b) UV–vis spectra, and (c) photoluminescence spectra.....	24
Figure 18 Cu-doped TiO_2 nanoparticles (a) schematic, (b) UV–vis spectra and.....	26
Figure 19 Photodegradation of methylene blue by TiO_2 with different Mn doping under visible light (Deng et al., 2011)	27
Figure 20 Photocatalytic activity of Mn-doped TiO_2 for glyphosate and methylene blue degradation under visible irradiation 300 minutes (Umar et al., 2016).	28
Figure 21 Photocatalytic activity of Mn-doped TiO_2 for methylene blue degradation under (a) UV and (b) visible irradiation (Binas et al., 2012).	29

Figure 22 Schematic for the energy band gap of (a) the bulk and (b) sulfuric acid modified anatase TiO ₂ (Yang et al., 2008).	30
Figure 23 Schematic illustration for the surface structure of (a) unmodified and (b) HF-modified TiO ₂ in the atmosphere and water (Walthall & Stark, 1999).....	31
Figure 24 Schematic for photoelectrochemical (PEC) water oxidation by cobalt (II) phosphate-modified TiO ₂ . Adapted from reference (Nilsson, Nordlinder, Wass, Meding, & Belin, 1993).	31
Figure 25 Schematic of (a) mechanism and (b) photocatalytic activity of the ISQ sensitized TiO ₂ nanoparticles under visible light (Z. Li, Fang, Zhan, & Xu, 2013)....	33
Figure 26 Equilibrium position of semiconductor-Metal nanocomposites with Redox Couple (a) before and (b) after UV irradiation, and schematic of photogenerated charge transfer and separation in semiconductor-metal heterojunctions (c) under UV and (d) visible irradiation.....	35
Figure 27 Photocatalytic degradation of methylene blue of TiO ₂ thin films containing Au, Ag and Cu nanoparticles (Sangpour, Hashemi, & Moshfegh, 2010).	36
Figure 28 Photocatalytic degradation of methylene blue of Ag/TiO ₂ under UV irradiation (Tseng & Chen, 2019).....	37
Figure 29 Band gap structures and direction of the charges of semiconductors- TiO ₂ heterojunctions.	37
Figure 30 Photocatalytic degradation of Gallic acid of TiO ₂ and CuO-TiO ₂ composites under visible light.	38
Figure 31 Schematic of energy level and electron-hole pair separation/transfer of undoped TiO ₂ , (b) semiconductor-TiO ₂ heterostructure, (c) metal, and (d) non-metal doping with TiO ₂ (Gnanasekaran et al., 2016).....	40
Figure 32 Summarization of research methodology.	43
Figure 33 Preparation of undoped TiO ₂ nanoparticle by hydrothermal method.	44
Figure 34 Preparation of CuO nanoparticles.	45
Figure 35 Preparation of Cu-doped TiO ₂ nanoparticles.	46
Figure 36 Preparation of Mn-doped TiO ₂ nanoparticles.....	46
Figure 37 Photocatalytic reactor under UV-A irradiation.	49
Figure 38 Photocatalytic reactor under visible irradiation.....	50
Figure 39 Photo-killing experimental setup under (a) UV and (b) visible light.....	51
Figure 40 XRD patterns of undoped TiO ₂ and Cu-doped TiO ₂ nanoparticles.	54

Figure 41 TEM images of (a) undoped, (b) 0.1 wt.% (c) 0.5 wt.%, and (d) 1.0 wt.% Cu-doped TiO ₂ nanoparticles.....	56
Figure 42 SEM images of (a) undoped, (b) 0.1 wt.% (c) 0.5 wt.%, and (d) 1.0 wt.% Cu-doped TiO ₂ nanoparticles.....	57
Figure 43 Reflection spectra (a) and Tauc plot (b) of Cu-doped TiO ₂ nanoparticles.	59
Figure 44 MB degradation of Cu-doped TiO ₂ nanoparticles	62
Figure 45 E. coli photokilling of Cu-doped TiO ₂ nanoparticles.....	63
Figure 46 Photo of visible E. coli colony after UV-A radiation.....	63
Figure 47 XRD patterns of undoped and Mn-doped TiO ₂ nanoparticles.	64
Figure 48 N ₂ adsorption-desorption isotherms of undoped and Mn-doped TiO ₂	66
Figure 49 Pore size distribution of undoped and Mn-doped TiO ₂ nanoparticles.	67
Figure 50 XPS spectra; (a) Ti 2p, (b) O 1s and (c) Mn 2p of Mn-doped TiO ₂ nanoparticle.....	69
Figure 51 TEM images of (a) undoped and (b) 0.2% Mn-doped TiO ₂ nanoparticles.	70
Figure 52 SEM images of (a) undoped TiO ₂ and (b) 0.2%Mn-doped TiO ₂ nanoparticles.	71
Figure 53 EDX spectra of (a) undoped TiO ₂ and (b) 0.2%Mn-doped TiO ₂ nanoparticles.	72
Figure 54 Reflection spectra (a) and Tauc plot (b) of Mn-doped TiO ₂ nanoparticles.	74
Figure 55 MB degradation of Mn-doped TiO ₂ under UV-A irradiation.	76
Figure 56 Absorbance spectrum of MB during degradation under visible irradiation by (a) undoped TiO ₂ , (b) 0.1% Mn-doped TiO ₂ , (c) 0.2% Mn-doped TiO ₂ and (d) 0.3% Mn-doped TiO ₂	78
Figure 57 MB degradation of Mn-doped TiO ₂ under visible irradiation.	80
Figure 58 Absorbance spectrum after subtracting baseline of salbutamol with different concentrations.	81
Figure 59 Calibration curve to determine the concentration of salbutamol (a) 0.1-1 and (b) 1-20 mg/L.	83
Figure 60 Absorbance spectrum after subtracting baseline of SAL during degradation under UV-A irradiation by (a) undoped TiO ₂ , (b) 0.1% Mn-doped TiO ₂ , (c) 0.2% Mn-doped TiO ₂ and (d) 0.3% Mn-doped TiO ₂	85

Figure 61 SAL degradation of the undoped and Mn-doped TiO ₂ under UV-A irradiation.....	88
Figure 62 Absorbance spectrum after subtracting baseline of SAL during degradation by undoped TiO ₂ nanoparticles under visible irradiation (a) 0-60 min and (b) 90-240 min.	89
Figure 63 Absorbance spectrum after subtracting baseline of SAL during degradation by 0.1% Mn-doped TiO ₂ nanoparticles under visible irradiation (a) 0-60 min and (b) 90-240 min.	90
Figure 64 Absorbance spectrum after subtracting baseline of SAL during degradation by 0.2% Mn-doped TiO ₂ nanoparticles under visible irradiation (a) 0-60 min and (b) 90-240 min.	91
Figure 65 Absorbance spectrum after subtracting baseline of SAL during degradation by 0.3% Mn-doped TiO ₂ nanoparticles under visible irradiation (a) 0-60 min and (b) 90-240 min.	92
Figure 66 SAL degradation of the undoped and Mn-doped TiO ₂ under visible irradiation.....	104
Figure 67 LC-MS chromatograms for peak area of SAL (a) in dark 60 min and after visible irradiation (b) 30, (c) 60, (d) 90, and (e) 180 min of 0.2% Mn-doped TiO ₂ ..	105
Figure 68 SAL degradation of the 0.2% Mn-doped TiO ₂ under visible irradiation by LC-MS and UV-Vis spectroscopy measuring.	106
Figure 69 LC-MS chromatograms of SAL (a) in dark 60 min and after visible irradiation (b) 30, (c) 60, (d) 90, and (e) 180 min of 0.2% Mn-doped TiO ₂	108
Figure 70 LC-MS spectra of salbutamol after dark adsorption	109
Figure 71 Mass spectrum of identified intermediates at various m/z fragments.	111
Figure 72 Possible photocatalytic degradation scheme of salbutamol.	115
Figure 73 Antibacterial activity of undoped and Mn-doped TiO ₂ nanoparticles.....	117
Figure 74 E. coli colony after visible irradiation of undoped and Mn-doped TiO ₂ ..	117
Figure 75 The powder of CuO, undoped and Cu-doped TiO ₂ nanoparticles.....	114
Figure 76 Photograph of the MB degradation color change of 0.1% Cu-doped TiO ₂ after UV irradiation for various times.....	115
Figure 77 The powder of undoped and Mn-doped TiO ₂ nanoparticles.	116

CHAPTER I

INTRODUCTION

1.1 Background

In the past decade, the contaminations in water have rapidly increased from a large number of industries. Discharging dyes into wastewater and water bodies is a major environmental problem. Dyes are widely used in several industries, such as leather, paper, plastic, textile, food processing, printing, cosmetics, and pharmaceuticals. The dye-containing wastewater can affect the aquatic environment because the dyes can block sunlight, which decreases oxygen dissolution, resulting in low photosynthetic activity for aquatic biota. In addition, some of the dyes can cause serious health problems such as cancer and mutation. Severe water contamination issues are the lack of safe water for drinking, household uses, agriculture, and farming. Therefore, dye removal is important before discharge into water.

In addition, the pharmaceutical pollutants, especially antibiotics drug, are commonly found in urban and industrial wastewater. Due to this pollutant were discharged to the environment from various sources, including pharmaceutical production plants, hospitals, wastewater treatment plants, excretion by humans and livestock treated with antibiotics. Antibiotics in the water have negative effect to human health and aquatic ecosystems, inducing problems such as toxicity and antibiotic-resistance. Most wastewater treatment hardly efficiently removes these compounds. Besides, antibiotic have continually been used with increasing due to the growing world population coupled with the rise in human life expectancy and the outbreak of the human coronavirus disease 2019 (COVID-19).

Several methods for pollutant removal have been reported in the literature about decontamination and handling of the contamination, ion flotation, coagulation, adsorption, and sedimentation. However, the end of these treatment methods produces a secondary waste product that needs further treatment. In order to solve this problem, Advanced Oxidation Processes (AOPs) have been developed and employed in wastewater treatment industries.

AOPs, such as ozonation, fenton and photocatalysis have shown high efficiency in reducing the concentration of pollutants in water. Among of these AOPs, photocatalytic is widely used for water treatment due to it has many advantages, such as low operating cost, ambient operating temperature, and complete mineralization of contaminants. TiO₂ is the most popular photocatalyst due to several advantages such as nontoxicity, thermodynamic stability, unique physical and chemical properties, and low cost. However, TiO₂ has low utilization of the sunlight spectrum due to it having a wide band gap (anatase: 3.2 eV, rutile: 3.0 eV). This limit needs to improve to enhance photocatalytic performance. Therefore, many researchers have been devoted to overcoming these shortages by various approaches such as structural modification or doping TiO₂.

Various modifications of TiO₂ photocatalysts with non-metal elements (C, B, N, F, S, and I) and metal elements (Fe, Co, Cr, V, Bi, Cu, and Mn) doping have made significant progress in the removal of various contaminations. Moreover, it has been thought of as a feasible method to expand the light response range, enhancing photocatalytic activity under sunlight. The problem can be solved by extending the range of optical response, especially metal doping TiO₂.

Many works try combining a narrow band gap semiconductor with TiO₂ to enhance photocatalytic activity (Jiang et al., 2016; Wei et al., 2016). CuO is one of the various low band gap semiconductors, which has been recognized to be combined with TiO₂ to improve visible light absorption and retard the recombination of the photogenerated electrons and holes. CuO is a p-type semiconductor material that is cheap and non-toxic. It also has good optical, electrical, and catalytic properties with a narrow energy gap of 1.2–1.7 eV. Many researchers reported that Cu-doped TiO₂ enhanced photocatalytic activity under UV light irradiation, increased quantum efficiency, and improved charge transfer compared to the TiO₂ nanoparticles (J. Wu et al., 2017). In the meanwhile, Mn-doped TiO₂ nanoparticles have received attention due to their enhanced photocatalytic efficiency (Deng, Xia, Guo, Gao, & Shao, 2011). The lower valence states of the dopants create oxygen vacancies and reduce the optical band gap of TiO₂. Therefore, it is helpful to maximize the solar light for photocatalytic activity (Binas, Sambani, Maggos, Katsanaki, & Kiriakidis, 2012).

For the above reasons, the TiO₂ nanoparticles doping with Cu and Mn are expected to be very effective for removing pollutant and other pollutants such as drugs and bacteria from wastewater and contaminated water under the sunlight light.

1.2 Objectives of this study

This study was conducted to achieve the following objectives:

1. Synthesize the TiO₂ nanoparticles with various dopants including Cu and Mn
2. Characterize the physico-chemical properties of Cu-doped TiO₂ and Mn-doped TiO₂
3. Investigate the photocatalytic activity of the nanoparticles for pollutants and degradation as well as the photocatalytic disinfection
4. Propose the removal of the pathway of the nanoparticles for the pollutants removal

1.3 Scope of this study

The scopes of this work were following:

1. The nanoparticles including undoped TiO₂, Cu-doped TiO₂ and Mn-doped TiO₂ were synthesized by sol-gel and hydrothermal methods. The doping contents were varied to achieve the best photocatalytic activity under UV and visible light.
2. The physico-chemical properties of the nanoparticles were characterized. The crystal structure of the nanoparticles was performed using X-ray diffraction (XRD). The shape of the nanoparticle surface was observed using a scanning electron microscopic (SEM) instrument. Moreover, the elemental of the nanoparticles was also identified using energy dispersive x-ray (EDX) spectroscopy. In addition, transmission electron microscopy (TEM) was used to examine the size and distribution of the nanoparticles. Besides, the Brunauer-Emmett-Teller (BET) methods were used to determine the total surface areas of the nanoparticles. Finally, the nanoparticles band gap energy was also estimated using diffuse reflectance UV-Visible spectroscopy (DRS).

3. The photocatalytic activity of the nanoparticles was studied to degrade various pollutants including dyes and antibiotics. The methylene blue (MB) and salbutamol (SAL) were representative of dyes and antibiotics respectively. In addition, the photocatalytic disinfection was carried out by investigating the antimicrobial activity of *Escherichia coli* (*E. coli*).



CHAPTER II

LITERATURE REVIEW

2.1 Pollutants in the environment

2.1.1 Synthetic dyes

Dyes are colorful substances produced to give materials such as fabrics, papers, or any colorable materials. There are many types of synthetic dyes and they can be commonly classified based on their molecular structure. Generally, dyes can be classified as anionic (acidic dyes) and cationic (basic dyes). Among them, azo dyes (anionic dyes) are a class of dyes considered the largest group of organic dyes containing nitrogen-nitrogen double bonds but at the same time are quite toxic.

Sometimes, dyes are classified by their application or even by their solubility. Dyes are classified based on chromophore structure into reactive dyes, solvent dyes, basic dyes, direct dyes, and vat dyes, as shown in Figure 1 (Rauf & Ashraf, 2012).

Among all dye types, azo dyes are the highest produced dye type at a 70% production rate and are the most frequently utilized dye worldwide.

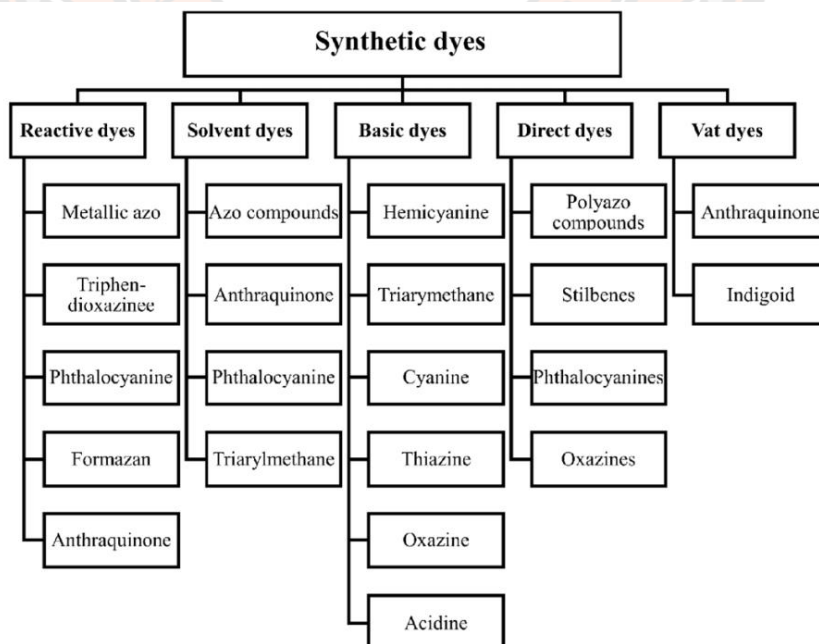


Figure 1 Dyes classification based on molecular structure.

Synthetic dyes are essential in various industries, such as the leather, paper, and textile industries. Often, dyes have served their purpose; most of them are discarded into environmental water bodies or wastewater. Mainly industries are known to be responsible for the presence of dye effluents in the environment, as shown in Figure 2 (Rauf & Ashraf, 2012). The dyeing industry (21%), paper and pulp industry (10%), tannery and paint industry (8%) and the dye manufacturing industry (7%) are known to produce high amounts of dye effluents from various associated processes. Figure 2 shows that the textile industry (54%) releases the highest amount of dye effluent, contributing to more than half of the existing dye effluents in the environment around the world.

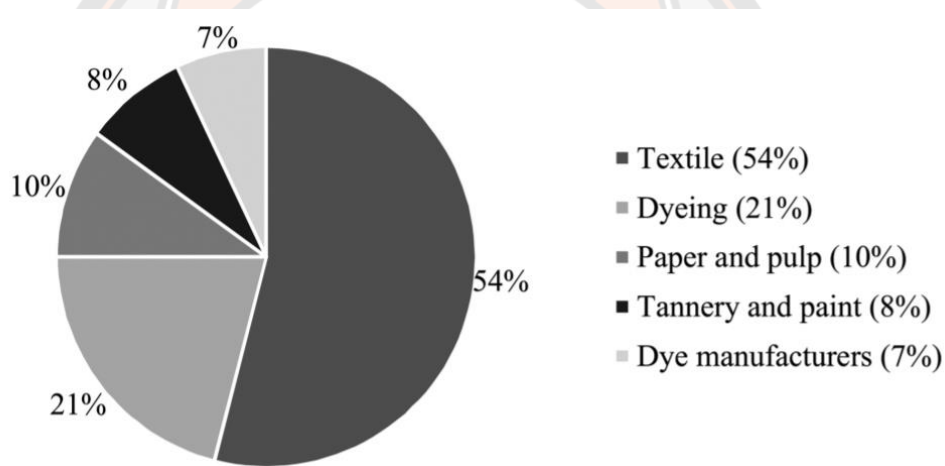


Figure 2 Industries responsible for the presence of dye effluent in the environment.

Dye effluents, better known as dye wastewater, block sunlight that decreases oxygen dissolution and can be toxic to animals and humans. Dyes are widely used in various industries and more than 20% of dyes are lost as contaminated in the environment. Moreover, some dyes can cause serious health problems such as cancer and mutation. The removal of dye molecules from water sources has become a major environmental concern.

Methylene blue (MB) is an aromatic synthetic cationic dye that can form a stable solution with water at room temperature (Russo, Masiello, Trifuoggi, Di Serio, & Tesser, 2016). MB is widely used with a high adsorption capacity in the industrial

process of dyeing silk, wool, cotton and paper in the industrial process (Gupta, Suhas, Ali, & Saini, 2004). Additionally, it is commonly used for biological staining. Moreover, MB is used to treat diseases such as duck hepatitis B, psoriasis, West Nile virus methemoglobinemia and urinary tract infections (Bayomie et al., 2020; Ullah et al., 2022). However, accumulation of MB in wastewater has harmful health effects such as difficulties in breathing, nausea, vomiting, diarrhea and eye burns (Mahapatra, Ramteke, & Paliwal, 2012).

The methylene blue (3,7-bis(dimethylamino)-phenothiazin-5-ium chloride) is a cationic dye with the molecular formula $C_{16}H_{18}N_3SCl$ with a molecular weight of 319.85 g/mol and the chemical structure of this dye shown in Figure 3. The maximum absorbance wavelength of methylene blue is 664 nm, as shown in Figure 4 (Dinh et al., 2019).

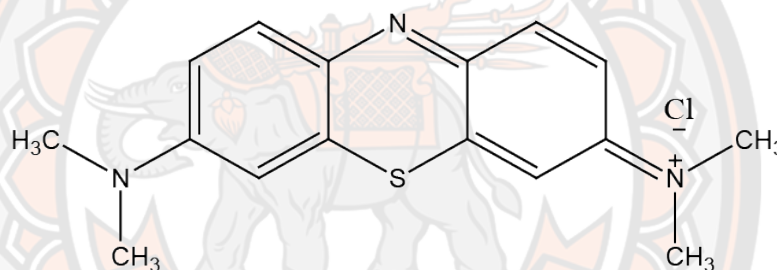


Figure 3 The chemical structure of methylene blue ($C_{16}H_{18}N_3SCl$).

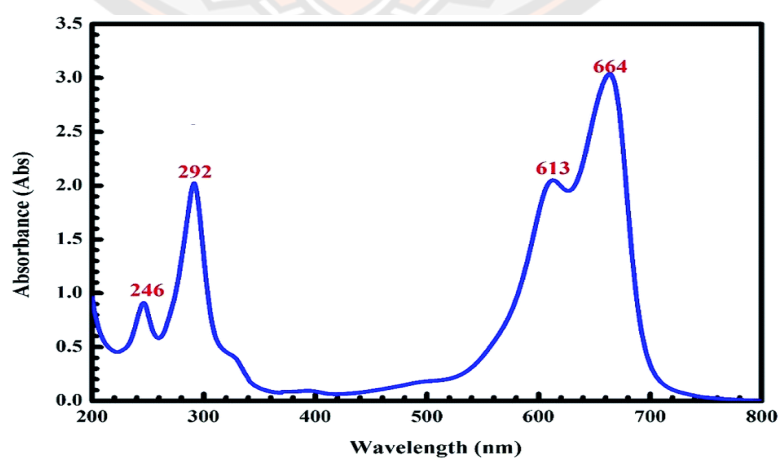


Figure 4 UV adsorption spectra of methylene blue

2.1.2 Pharmaceuticals

Antibiotics are medications used to kill bacteria or slow down bacterial growth. Antibiotics are compounds widely used in humans, farm animals and agriculture. It is continuously grown and consumed in large volumes with many consumers and various antibiotics. It was reported that approximately 100,000 to 200,000 tons of antibiotics were consumed in the world per year and discharged into the environment as the parent compounds or incomplete metabolites (Yan et al., 2013). Several reports have detected antibiotic residues in livestock and other industrial wastewater. In addition, antibiotics have also been detected in soil, water, manure and sludge (Göbel, Thomsen, McArdell, Joss, & Giger, 2005; Kümmerer, 2009). Antibiotics in hospitals and urban wastewater were detected in the concentration range of 0.3 to 100 mg/L and higher (Le-Minh, Khan, Drewes, & Stuetz, 2010). Unfortunately, conventional wastewater treatment plants are ineffective removal of these compounds. Therefore, concentrations ranging from ng/L to mg/L of antibiotics in surface and underground waters and other aquatic resources have been found (Almasi et al., 2016; Frontistis, Mantzavinos, & Meriç, 2018). This phenomenon leads to bacteria responding to antibiotic resistance by adapting to an antibiotic in the environment, causing antibiotic resistance bacteria. Antibiotic-resistant bacteria in the environment are steadily resistant and can transmit this behavior through cellular plasmids to other bacteria.

The effluent containing antibiotic residues is. Overall, antibiotic and antibiotic-resistant bacteria contamination in the environment occurs in a closed-loop that includes food chain routes and bioaccumulation and biomagnification generated from hospitals, houses, farms, humans, animals and agriculture, as illustrated in Figure 4.

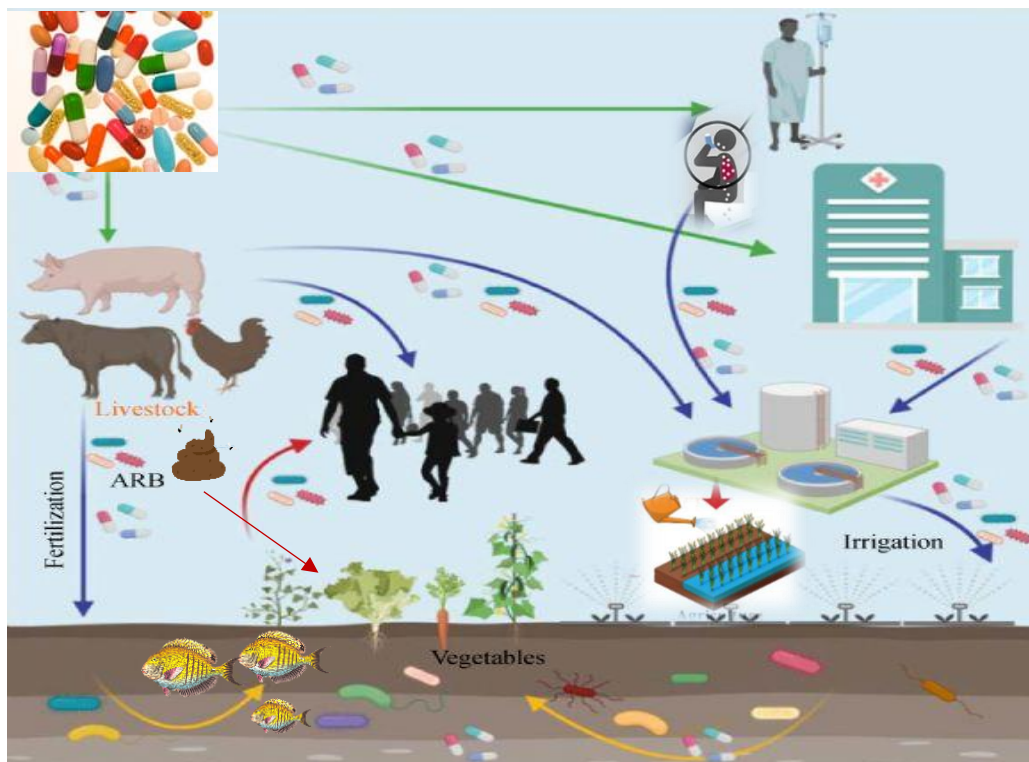


Figure 5 Antibiotics spread in the environment.

Humans face a cumulative number of antibiotic-resistant bacteria known as environmental health risks that are declared as one of the top five risks to global health by the World Health Organization (WHO). Furthermore, the WHO declares that antibiotic resistance diseases cause 700,000 deaths per year which could increase to 10 million by 2050 if no action is taken (United, 2019).

Salbutamol is a pharmaceutical compound or antibiotic drug widely used to treat asthma, chronic obstructive pulmonary, and other allergic respiratory diseases (J. Li et al., 2017). Salbutamol is one kind of β_2 -adrenoceptor agonist that has short-acting bronchodilation and anti-inflammatory effects.

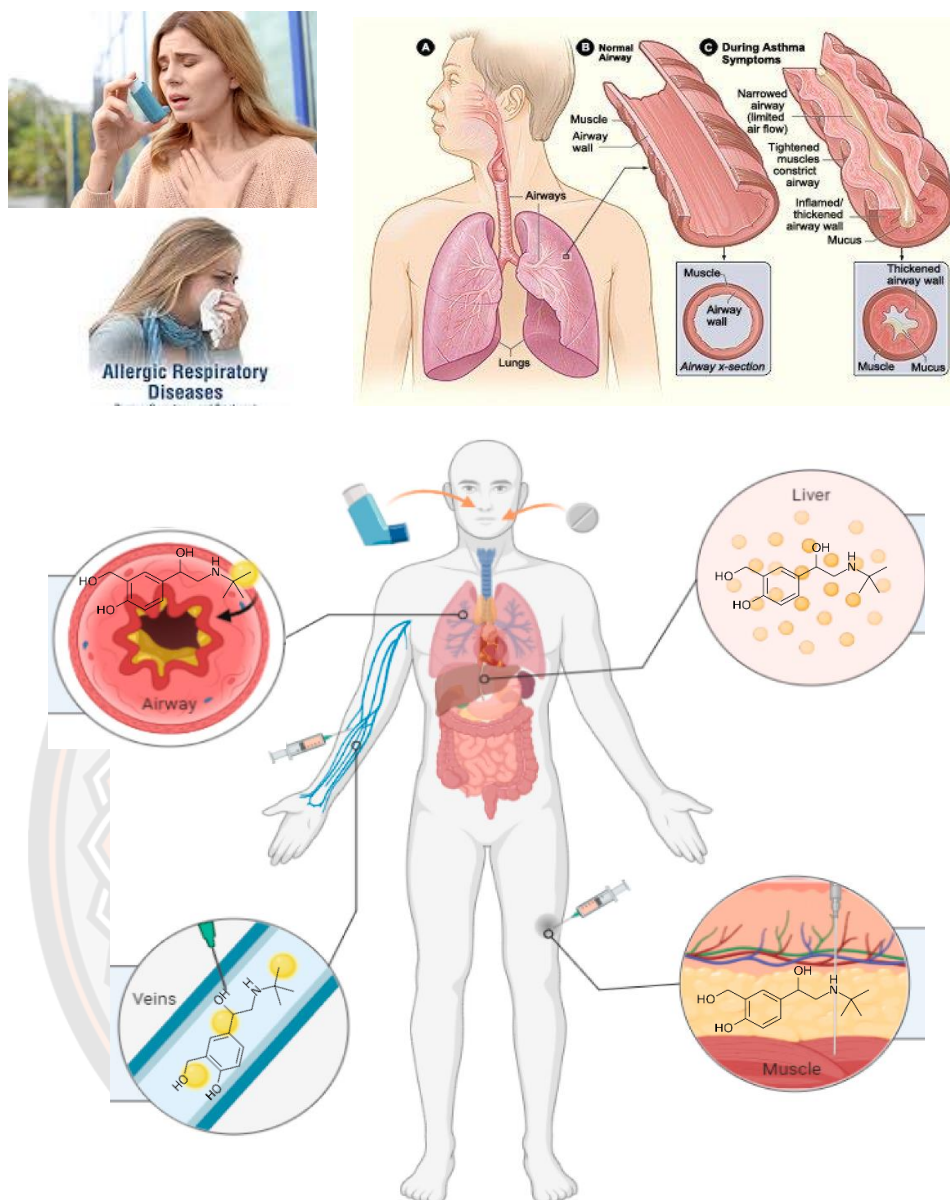


Figure 6 Asthma and other allergic respiratory diseases treated by salbutamol.

The chemical structure of salbutamol (4-[2-(tert-butylamino)-1-hydroxyethyl]-2-(hydroxymethyl phenol) with the molecular formula $C_{13}H_{21}NO_3$, also known as albuterol, is shown in Figure 7 (Dodson, Vogt, Marks, Reichardt, & Crespo-Hernández, 2011). The maximum absorption of salbutamol is at the wavelengths 224 and 276 nm, as shown in Figure 8.

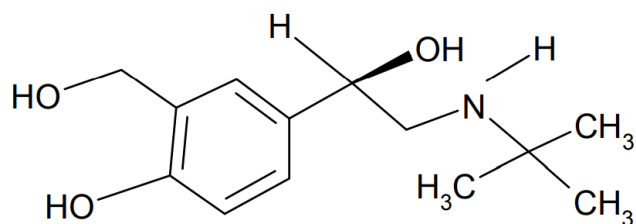


Figure 7 The chemical structure of salbutamol.

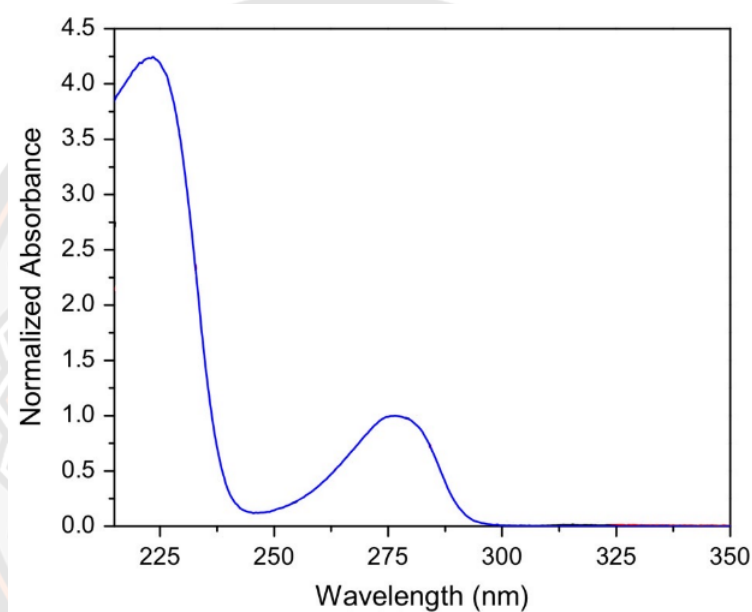


Figure 8 UV adsorption spectra of salbutamol.

Extensively used salbutamol led to water pollution problems such as incomplete metabolism in the organism. The excess salbutamol is excreted in urine as an unchanged drug, and its conjugated metabolite is mainly sulfate (Damasceno, Ventura, Ortuño, & Segura, 2000). There are several reports observed of this pollutant. Salbutamol occurred at concentrations less than 20 ng/L in municipal sewage effluents (Ternes, 1998) and ranged from 1.14 to 2.48 ng/L on the water surface of Italy (Calamari, Zuccato, Castiglioni, Bagnati, & Fanelli, 2003). Although there is a low level, the related potential toxic effects are weakly known. However, some areas have much higher salbutamol residues, with more than 471 ng/L found on the UK water surface by Bound and Voulvoulis (Bound & Voulvoulis, 2006).

2.1.3 Microorganisms

Microorganisms or microbes are microscopic organisms that exist in a single-celled form or as a cell colony consisting of bacteria, fungi, viruses, algae, and protozoa. The most numerous microorganisms are bacteria. Bacteria are prokaryotic cells that do not contain organelles and have no nucleus inside the cell. The average size of bacteria is around 0.25–10 μm . Generally, bacteria can be divided into 2 types based on the physical and chemical properties of the peptidoglycans in the microorganism's cell wall. Gram-positive bacteria with thick cell walls retain the crystal violet-iodine complex after treatment with acid-alcohol in a gram stain test and appear violet color and stain. Common gram-positive bacteria include *Staphylococcus aureus* (*S.aureus*), *S.epidermidis*, *Streptococcus pyogenes*, *S.pneumoniae*, and *Enterococci*. In contrast, gram-negative bacteria decolorized with the same treatment appear to lose crystal violet and show stained red or pink (Coico, 2006). Gram-negative bacteria are the most common primary pathogen, including *Escherichia coli*, *Salmonella*, *Providencia*, *Pseudomonas*, *Klebsiella*, *Proteus*, *Morganella*, *Aeromonas*, and *Citrobacter*. The scheme of gram-negative and gram-positive bacteria is shown in Figure 9 (Coico, 2006).

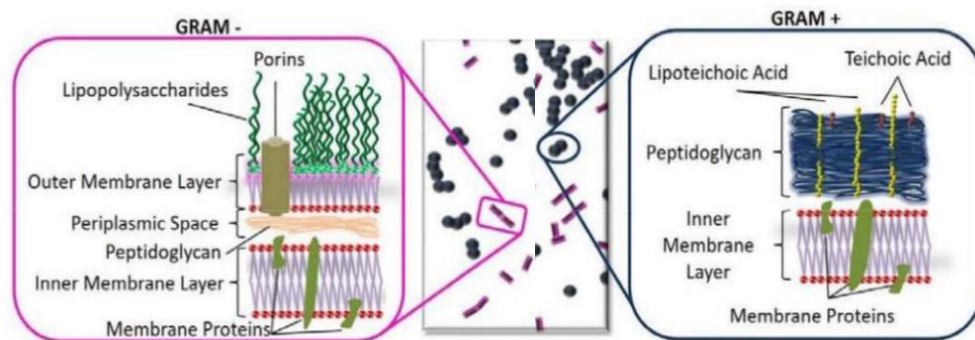


Figure 9 Schematic of gram-negative and gram-positive bacteria.

Escherichia coli (*E. coli*) is widely used as an indicator organism of water to determine water purity. Pathogenic microbes may also be found in water samples where *E. coli* is present (De Vietro et al., 2019). Consequently, *E. coli* is also used to evaluate the efficiency of water disinfection methods. Suppose the water sample is

free from *E. coli* after a disinfection process; it is concluded that the method is efficient and the water is free from fecal contamination, thus it unnecessary to analyze other pathogens in the water sample (Ajiboye, Babalola, & Onwudiwe, 2021). The SEM images of *E. coli* cells are shown in Figure 10 (Nidheesh, 2017).

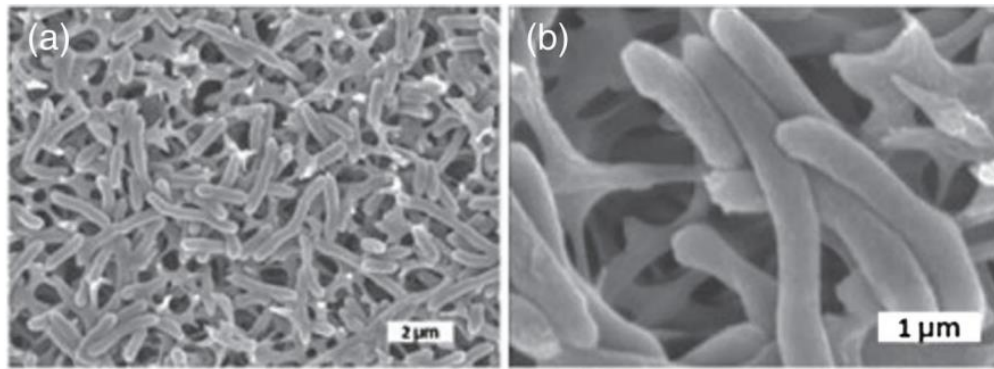


Figure 10 SEM images of *E. coli* cells on (a) large and (b) small scales.

2.2 Water treatment by advanced oxidation processes (AOPs)

Advanced oxidation processes (AOPs) were defined by Glaze and co-workers in 1987. The AOP generates highly reactive species to degrade the contamination. AOPs have been widely used to treat wastewater to remove various organic matters. AOP gives the possibility to produce hydroxyl radicals, which are greatly powerful oxidizing species. The mainly used of AOPs for water treatment are (i) ozonation, (ii) Fenton oxidation, and (iii) photocatalysis.

AOP has been continuously interested in researchers as an increase in the number of research papers on this topic was reported in Figure 11.

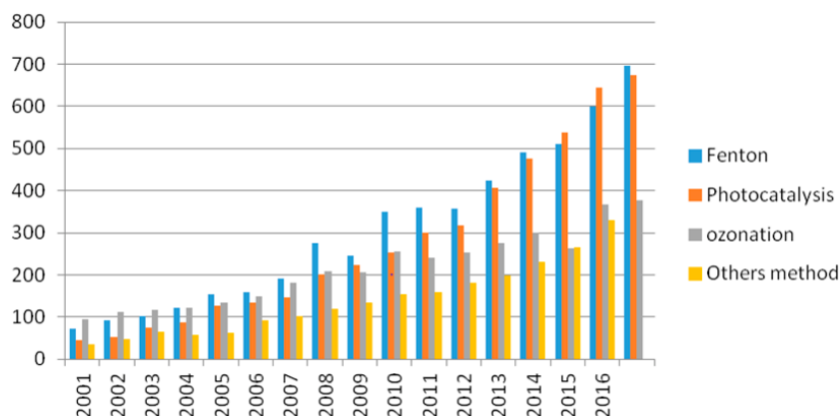
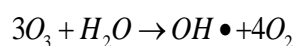


Figure 11 Numbers of research papers on advanced oxygenation processes (AOPs) for water treatment (Web of Science, May 2017).

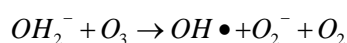
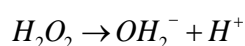
2.2.1 Ozonation

Ozone is a greatly powerful oxidizing agent, which is able to participate in a great number of reactions with organic and inorganic compounds. In the dark, ozone can slowly react with organic compounds by hydroxyl radicals. However, ozone can generate additional hydroxyl radicals with UV light due to the photolysis of O_3 , increasing the efficiency. The disadvantages of ozonation are the low solubility of O_3 in water and the high energy costs. Therefore, the main application of ozonation is for disinfection in wastewater treatment plants for drinking water.

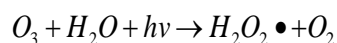
Hydroxyl radical ($OH\cdot$) is produced from ozone (O_3) to oxidation the contamination in water. In the detailed mechanisms have been explained the complex $OH\cdot$ generation as below.



In addition, the $OH\cdot$ yield can be significantly improved by peroxone (O_3/H_2O_2) system, the O_3 decomposition and $OH\cdot$ production are enhanced by hydroperoxide (HO_2^-) produced from H_2O_2 decomposition.



In the O₃/ultraviolet (UV) irradiation, H₂O₂ is generated as an additional oxidant primarily through O₃ photolysis. After that OH· can be generated by photolysis of H₂O₂ as show in below.

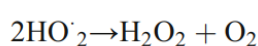
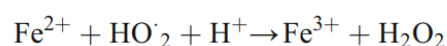
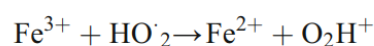
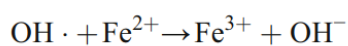
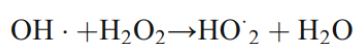
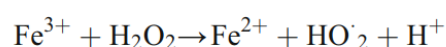
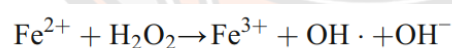


2.2.2 Fenton Oxidation

In the 1890s, Fenton H.J.H. discovered the reaction of polycarboxylic acid by hydrogen peroxide (H₂O₂) with ferrous ions (Fe²⁺). In the dark, the Fenton process involves using an oxidant, generally H₂O₂, and a catalyst, usually iron in the form of ferrous ions. The oxidation of Fe₂₊ generates hydroxyl radicals. The disadvantages of the Fenton process, it occurs in the acid medium, and iron removal is required.

The photo Fenton process with sunlight irradiation or other light source improves the efficiency of the treatment thanks to the photoreduction of the Fe³⁺ to Fe²⁺, which results in the additional generation of hydroxyl radicals. This process requires additional costs for UV irradiation advantage of this process.

Iron is the most frequently used to activate H₂O₂ and produce hydroxyl radicals in water, namely the Fenton process. Fe²⁺ reacts with H₂O₂ to generate hydroxyl radicals which are strong reactive species. The Fenton radical mechanisms primarily involve the following reactions:

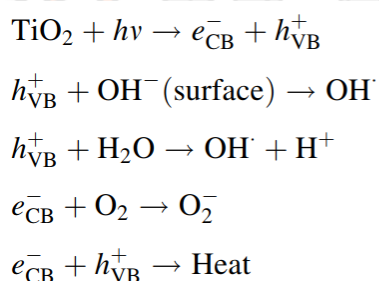


Notably, the generation of hydroxyl radicals during the Fenton reaction is the most effective only at an acidic pH condition. As a result, the application of Fenton reaction for wastewater treatment is restricted in practice.

2.2.3 Photocatalysis

Photocatalysis is one of the AOP that uses a semiconductor as a catalyst and a light source.

Several semiconductors have been used as a catalyst in this AOP. The most common catalyst is titanium dioxide (TiO₂) and an RO-type semiconductor. However, titanium dioxide (TiO₂) is the most widely used due to its high photoactivity, non-toxicity, low cost, and chemical inertness. The beginning procedure of the photocatalytic reaction is the adsorption of the radiation. TiO₂ particles are excited to produce positive holes in the valence band ($h\nu^+$) with an oxidative capacity and negative electrons at the conduction band (e^-) with a reductive capacity. The electrons and holes can either recombine and produce thermal energy or interact with other molecules. The holes can react with electron donors in the solution to produce powerful oxidizing free radicals, such as hydroxyl radicals, which oxidize the organics on the surface. The holes can also oxidize the substrate by direct electron transfer. Briefly, the photogeneration of radical species in TiO₂ under a radiation system can be described as follows:



A photocatalyst is a substrate that absorbs light and acts as a catalyst for chemical reactions. Generally, the photocatalyst combines two words: photo related to photon and catalyst, a substance altering the reaction rate in its presence. Therefore, photocatalysts are materials that change the rate of a chemical reaction on exposure to light. All the photocatalysts are semiconductors. This phenomenon is known as photocatalysis. Photocatalysis includes reactions that take place by utilizing light and a semiconductor. Photocatalysis is a phenomenon in which an electron-hole pair is generated on exposure of a semiconducting material to light. Photocatalytic reactions can be categorized into two types based on the appearance of the physical state of reactants.

- Homogeneous photocatalysis: When both the semiconductor and reactant are in the same phase, i.e., gas, solid, or liquid, such photocatalytic reactions are termed homogeneous photocatalysis.

- Heterogeneous photocatalysis: When both the semiconductor and reactant are in different phases, such photocatalytic reactions are classified as heterogeneous photocatalysis.

Photocatalysis is divided into several steps such as:

Step 1: Diffusion reactants to the catalytic surface

Step 2: Absorption of reactants onto the catalysis surface

Step 3: UV light absorption, molecules move from ground state to excited state

Step 4: Photocatalysis (two main phases)

- + Elementary photocatalytic reaction in which excited molecules are directly involved in the reaction with adsorbed substances.

- + Secondary photocatalysis reaction, called dark reaction or thermal reaction, in which the products of elementary reaction such as enable undergo secondary reaction.

Step 5: Reabsorption of products

Step 6: Diffusion products into a solution

The general photocatalysis process of semiconductor particles show in Figure

12.

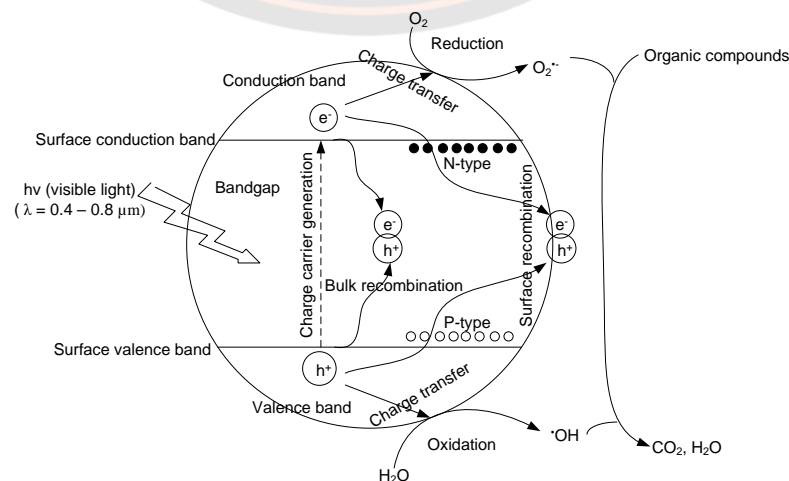


Figure 12 General photocatalysis process of the semiconductor particle.

2.3 TiO₂ Photocatalyst

Titanium dioxide is known as titanium (IV) oxide or titania with the chemical formula TiO₂. It is a white solid inorganic substance with physical characteristics as thermally stable, non-flammable, and poorly solubility. Generally, it occurs in well-known rutile, anatase, and brookite structures. The titanium atoms are gray, and the oxygen atoms are red (Figure 13). TiO₂ nanoparticles are used widely due to their high stability, anti-corrosive and photocatalytic properties. Titanium dioxide, particularly in the anatase form, is used to decompose organic pollutants under UV light.

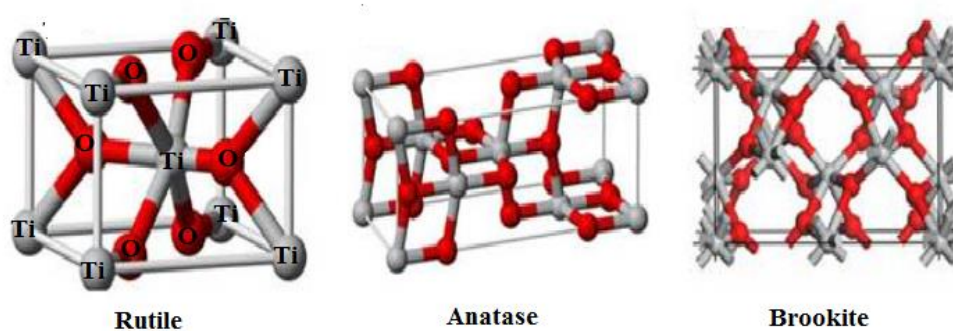


Figure 13 Crystal structures of rutile, anatase, and brookite titanium dioxide.

The most important property of titanium dioxide is a good photocatalytic, that is a semiconductor with the band gap 3.0 eV for rutile and 3.2 eV for anatase phase. Titanium dioxide absorbs violet visible light and near Ultraviolet (UV) light in which TiO₂ rutile can absorb violet visible light with the wavelength 415 nm and TiO₂ anatase only absorb the edge of visible light and near UV light (UV-A) with the wavelength 385 nm. Brookite is not excited by UV light but it can be transformed into rutile at high temperature. Generally, TiO₂ anatase is more photocatalytic activity than TiO₂ rutile. It can be explained with some reasons following. Anatase with larger bandgap can raise the maximum of bandgap to higher energy relative to redox potentials of adsorbed molecules and facilitates electron transfer from TiO₂ to adsorbed molecules. The surface properties of anatase are higher adsorption of molecules and subsequent charge transfer to the molecule. Anatase is more participant in surface reactions than rutile due to longer charge carrier lifetime. Mixed anatase

with (80%) and rutile (20%), called Degussa P25 TiO₂, is higher proportion of anatase. It is not completely understood that why the mixed anatase and rutile is better work as visible light than rutile on its own. Maybe, catalytic activity of titanium oxide powder is moved into visible region by rutile whereas anatase needed. The properties of anatase and rutile phase of TiO₂ are summarized in Table 1.

Table 1 Properties of anatase and rutile of TiO₂.

Property	Anatase	Rutile
Molecular weight (g/mol)	79.88	79.88
Melting point (°C)	1825	1825
Boiling point (°C)	2500–3000	2500–3000
Light absorption (nm)	<390	<415
Mohr's Hardness	5.5	6.5–7.0
Refractive index	2.55	2.75
Dielectric constant	31	114
Crystal structure	Tetragonal	Tetragonal
Lattice constants (Å)	$a = 3.78$ $c = 9.52$	$a = 4.59$ $c = 2.96$
Density (g/cm ³)	3.79	4.13
Ti–O bond length (Å)	1.94 (4) 1.97 (2)	1.95 (4) 1.98 (2)

2.4 Synthesis of TiO₂ photocatalyst

The synthesis of TiO₂ photocatalyst has been developed as many physical and chemical methods, such as sol-gel, solvothermal, impregnation, sputtering, dip-coating, co-precipitation, mechanical synthesis, chemical synthesis, vapor deposition and others. In many cases, combine the synthetic methods and reaction steps in order to create a specific photocatalyst with the desired characteristics. In this section, some of the most used methods for the synthesis of TiO₂-based heterostructures are reviewed.

2.4.1 Sol-gel method

The sol-gel method consists of the acidic or basic hydrolysis of an organometallic precursor, followed by a slow polymerization. The obtained material is dried, allowing the decomposition and elimination of all the organic components present in the gel. Usually, this method involves acid-catalyzed hydrolysis of titanium (IV)

alkoxide tracked by condensation. This process includes 4 steps, (i) hydrolysis, (ii) polycondensation, (iii) drying and (vi) thermal decomposition. The main steps of preparation of thin films and powder by the sol-gel method are shown in Figure 14.

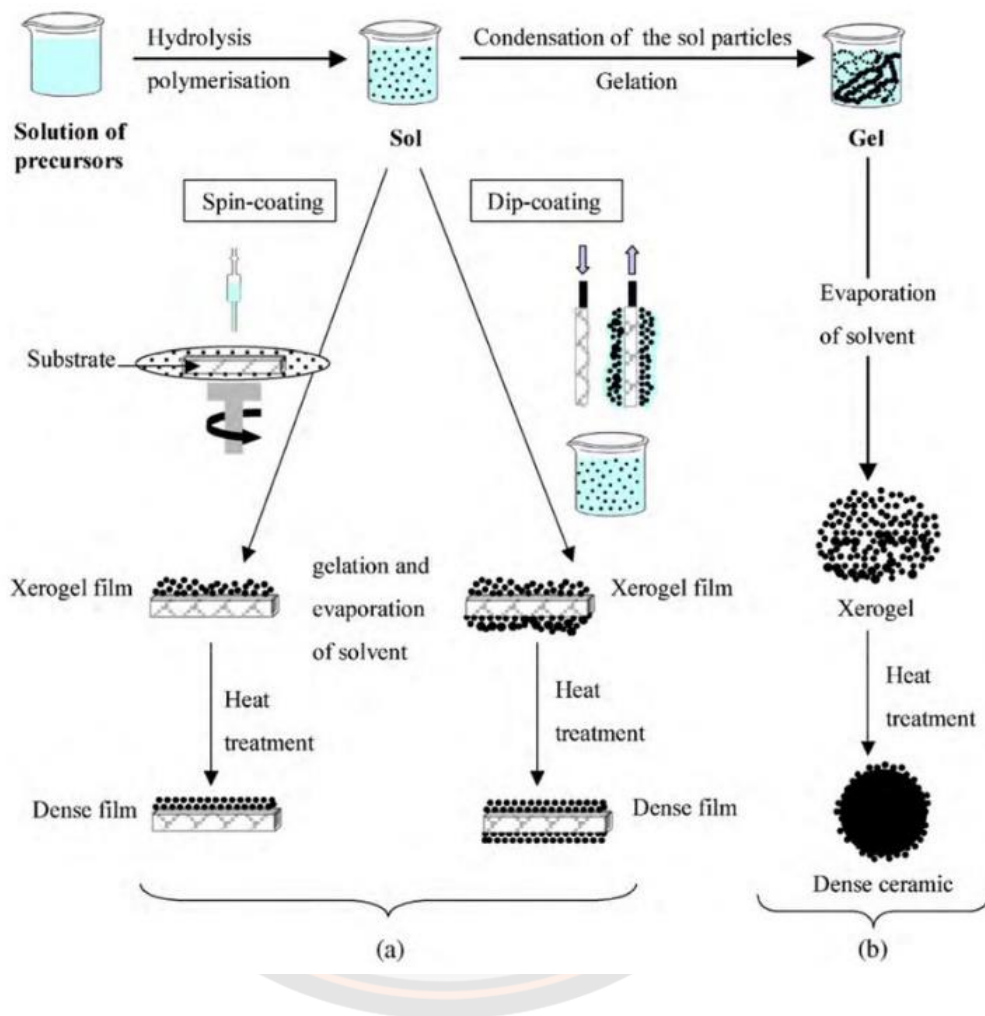


Figure 14 Principle of sol-gel method; (a) films from a colloidal sol and (b) powder from a colloidal sol transformed into a gel (Znaidi, 2010).

The sol-gel method advantages are summarized as follows:

- Low price as no particular apparatus.
- Low processing temperature.
- Easiness of manufacturing multi-component materials.
- Product homogeneity.
- Good particle shape and size distribution.

As the advantages of sol-gel method, there are many research used this method to produce TiO_2 composites. For example, WO_3/TiO_2 nanocomposites have been synthesized by the sol-gel method using $\text{Ti}(\text{OBU})_4$ and ammonium tungstate as main precursors (Rashad, Elsayed, Al-Kotb, & Shalan, 2013). To test the photocatalytic activity of materials on the malathion degradation by using natural sunlight. The complete degradation of the pollutant was achieved after a 2 h irradiation and a mineralization rate of 63% upon 5 h. The different of $\text{CeO}_2/\text{TiO}_2$ heterostructures were synthesized by the sol-gel method, using $\text{Ti}(\text{OBU})_4$ and $\text{Ce}(\text{NO}_3)_3 \cdot 6\text{H}_2\text{O}$ as precursors (Yang et al., 2008). The synthesized materials were tested for the degradation of methyl orange, noting the enhanced activity of the $\text{CeO}_2/\text{TiO}_2$ composite compared with unmodified TiO_2 and CeO_2 .

2.4.2 Hydrothermal method

The hydrothermal method is one of the most common preparation techniques for photocatalyst. Due to this method can operate with the variation of pressure and temperature parameters that allows the formation of a wide diversity of crystal morphologies. The products obtained are usually well dispersed in form and size. The hydrothermal method refers to the use of an aqueous solution as a reaction system in a special closed reactor, namely autoclave shows as Figure 15.

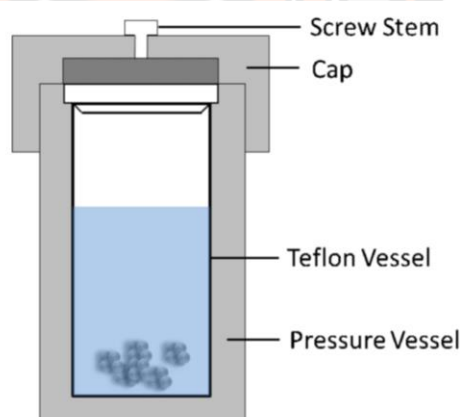


Figure 15 Schematic of autoclave used for hydrothermal method.

The hydrothermal method allows the synthesis of crystalline materials by heating the solution inside the autoclave to create a high temperature and high pressure as the vapor pressure is generated by itself. The process dissolves and recrystallizes a poorly soluble or insoluble substance under normal conditions.

The hydrothermal method is generally used for synthesizing TiO₂ catalysts. For example, CdS/TiO₂ composites were synthesized by hydrothermal method to form anatase nanoparticles with highly dispersed CdS nanocrystals on the surface. The results found that modifying TiO₂ with CdS nanoparticles increased the absorption of visible light irradiation at 550 nm. In addition, Bi₂O₃/TiO₂ photocatalysts were prepared, which displayed high photocatalytic activity due to their enhanced visible light absorption.

2.5 Modification of TiO₂

According to TiO₂ has a wide band gap and fast recombination of photogenerated charge carriers (electron-hole pairs) still significantly limits its practical applications. Various attempts have been created to overcome these lacks. Among them, doping with metal and non-metal elements, fabricating heterojunctions, surface modification with inorganic acids, and dye sensitization are widely investigated. This section is included as the following.

2.5.1. Doping metal and non-metal elements

Doping TiO₂ with metal or non-metal can increase its capacity for visible light absorption or its reactivity in the UV spectrum. The band structure of the undoped TiO₂, metal-doped TiO₂ and non-metal-doped TiO₂ are compared in Figure 16.

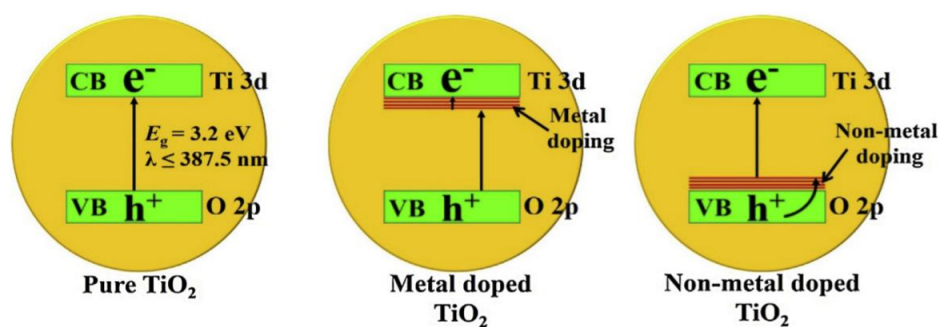
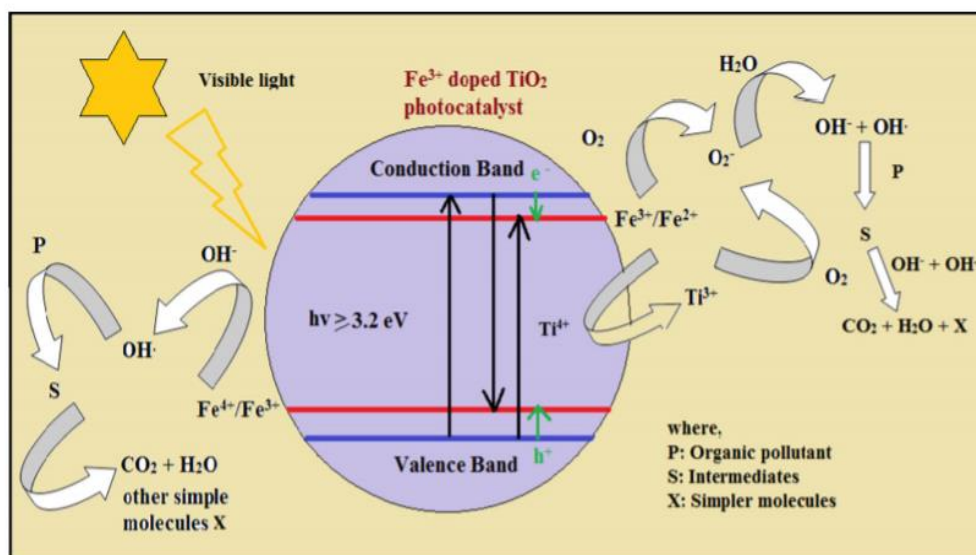


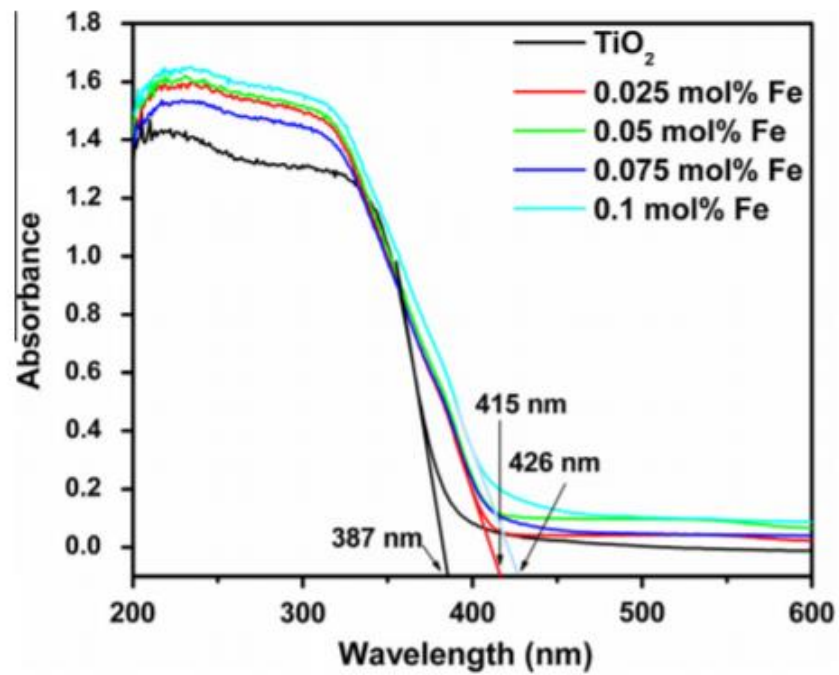
Figure 16 Schematic of band structure of undoped TiO₂, metal doped TiO₂ and non-metal doped TiO₂ (Low, Cheng, & Yu, 2017).

Metallic elements can induce a suitable bandgap shift and promote recombination due to minimizing the photocatalysis capability in combination with thermal instability. The lack of using metal-doped photocatalysts is leaching. It can undergo photo-corrosion during the photocatalytic process. Therefore, using non-metals, such as nitrogen, sulfur, and carbon, instead of metals to dope TiO₂ photocatalysts seems to be a viable approach for developing visible-light active photocatalysts.

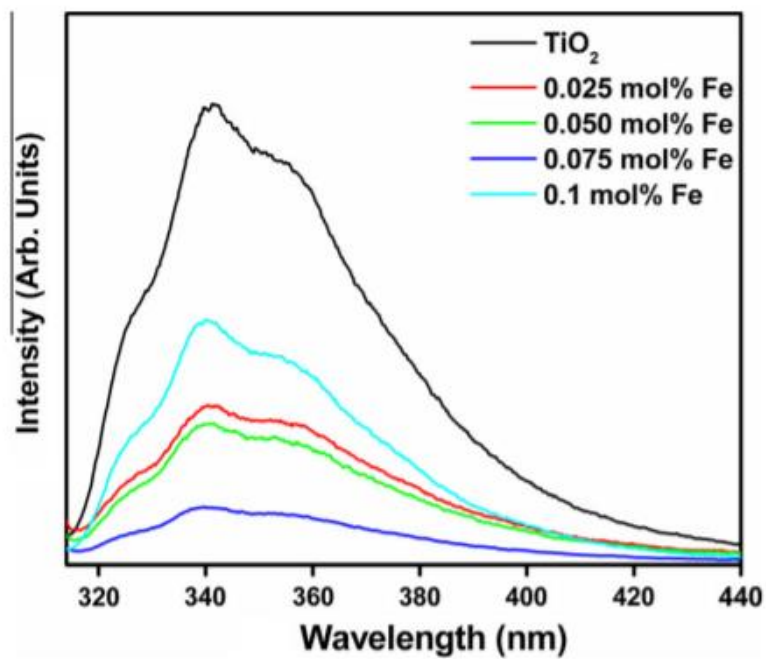
There are several methods to synthesize the non-metal doped TiO₂, especially hydrothermal, sol-gel and microwave-assisted. For example, Fe-doped TiO₂ by ultrasonic-assisted synthesis by hydrothermal method. It was observed that Fe doping extended the absorption of TiO₂ from UV to the visible region. The band gap was effectively reduced from 3.2 to 2.9 eV, resulting in enhanced visible-light photocatalytic activity for para-nitrophenol degradation. The schematic mechanism, UV-vis spectra and photoluminescence spectra for pollutant degradation by Fe-doped TiO₂ photocatalyst are shown in Figure 17.



(a)



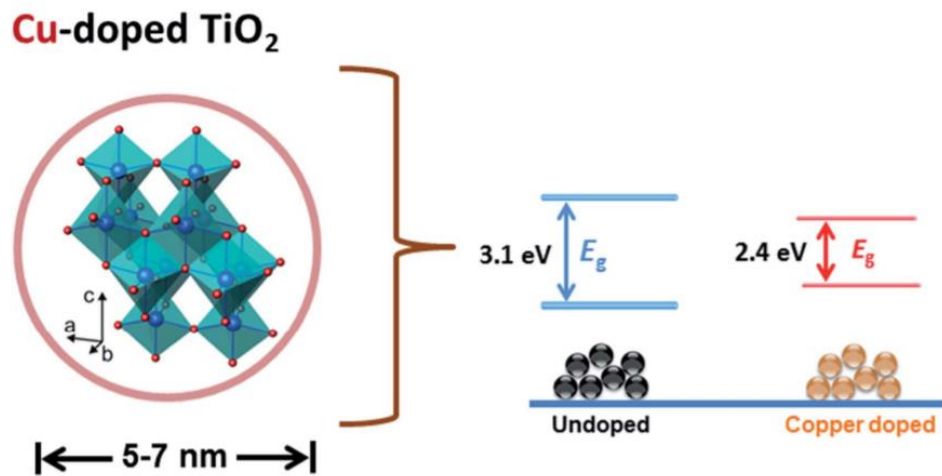
(b)



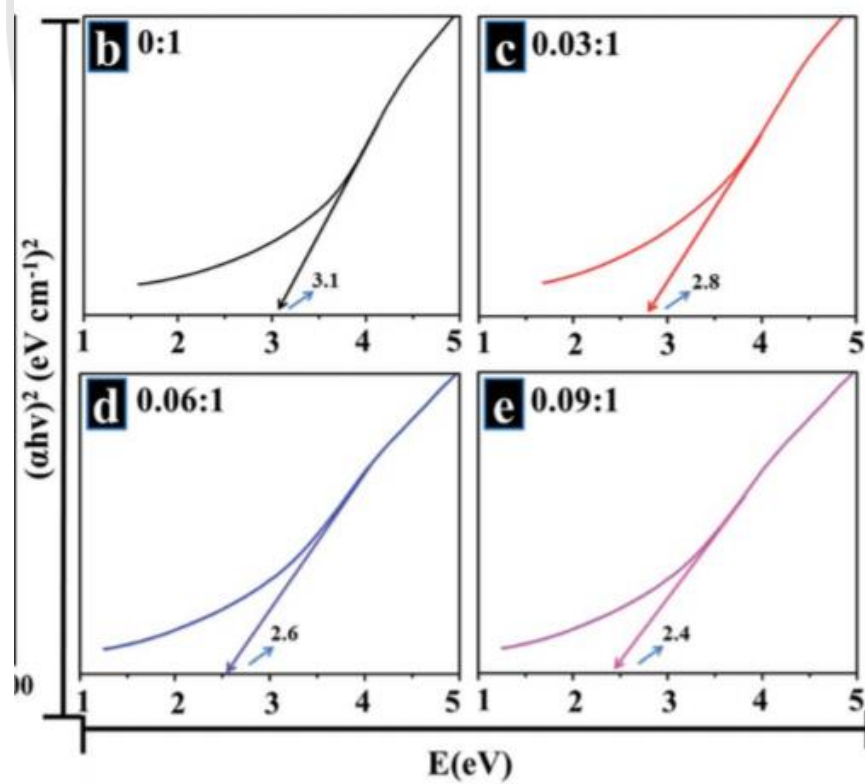
(c)

Figure 17 (a) Schematic, (b) UV-vis spectra, and (c) photoluminescence spectra of Fe-doped TiO₂ nanoparticles (Sood, Umar, Mehta, & Kansal, 2015).

For other research to get similar results, Cu-doped TiO₂ was prepared with a sol-gel chemical method. Various concentrations (3, 6, and 9 wt%) of Cu dopant were employed. The results are summarized in Figure 18.



(a)



(b)

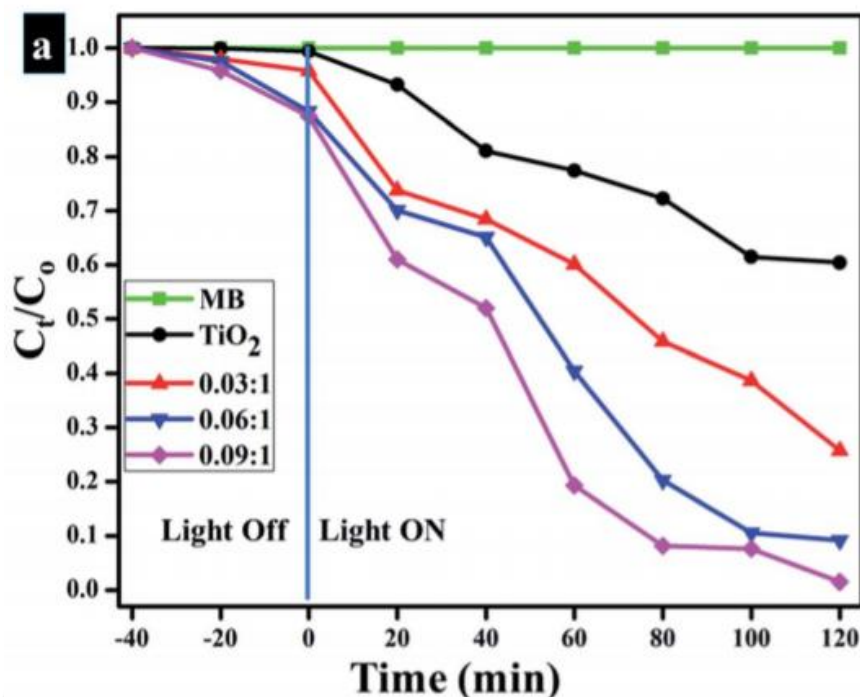


Figure 18 Cu-doped TiO₂ nanoparticles (a) schematic, (b) UV–vis spectra and (c) photocatalytic activity (Ikram et al., 2020).

In addition, Mn ions can be easily incorporated into the TiO₂ lattice to obtain a deformed structure. Mn has some contributions to the TiO₂ conduction band, which impact to TiO₂ narrowed bandgap. Therefore, Mn-doped TiO₂ has a high potential in optical absorption in visible or even infrared and solar light that extends the power of TiO₂ on optical absorption from the limited ultraviolet (Paul, Chetri, & Choudhury, 2014; Shao et al., 2010). Mn-doped TiO₂ nanoparticles can be prepared by several methods, including sol-gel, hydrothermal, ultrasonic synthesis, and impregnation. Several researchers have studied Mn-doped TiO₂ nanoparticles for organic pollutants degradation. Briefly, TiO₂ was doped with various Mn-doping content (0.1% to 2.0%) by the sol-gel method to enhance photocatalytic performance under visible light. 50 mL of 4 mg/l MB concentration was used with 0.1 g of synthesized nanoparticles for evaluating the photodegradation. The results found that 2.0% of Mn doping obtained the highest photocatalytic activity, with 90% MB removal within 3 hours, as shown in Figure 19.

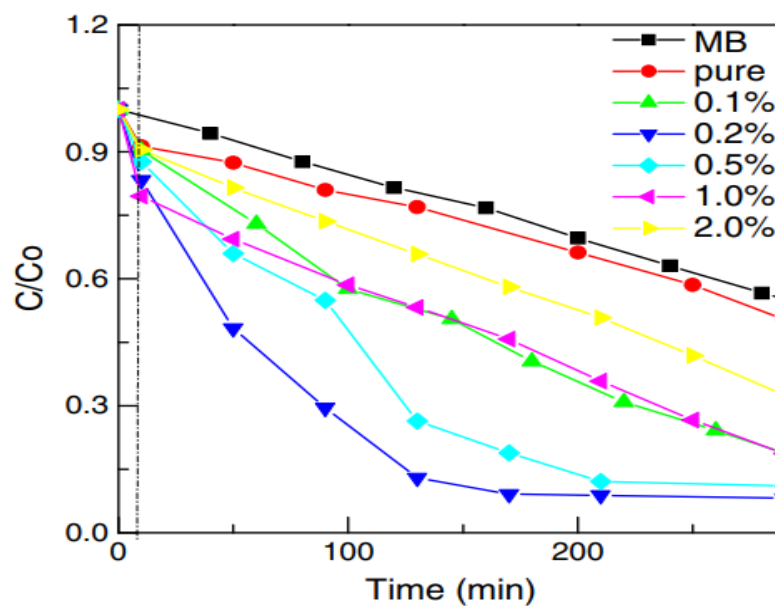


Figure 19 Photodegradation of methylene blue by TiO₂ with different Mn doping under visible light (Deng et al., 2011)

For the other research, TiO₂ doping was studied with 5% of the difference in metal, including Mn, Co and Zr to improve the photocatalytic efficiency of MB and MO dyes under visible light for industrial application (Gnanasekaran et al., 2016). As a result, the Mn-doped TiO₂ catalyst showed the highest photocatalytic activity among the other catalysts. Due to its smaller crystallite size, large surface area and lower band gap. The maximum degradation efficiency of Mn-doped TiO₂ is 65.2% and 73.2% for MO and MB, respectively, were shown in Table 2.

Table 2 Degradation efficiency of undoped and Mn, Co, Zr doping with TiO₂ under UV and visible light.

Samples	Degradation efficiency of MO in 60 min under UV light (%)	Degradation efficiency of MB in 60 min under UV light (%)	Degradation efficiency of MO in 240 min under visible light (%)	Degradation efficiency of MB in 240 min under visible light (%)
Pure TiO ₂	65.3	72.4	4.1	6.2
Mn doped TiO ₂	85.2	93.6	65.2	73.2
Co doped TiO ₂	78.2	86.4	53.2	64.3
Zr doped TiO ₂	70.1	77.3	22.6	38.2

In other research, the photocatalytic activity of organic pollutants, MB and glyphosate, of TiO₂ doping with Mn in different concentrations of 0.15-0.60% were studied (Umar et al., 2016). The results observed that the degradation efficiency of all the pollutants increases with an increasing doping concentration from 0.15 to 0.45%. A further increase in the doping concentration decreases the degradation efficiency. The study observed 0.45% Mn doping content as the best degradation activity, as shown in Figure 20.

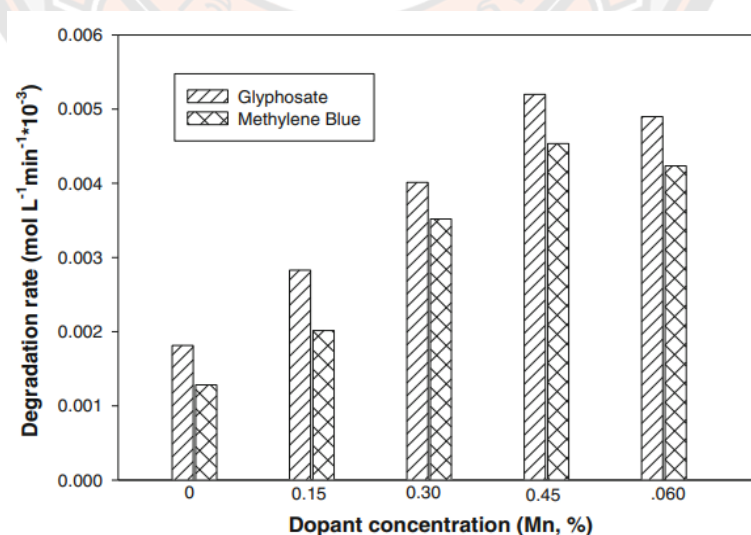
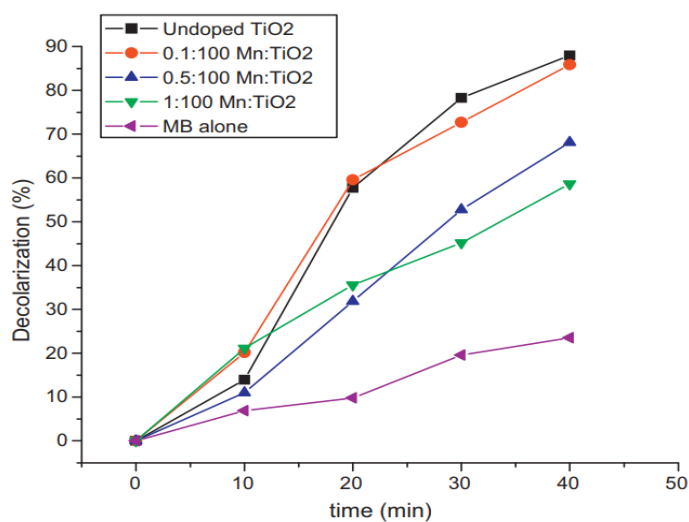
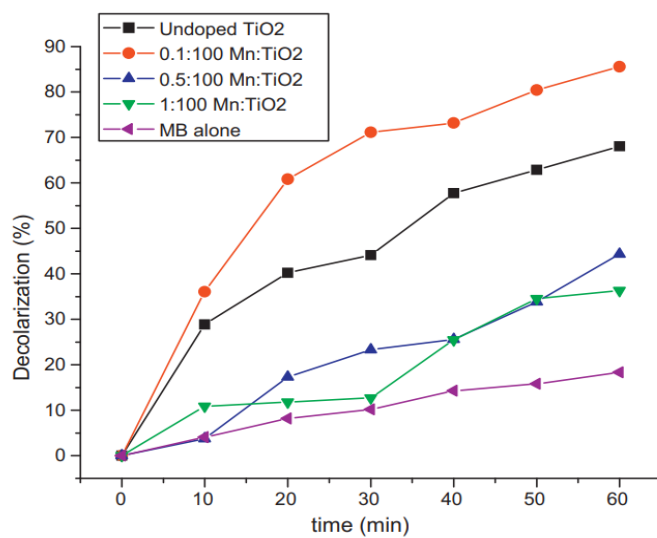


Figure 20 Photocatalytic activity of Mn-doped TiO₂ for glyphosate and methylene blue degradation under visible irradiation 300 minutes (Umar et al., 2016).

In addition, the Mn-doped and undoped TiO₂ photocatalysts were explored by the sol-gel method (Binas et al., 2012). The photocatalytic activity of these materials was evaluated by using methylene blue as an organic contaminant. The best photocatalytic activity was observed in Mn-doped TiO₂ powder with molar ratio 0.1:100, as shown in Figure 21.



(a)



(b)

Figure 21 Photocatalytic activity of Mn-doped TiO₂ for methylene blue degradation under (a) UV and (b) visible irradiation (Binas et al., 2012).

2.5.2 Modification with inorganic acids

It has been demonstrated that surface modification with inorganic acids can significantly improve the surface carried charge properties of TiO₂ photocatalysts in neutral water. Due to it much promotes the adsorption of O₂ on the photocatalyst surface, leading to enhanced photocatalytic activities. TiO₂ nanosheets were modified with sulfuric acid by hydrothermal synthesis. The results found that H₂SO₄-modified TiO₂ exhibits enhanced photocatalytic performance with visible-light irradiation. The mechanism of CO₂ reduction and water oxidation of over-bulk anatase TiO₂ and sulfuric acid-modified TiO₂ nanosheets are shown in Figure 22.

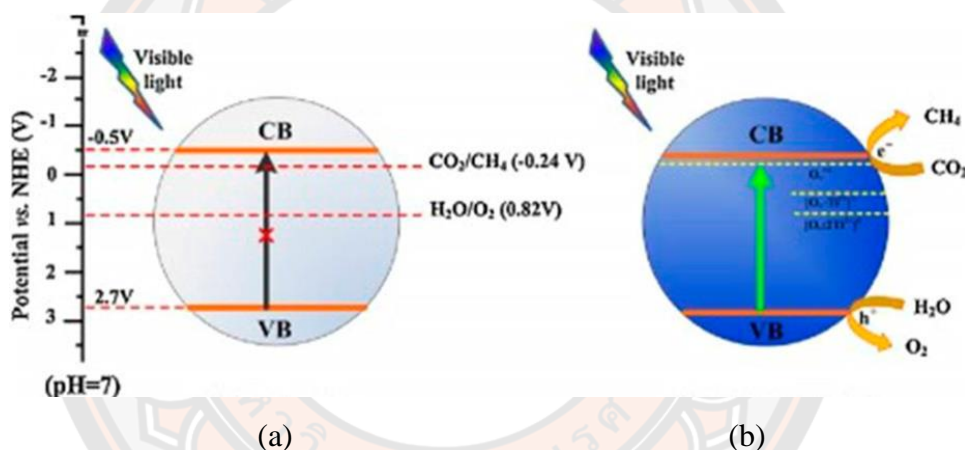


Figure 22 Schematic for the energy band gap of (a) the bulk and (b) sulfuric acid modified anatase TiO₂ (Yang et al., 2008).

In addition, the synthesis of TiO₂ nanoparticles by the hydrothermal method was modified with hydrofluoric acid. The photocatalytic performance is higher than the unmodified TiO₂. The resulting -Ti: F-H bond enhanced the adsorption of O₂ on the surface of TiO₂. Hence, the photogenerated electrons were effectively captured by the adsorbed O₂ and the charge carrier's separation was improved. The residual HF linked to the TiO₂ surface with coordination bond between Ti⁴⁺ and F⁻ are shown in Figure 23.

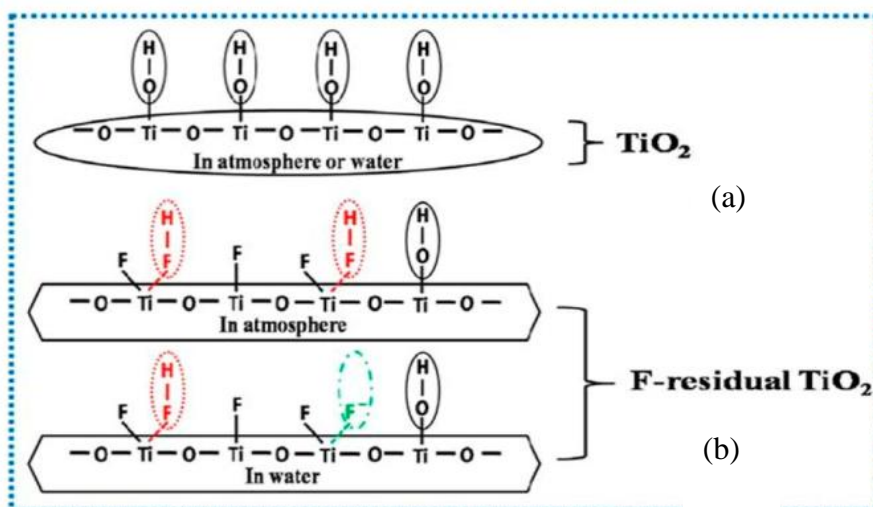


Figure 23 Schematic illustration for the surface structure of (a) unmodified and (b) HF-modified TiO_2 in the atmosphere and water (Walthall & Stark, 1999).

Moreover, some research reported that the cobalt phosphate-modified TiO_2 films greatly enhanced photocatalytic activity. It was attributed to the surface-linked cobalt (II) ions. The schematic mechanism for the holes captured by Co (II) and the improved photoelectrochemical (PEC) water oxidation of TiO_2 after modification with Co (II) phosphate is shown in Figure 24.

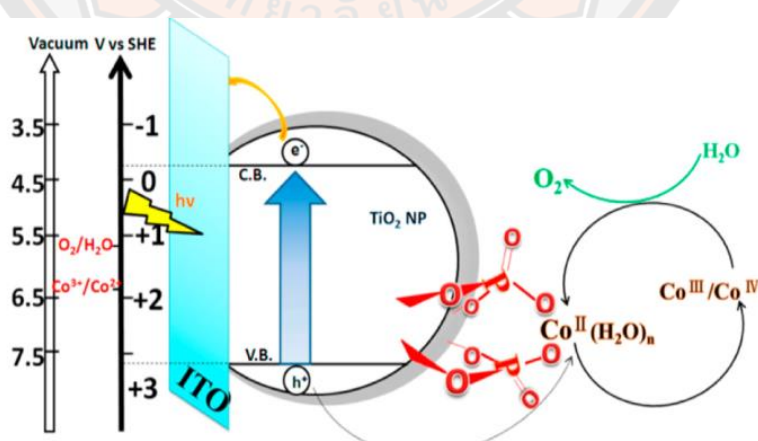
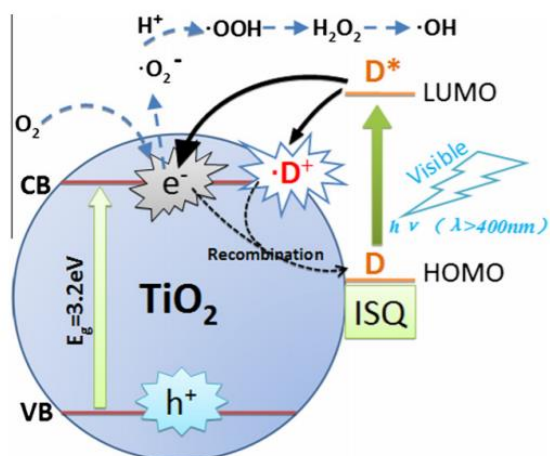


Figure 24 Schematic for photoelectrochemical (PEC) water oxidation by cobalt (II) phosphate-modified TiO_2 . Adapted from reference (Nilsson, Nordlinder, Wass, Meding, & Belin, 1993).

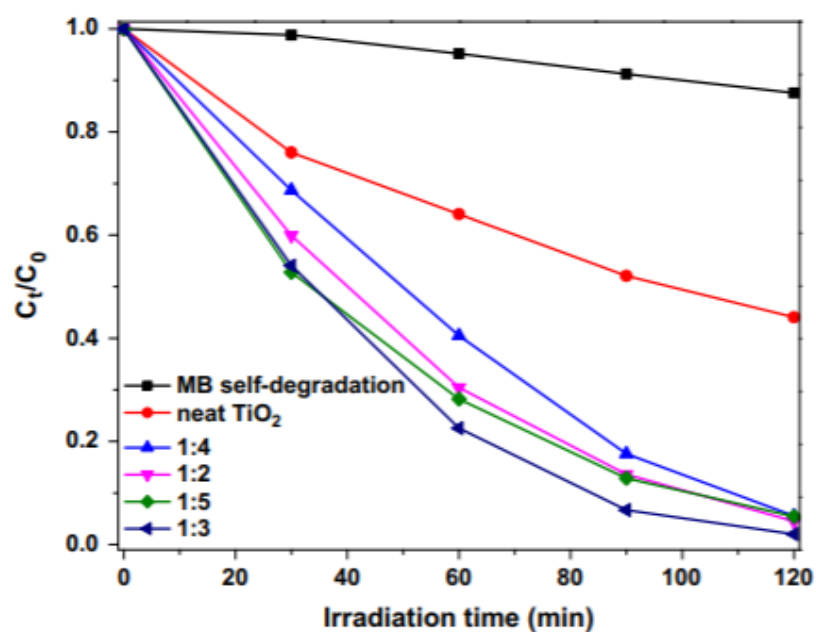
2.5.3 Dye-sensitized TiO₂

Dye-sensitized TiO₂ is an effective technique to utilize sunlight for various organic pollutants oxidation. In this technique, the dye molecules anchored on TiO₂ are excited by solar photons to generate the excited electrons and then transfer them to the conduction band of TiO₂. Subsequently, the electrons in the conduction band of TiO₂ are transported to the interfacial electron acceptors, H₂O, I⁻³, H⁺, O₂ and induce various redox reactions.

A squarylium dye, 1,3-bis[(3,3-dimethylindolin-2-ylidene) methyl] squaraine (ISQ) were sensitized on TiO₂ nanoparticles photocatalysts. In this research, the different mass ratio of ISQ to TiO₂ was studied by blending ISQ and TiO₂ in an ethanol solution. The visible light photocatalytic activities of ISQ sensitized TiO₂ nanoparticles were evaluated for methylene blue (MB) degradation. The results showed that photo-response of the ISQ sensitized TiO₂ nanoparticles enhanced photocatalytic activity under visible light irradiation. The maximum degradation efficiency of MB reached approximately 98% in 2 h under visible light irradiation using the mass ratio of ISQ to TiO₂ was 1:3. The photocatalytic activities and schematic diagram of neat TiO₂ and ISQ/ TiO₂ nanoparticles are shown in Figure 25.



(a)



(b)

Figure 25 Schematic of (a) mechanism and (b) photocatalytic activity of the ISQ sensitized TiO₂ nanoparticles under visible light (Z. Li, Fang, Zhan, & Xu, 2013).

2.5.4 Constructing heterojunctions

TiO₂ semiconductor photocatalyst has a wide band gap with proper VB and CB positions. Therefore, the low quantum yield limits its practical application. Because TiO₂ could absorb only UV light, which accounts for ca. 5% of the solar spectrum. To overcome this shortfall, constructing heterojunctions with noble metals and other semiconductor oxides is widely used.

Constructing heterojunctions could effectively improve the optical absorption, effective separation of photogenerated charges, transfer of energetic electrons and high stability toward photo-corrosion. Therefore, it is highly desirable to choose suitable photocatalysts for coupling in order to improve the stability and efficiency of TiO₂ photocatalysts. Photocatalysts with large surface areas exhibit more active sites, which is crucial for photocatalytic reactions. Besides, the proper band gap and band edge alignment is also a key point because the relative energy level at the interface junction also reveals the charge separation direction and transportation. Based on the above consideration, the heterojunctions are categorized into two classes; noble-metals- TiO₂ heterojunctions and semiconductor oxides- TiO₂ heterojunctions.

2.5.4.1 Noble-metals-TiO₂ heterojunctions

Deposition of noble metals, Ag, Au and Pt, on TiO₂ surface has been reported to improve the photocatalytic in visible-light region due to the surface plasmon resonance (SPR) effect of noble metals. The surface plasmon resonance effect mainly arises from the collective oscillations of electrons on surfaces of noble metal and transfer into the conduction band of the coupled semiconductor due to the Schottky barrier. The schottky barrier between noble metals and semiconductor oxides arises via Fermi levels equilibrium. As a result, built-in electric field is formed at the interface, which favors the separation of photogenerated charges, as depicted in Figure 26.

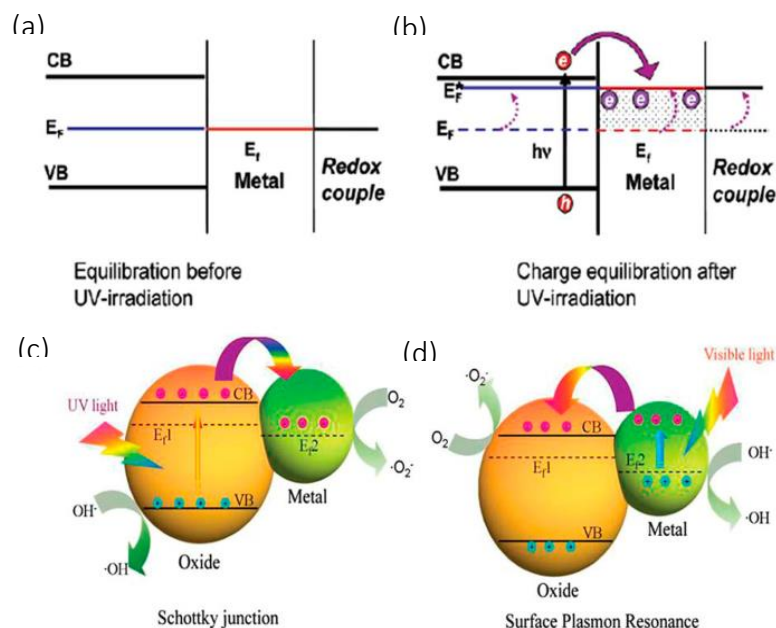


Figure 26 Equilibrium position of semiconductor-Metal nanocomposites with Redox Couple (a) before and (b) after UV irradiation, and schematic of photogenerated charge transfer and separation in semiconductor-metal heterojunctions (c) under UV and (d) visible irradiation.

There are many researches on this material. For example, TiO_2 thin film systems containing noble metal nanoparticles such as Au, Ag, and Cu were prepared using radio frequency reactive magnetron co-sputtering. The photocatalytic activity of all synthesized samples annealed at $600\text{ }^\circ\text{C}$ in an $\text{Ar} + \text{H}_2$ (80 + 20%) environment was evaluated by measuring the rate of photodegradation reaction of methylene blue (MB) under similar conditions in the presence of visible irradiation. The photo enhancement of this research was reported in the following order: $\text{Cu: TiO}_2 > \text{Au: TiO}_2 > \text{Ag: TiO}_2 > \text{TiO}_2$. Moreover, the results are shown in Figure 27.

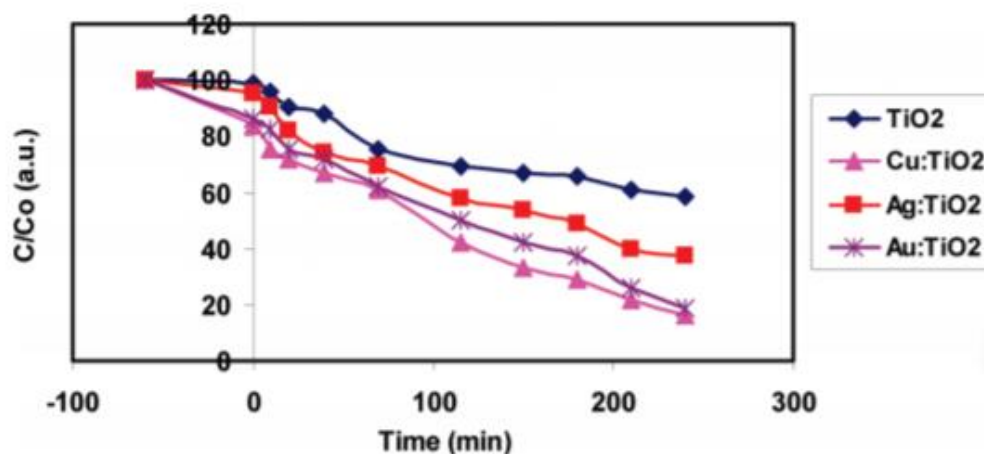


Figure 27 Photocatalytic degradation of methylene blue of TiO₂ thin films containing Au, Ag and Cu nanoparticles (Sangpour, Hashemi, & Moshfegh, 2010).

A series of Ag/TiO₂ with different Ag contents were prepared by the photoreduction method (Tseng & Chen, 2019). The results reported that the photocatalytic activity of 1 wt% Ag is the optimum loading for high activity, as shown in Figure 28. The photocatalytic activity of Ag/TiO₂ decreased when the silver content was more than 1 wt%. As silver concentration is more than the optimum amount, Ag becomes the recombination center of the photoinduced electrons and holes, which is harmful to photocatalytic reactions.

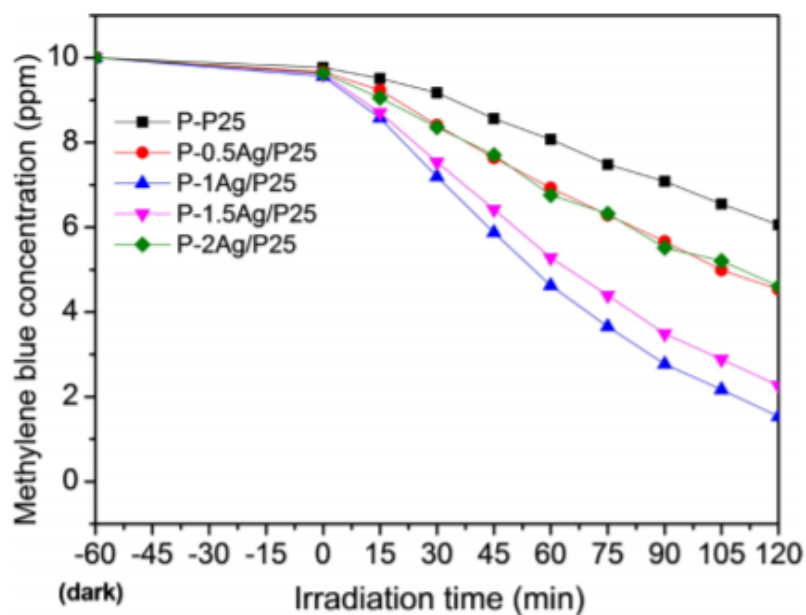


Figure 28 Photocatalytic degradation of methylene blue of Ag/TiO₂ under UV irradiation (Tseng & Chen, 2019).

2.5.4.2 Semiconductors-TiO₂ heterojunctions

Both the semiconductors' components of semiconductors-TiO₂ heterojunctions can be excited by photons to generate charge carriers (electron-hole pairs). The direction of charge transfer would mainly depend on the relative VB and CB positions of both semiconductors. Generally, the heterojunctions between TiO₂ and other semiconductors are classified into three types, as shown in Figure 29.

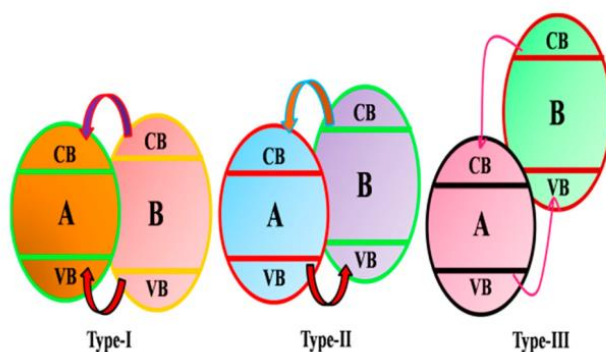


Figure 29 Band gap structures and direction of the charges of semiconductors- TiO₂ heterojunctions.

Heterojunctions with narrow band gap semiconductors efficiently achieve high photocatalytic degradation yields under visible light on dyes. There are several narrow band gap semiconductors. CuO is one of the various narrow band gap semiconductors, which has been appropriated to combine with TiO₂ to enhance visible light absorption and retard the recombination of the photogenerated electrons and holes. CuO is a p-type semiconductor and non-toxic material that is cheap and abundant in the world. It has good optical, electrical, and catalytic properties with a narrow energy gap of 1.2–1.7 eV. Many researchers reported that Cu-doped TiO₂ enhanced photocatalytic activity under UV light irradiation

Several researchers have studied Cu-doped TiO₂ nanoparticles. Cu-doped TiO₂ nanoparticles were prepared by impregnation using TiO₂ powder (Evonik, P25) with different copper content. The photocatalytic degradation for pollutants was efficiently converted to several intermediate and partially mineralized to CO₂ under visible light. The photocatalytic degradation of Gallic acid of Cu-doped TiO₂ composites under visible light is shown in Figure 30 (Luna et al., 2016). Moreover, the specific surface area, pore volume and band gap values of TiO₂ and Cu-doped TiO₂ are shown in Table 3 (Luna et al., 2016).

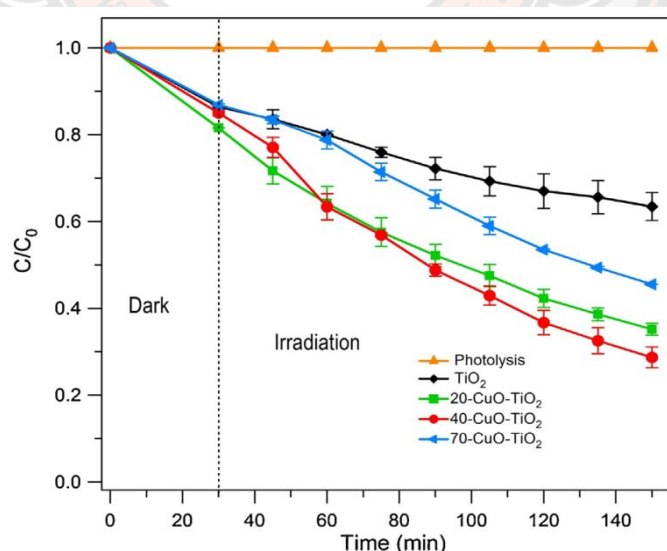


Figure 30 Photocatalytic degradation of Gallic acid of TiO₂ and CuO-TiO₂ composites under visible light.

Table 3 Specific surface area, pore volume and band gap values of TiO₂ and CuO- TiO₂.

Samples	S_{BET} (m ² /g)	Pore volume (mL/g)	Band gap (eV)
TiO ₂	48.3	0.025	3.10
3-CuO-TiO ₂	46.6	0.021	2.56
5-CuO-TiO ₂	36.1	0.017	2.50
10-CuO-TiO ₂	30.2	0.015	2.46
20-CuO-TiO ₂	26.4	0.012	2.40
40-CuO-TiO ₂	23.1	0.005	2.31
70-CuO-TiO ₂	9.2	0.004	2.06

Summaries in this section, due to TiO₂ nanomaterials are widely used as its low-cost, good physical and chemical properties. However, associated with wide band gap (anatase: 3.2 eV, rutile: 3.0 eV), TiO₂ can only absorb ultraviolet light (3-5% solar light). Besides, the electron/holes are fast recombined. These drawbacks make TiO₂ inactive under visible light. Therefore, it needs to modify in order to solve this problem. The common modification strategies and their corresponding purposes include doping (metal and non-metal elements) and heterostructure construction by coupling with noble metal particles and semiconductors. The schematic of the energy level and electron-hole pair separation/transfer of undoped TiO₂ and corresponding modification is shown in Figure 31.

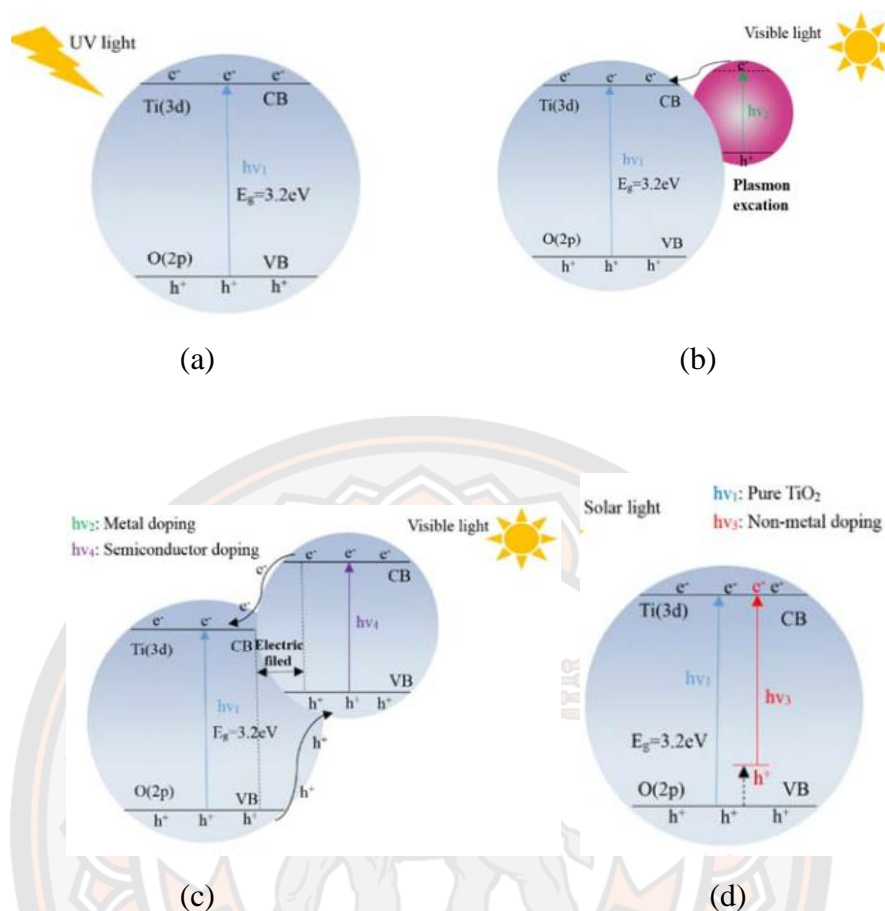


Figure 31 Schematic of energy level and electron-hole pair separation/transfer of undoped TiO₂, (b) semiconductor-TiO₂ heterostructure, (c) metal, and (d) non-metal doping with TiO₂ (Gnanasekaran et al., 2016).

2.6 Operating factors on photocatalytic degradation

According to there are several factors that affect photocatalytic degradation activity. The main factors are light intensity, pH, pollutants concentration, and photocatalyst concentration, described as the following.

2.6.1 Intensity and wavelength of light

TiO₂ has a wide band gap of 3.2 eV for anatase, 3.00 eV for rutile and 3.13 eV for the brookite phase. Therefore, it limits absorption only to the UV region of sunlight. The wavelength and intensity of the UV light irradiation source affect the degradation of dye in an aqueous solution using TiO₂ photocatalyst powder in the

photocatalytic reactor. The artificial UV irradiation is more reproducible than sunlight and can bring higher efficiency in the degradation of textile dyes. However, because of its abundance and non-hazardous nature, solar energy is expected to emerge as an alternative, cost-effective light source.

In the past decade, the effect of light intensity on photocatalytic dye degradation has been widely studied. Several studies have reported that the light intensity led to improve rate of photocatalytic degradation. When the light intensity increased from 16 to 32 W, the photocatalytic degradation increased above 33% (Bhati, Punjabi, & Ameta, 2010).

2.6.2 pH

One of the significant parameters for photocatalytic dye degradation is pH. Many researchers report that the pH effect is related to the surface-charge properties of the photocatalysts. The pH of the solution can influence dye adsorption onto the semiconductor surface as the catalyst surface charge depends on the pH of a given solution. The point of zero charges (pH_{pzc}) value for TiO_2 particles is 6.8.

For example, the photocatalytic degradation of methylene blue with the difference in pH solution was observed (Bubacz, Choina, Dolat, & Morawski, 2010). The result found that the photocatalytic activity increased with an increase in pH. According to electrostatic interactions between negative TiO^- and methylene blue cation leads to strong adsorption with a correspondingly high degradation rate. In acidic solutions, the photodegradation of the dye is retarded by the high proton concentration, resulting in lower degradation efficiency.

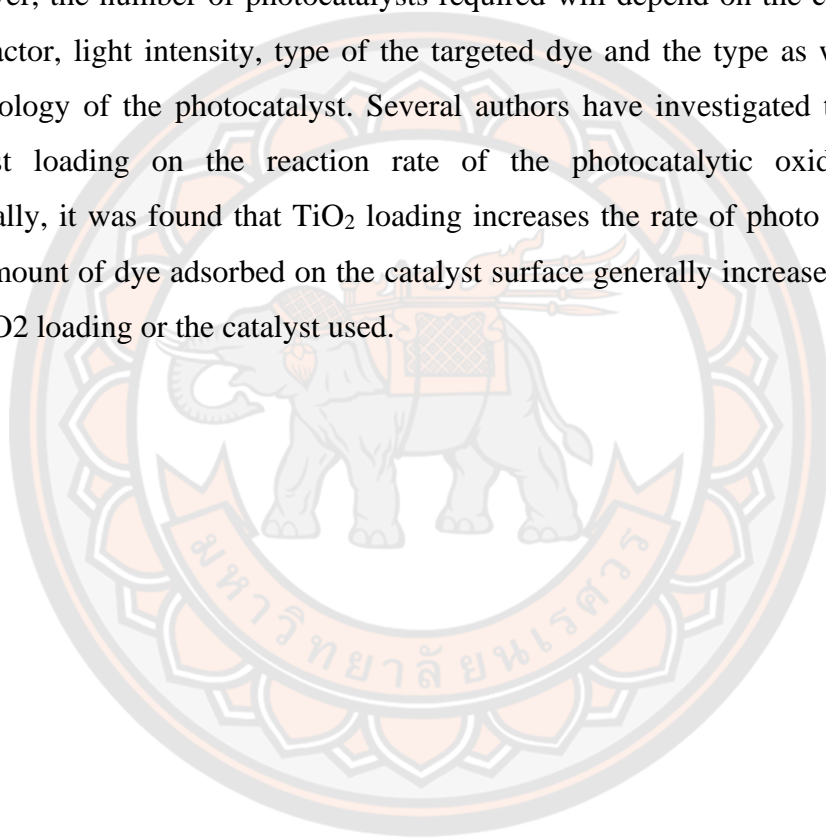
2.6.3 Pollutants concentration

The effect of dye concentration has been studied. It has been reported that the decolorization rate constant (k) decreases by increasing the dye concentration. The initial dye concentration can affect the rate of photodegradation. In similar results, a higher initial concentration of methyl orange made fewer photons reach the catalyst surface due to the reduction of light penetration. As the initial dye concentration increases, the photocatalytic degradation efficiency decreases because more dye

molecules compete, leading to increased turbidity. Furthermore, a high dye concentration makes the dye itself absorb light more than a photocatalyst.

2.6.4 Photocatalyst concentration

The photocatalyst load in a dye suspension significantly affects the rate of dye photodegradation. In order to avoid the excessive use of the catalyst, it is necessary to find out the optimum dose or loading of the catalyst for the efficient removal of dye. However, the number of photocatalysts required will depend on the configuration of the reactor, light intensity, type of the targeted dye and the type as well as particle morphology of the photocatalyst. Several authors have investigated the function of catalyst loading on the reaction rate of the photocatalytic oxidation process. Generally, it was found that TiO_2 loading increases the rate of photo decolorization. The amount of dye adsorbed on the catalyst surface generally increases by increasing the TiO_2 loading or the catalyst used.



CHAPTER III

RESEARCH METHODOLOGY

The research methodology of this study was divided into three parts, summarized in Figure 32, as the following:

- 1) Synthesis of the nanoparticles, including undoped TiO₂, Cu-doped TiO₂ and Mn-doped TiO₂ nanoparticles.
- 2) Characterization in physico-chemical properties of the synthesized nanoparticles using X-ray diffraction (XRD), scanning electron microscopy (SEM), transmission electron microscopy (TEM) and Brunauer-Emmett-Teller method (BET).
- 3) Investigation of the photocatalytic on dyes (MB), drugs (SAL) degradation, and *E.coli* photokilling under UV and visible light.

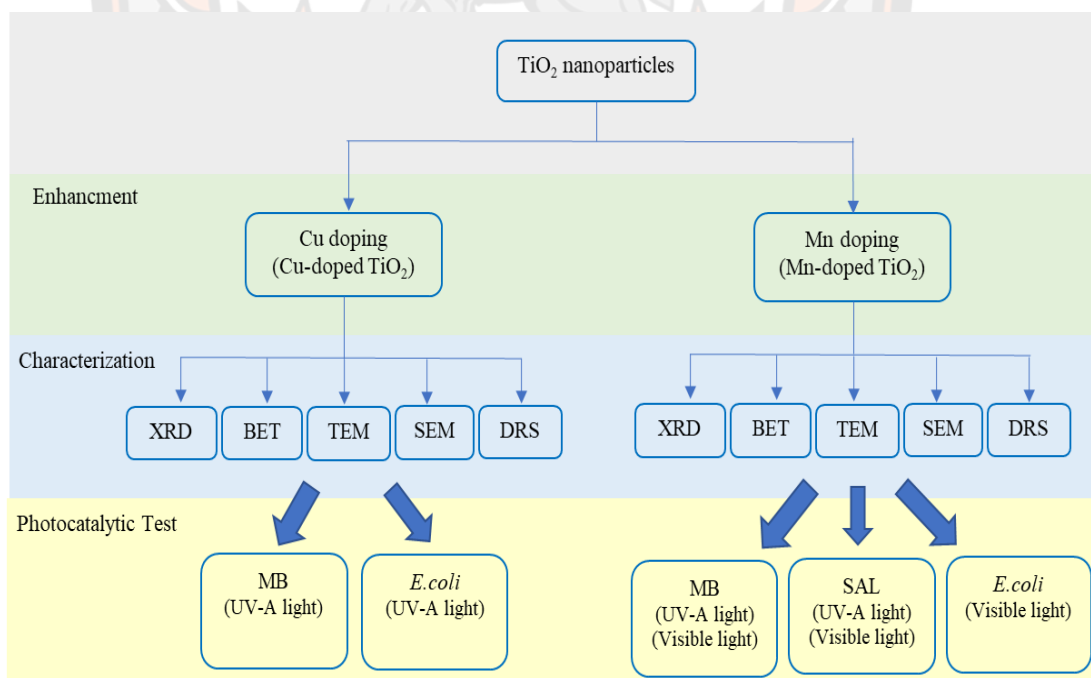


Figure 32 Summarization of research methodology.

3.1 Synthesis of the nanoparticles

3.1.1 Synthesis of undoped TiO₂

TiO₂ nanoparticles were synthesized with the hydrothermal method. The preparation steps are shown as described below in Figure 33. At first, 4 mL of titanium tetraisopropoxide and 20 mL of ethanal were mixed and stirred at room temperature for 1 hour. Afterward, the mixture was transferred to an autoclave and maintained at 180°C for 12 hours. Finally, the sample was washed with ethanol 2 times and deionized (DI) water 3 times. The TiO₂ nanoparticles were separated from the solution by centrifuge and dried at 100 °C for 24 hours

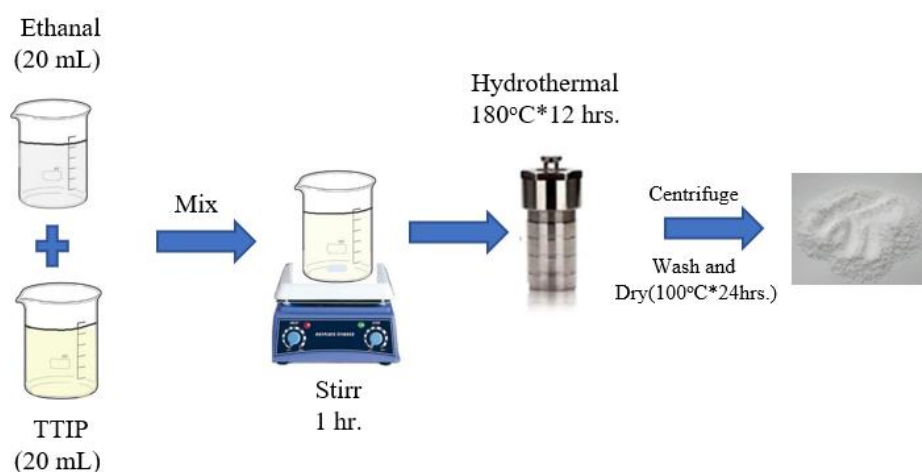


Figure 33 Preparation of undoped TiO₂ nanoparticle by hydrothermal method.

3.1.2 Synthesis of CuO

CuO nanoparticles were synthesized using a sol-gel method. This synthesis dissolved 0.025 mol of CuSO₄·5H₂O in 100 mL of DI water with constant magnetic stirring. Then, 0.05 mol of NaOH in 150 mL of DI water was added to the solution until a pH value of 12. Subsequently, the solution was maintained at 80 °C with stirring for 3 hours to form a gel. It was dried at 80 °C for 4 hours and then annealed at 125 °C for 8 hours. The synthesis of CuO nanoparticles shows in Figure 34.

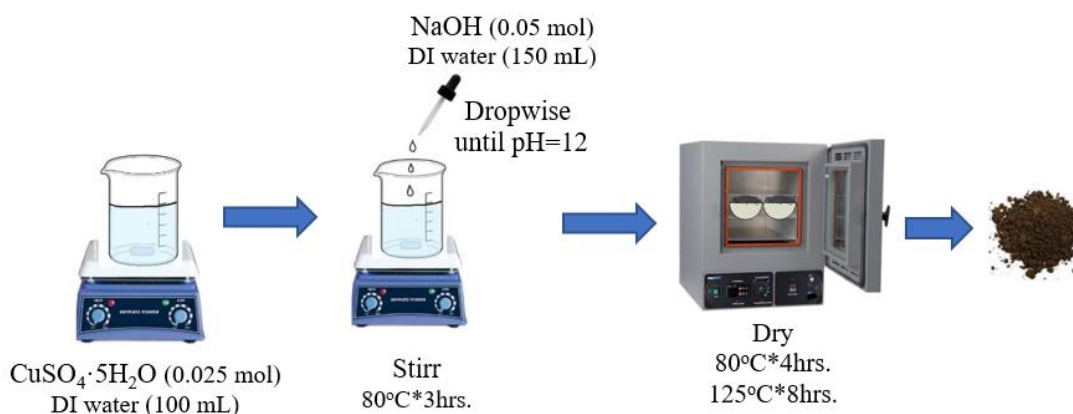


Figure 34 Preparation of CuO nanoparticles.

3.1.3 Synthesis of Cu-doped TiO_2

Cu-doped TiO_2 nanoparticles were synthesized by the sol-gel method. Typically, 0.0125 mol of TiO_2 was dissolved in 30 mL DI water under stirring. After that, 0.0125 mol of NaOH dropwise into the TiO_2 solution until a pH value of 12. The reaction temperature was kept at 80°C . During the same time, various CuO nanoparticles were separately dispersed in 30 mL of DI water. Subsequently, CuO dispersion was introduced into the TiO_2 solution. The solution was continuously stirred at 80°C for 2 hours. Later, the precipitated sample was collected by centrifugation and aged overnight. Then the sample was washed with DI water until a pH of 7. The final products were dried at 100°C for 1 hour under vacuum conditions. In this research, the Cu content of the Cu-doped TiO_2 nanoparticles varied as 0.1, 0.5, and 1.0 wt%. The preparation of Cu-doped TiO_2 nanoparticles shows in Figure 35.

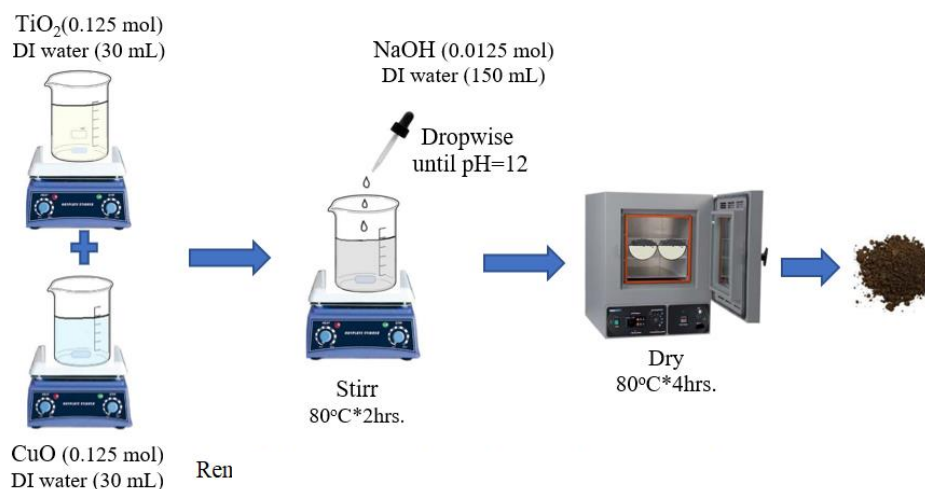


Figure 35 Preparation of Cu-doped TiO_2 nanoparticles.

3.1.4 Synthesis of Mn-doped TiO_2

Undoped TiO_2 and Mn-doped TiO_2 nanoparticles were prepared by the sol-gel method. Titanium tetraisopropoxide (TTIP) and 2-propanol were added together in 1:1 with continuous stirring. For Mn-doped TiO_2 , the complete dissolution of $\text{MnCl}_2 \cdot 4\text{H}_2\text{O}$ in DI water with different content, including 0.05%, 0.10%, and 0.20% Mn was added to TTIP and 2-propanol mixture. The mixture was adjusted the pH value at 2 by HNO_3 dropwise and stirred for 4 hours. After that, the blend aged at 55°C for 24 hours and calcinated at 400°C for 2 hours.

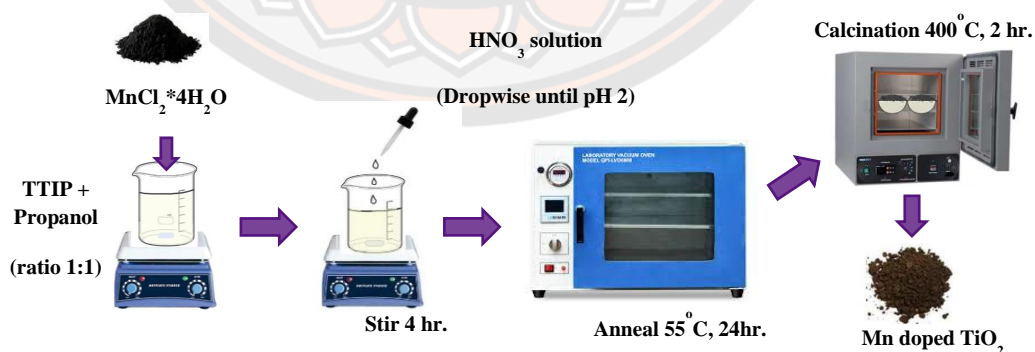


Figure 36 Preparation of Mn-doped TiO_2 nanoparticles.

The synthesis of nanoparticles, including Cu-doped, Mn-doped and undoped TiO_2 were summarized in Table 4.

Table 4 Summary of synthesis of nanoparticles.

Nanoparticles	Amount of chemicals				Preparation method
	TiO ₂ (g)	CuO (g)	TTIP (mL)	MnCl ₂ ·4H ₂ O (g)	
TiO ₂	2.0000	-	-	-	Hydrothermal
0.1%Cu-doped TiO ₂	1.9980	0.0020	-	-	Hydrothermal
0.5%Cu-doped TiO ₂	1.9900	0.0100	-	-	Hydrothermal
1.0%Cu-doped TiO ₂	1.9800	0.0200	-	-	Hydrothermal
TiO ₂	-	-	50	0.0000	Sol-gel
0.1%Mn-doped TiO ₂	-	-	50	0.0291	Sol-gel
0.2%Mn-doped TiO ₂	-	-	50	0.0582	Sol-gel
0.3%Mn-doped TiO ₂	-	-	50	0.0874	Sol-gel

3.2 Characterization of the synthesized nanoparticles

The synthesized nanoparticles were characterized Physico-chemical by X-ray diffraction (XRD) to identify the crystal structure of nanocomposites. The shape and form on the surface of the nanoparticles were observed using a scanning electron microscopy (SEM) instrument. In addition, energy dispersive X-ray (EDX) examined elemental analyses of the nanocomposites. Transmission electron microscopy (TEM) was also used to explore the size and distribution of the nanocomposites. Moreover, the total surface areas of the samples were determined by the Brunauer-Emmett-Teller (BET) methods. Besides, the optical band gap of nanoparticles was determined using diffuse reflection spectroscopy. The characterization in physico-chemical properties of the synthesized nanoparticles was summarized shown in Table 5.

Table 5 Summary of the characterization of the synthesized nanoparticles.

Property of nanoparticles	Analytical instruments
Crystalline structure	X-ray diffraction (XRD)
Shape and form on the surface	Scanning electron microscopy (SEM)
Size and distribution	Transmission electron microscopy (TEM)
Elemental composition	Energy dispersive X-ray (EDX)
Specific surface areas, pore size, and pore volume	Brunauer-Emmett-Teller (BET)

The crystal structure of the undoped and metal-doped TiO₂ nanocomposites was determined by X-ray diffraction (XRD, BRUKER, D2 Phaser) operating with Cu K_α radiation ($\lambda = 0.154$ nm) in the range of 20°-80°. The crystallite size of the nanocomposites was determined using Debye–Scherrer formula (Cullity & Graham, 2011):

$$D = \frac{K\lambda}{\beta \cos\theta}$$

Where D is the crystallite size, K is the shape factor (0.9), λ is the wavelength of X-ray radiation, and β is the full width at the half maximum (FWHM) of the diffraction peak.

The lattice parameters of a tetragonal structure were calculated by the following formula (Ganesh et al., 2012):

$$\frac{1}{d^2} = \frac{h^2 + k^2}{a^2} + \frac{l^2}{c^2}$$

Where d is the interplanar distance corresponding to the miller indices h , k , and l , while a and c are the lattice constants. The lattice constants of all the samples were calculated using (101) and (110) peaks of the anatase and rutile phases, respectively.

The percentage of anatase structure relative to rutile structure for the nanoparticles was calculated using the Spurr equation:

$$W_A(\%) = \frac{100}{1+1.265\left(\frac{I_R}{I_A}\right)} ; \quad W_R(\%) = \frac{100}{1+0.8\left(\frac{I_A}{I_R}\right)} ,$$

where W_A is the weight fractions of the anatase phase, W_R is the weight fractions of the rutile phase ($W_A = 1 - W_R$), I_A is the intensity of the anatase (101) peak at $2\theta = 25.3^\circ$ and I_R is the intensity of the rutile (110) peak at $2\theta = 27.4^\circ$.

The morphologies of the nanoparticles were studied using a scanning electron microscope (SEM, JSM-6335F, JEOL). In addition, the sample's elements were also analyzed by energy dispersive X-ray (EDX).

Transmission electron microscopy (TEM) was also performed using JEOL/JEM-2100Plus and operating at 100kV.

The BET analysis was performed using TriStar II 3020 Micromeritics with nitrogen adsorption-desorption analysis at 77 K. And the specific surface area was calculated by the Brunauer-Emmett-Teller (BET) method.

The method adopted to acquire the absorption spectra of powder samples in DRS mode is that of Kubelka-Munk. The band gap energy of the nanoparticles was estimated using diffuse reflectance UV-Visible spectroscopy (DRS: Shimadzu, UV-360) with an integrating sphere attachment (ISR-3100, Shimadzu; Japan). The band

gap energy was calculated using a Tauc plot from the DRS spectrum (Tseng & Chen, 2019). For band gap energy determination, $[F(R)hv]^{1/2}$ is plotted against hv as y and x-axis, respectively. The line is drawn on the linear part of $[F(R)hv]^{1/2}$ vs. hv curve at $[F(R)hv]^{1/2} = 0$ gives the band gap.

The band gap energy is typically determined from diffuse reflectance spectra. The measured reflectance spectra can be transformed into the corresponding absorption spectra by applying the theory of P. Kubelka and F. Munk (Kubelka-Munk) presented in 1931 (Kubelka & Munk, 1931). The Kubelka–Munk function (F(R)) is shown in the equation below.

$$F(R) = \frac{K}{S} = \frac{(1 - R)^2}{2R}$$

Where $R = \frac{R_{sample}}{R_{standard}}$ is the reflectance of an infinitely thick specimen, while K is the absorption coefficient and S is the scattering coefficient (López & Gómez, 2012). For hv is the photon energy, $hv = 1240/\lambda$ eV, where λ is the wavelength in nanometers.

3.3 Photocatalytic activity test

3.3.1 Dyes degradation

The photocatalytic degradation of methylene blue (MB) was investigated under UV-A (365 nm, single wavelength) at room temperature in the reactor with magnetic stirring at 250 rpm. In typical processes, 3 mg/L MB solution was prepared in DI water. The nanoparticles were dispersed in the MB solution at a 1 g/L concentration; 50 mg of the photocatalyst nanoparticles were added to 50 mL of MB solution and put in the dark reactor under stirring for 30 min to reach adsorption equilibrium. The solution was taken out in time. After adsorption equilibrium, the solution in the reactor was irradiated and taken every 5 minutes until 30 minutes. During the degradation, the dye solution with photocatalyst was continuously stirred. The remaining MB concentration taken out in the time was measured with UV-VIS spectroscopy (UV-6100, Mapada; China). Since the wavelength of absorbance maximum of MB (λ_{max}) was observed at 664 nm. The photocatalytic reactor under UV-A light is shown in Figure 37.

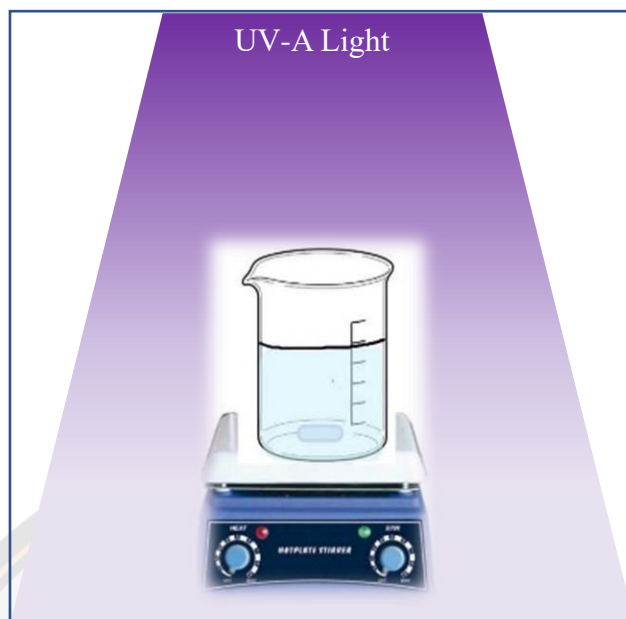


Figure 37 Photocatalytic reactor under UV-A irradiation.

3.3.2 Drugs degradation

The salbutamol (SAL) photocatalytic degradation was examined under UV-A and visible irradiation at room temperature with 250 rpm magnetic stirring in the reactor. Briefly, the salbutamol solution was prepared in DI water at a 15 mg/L concentration. The nanoparticles were dispersed in the solution at a 1 g/L concentration; 50 mg of the photocatalyst nanoparticles were added to 50 mL of SAL solution and put in the dark reactor under stirring for 60 min to reach adsorption equilibrium.

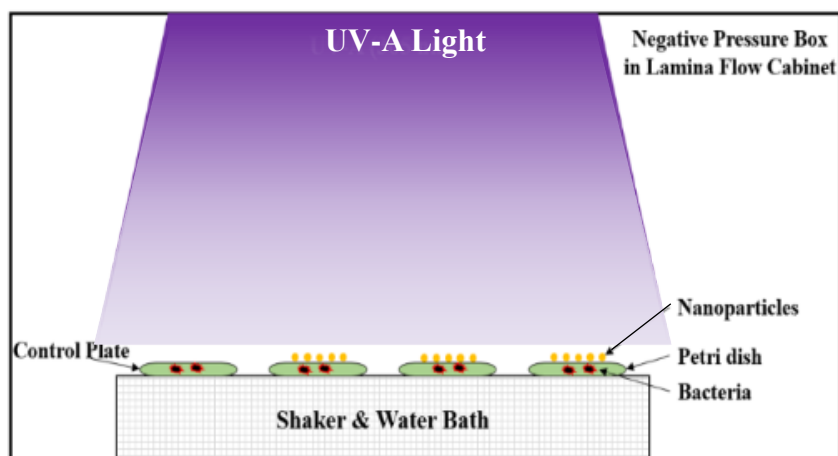
After adsorption equilibrium, the solution in the reactor was irradiated and taken out at the time following 15, 30, 45, 60, 90, 120, 180, and 240 minutes. During the degradation, the solution with the photocatalyst nanoparticles was continuously stirred. The remaining salbutamol solution, as the solution taken in the time, was measured with UV-Vis spectroscopy (UV-6100, Mapada; China). Since the wavelength of absorbance maximum of salbutamol (λ_{\max}) was observed at 276 nm. The photocatalytic reactor under visible light is shown in Figure 38.



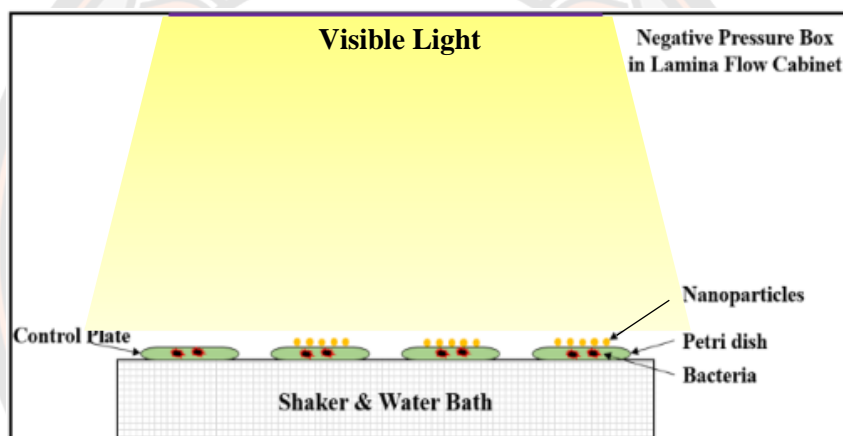
Figure 38 Photocatalytic reactor under visible irradiation.

3.3.3 Microbial photokilling

Escherichia coli (*E. coli*) TISTR117 (from Thailand Institute of Scientific and Technological Research), was used for representing Gram-negative bacteria as indicator strains for a photokilling evaluation of the nanoparticles. The bacteria's initial concentration of 10^7 CFU/mL was used in this research. The indicator strain was grown in nutrient broth at 30°C for 16–18 hours to obtain the initial concentration. After that, the bacteria culture was diluted in DI water. The treated samples, 0.025 g of undoped TiO₂ and 0.1 wt.%, 0.5 wt.% and 1.0 wt.% Cu-doped TiO₂ was used for treatment with 10 mL of bacterial suspensions. The untreated samples, the bacteria suspension without the nanoparticles, represent this study's control sample. Both treated and untreated samples were activated under UV-A (10 W) irradiation for 0, 30, 60, 120 and 180 min on the stirring platform in the reactor. The layout of the reactor in these experiments is presented in Figure 39.



(a)



(b)

Figure 39 Photo-killing experimental setup under (a) UV and (b) visible light.

3.4 Calculation

3.4.1 Degradation efficiency

The photocatalytic activity analysis of all the samples, before and after irradiation, was calculated by measuring the MB and salbutamol removal efficiency (R%) as the following equation;

$$\%R = \frac{A_0 - A}{A_0} \times 100\%$$

where A_0 is the initial absorbance or concentration of pollutants and A is the final absorbance or concentration absorbance of pollutants after irradiation of the samples in the desired time interval.

3.4.2 Antimicrobial efficiency

The cell growth was observed by plating 100 μL of treated and untreated samples on the nutrient agar in chronological order and incubating them at 30 °C for 24 h. The number of visible colonies was counted, and the bacteria viability was determined by plotting the log of visible counts (CFU/mL) against incubation time under UV-A radiation.

3.4.3 Intermediate compound identification

The potential intermediates during photocatalytic degradation of salbutamol were identified using high performance liquid chromatography-mass spectrometry (HPLC-MS). The HPLC-MS was performed on an Agilent 1260 infinity series HPLC system (Agilent, Waldron, Germany) coupled with Agilent 6540 Q-TOF LC-MS spectrometer (Agilent Technologies, Santa Clara, CA, USA). Moreover, the C-18 column was used as Luna C18 column, 4.6 mm \times 150 mm, 5 μm (Phenomenex Inc., Torrance, CA, USA). The mobile phase was 0.1% (v/v) formic acid in the water, mobile phase A, and 50% (v/v) acetonitrile in methanol, mobile phase B. The linear gradient elution was 5-95% for solvent B starting at 0-15 min and post-run for 5 min. The flow rate was 0.5 mL/min, and the injection volume of the sample was 5 μL . Mass Hunter software (Agilent Technologies) controlled all the acquisition and analysis of data. All samples were analyzed in positive mode to provide information for identification.

CHAPTER IV

RESULTS AND DISCUSSIONS

The main of this research was to evaluate the synthesized nanoparticles including Cu-doped and Mn-doped TiO₂ nanoparticles. The nanoparticles were characterized by X-ray diffraction (XRD), scanning electron microscopic (SEM), energy dispersive x-ray (EDX) spectroscopy, transmission electron microscopy (TEM), Brunauer-Emmett-Teller (BET) and diffuse reflectance UV-Visible spectroscopy (DRS). In addition, the photocatalytic degradation efficiency for MB and salbutamol removal and *E. coli* photokilling activity were carried out. All of the results show in the following.

4.1 Characterization of Cu-doped TiO₂ nanoparticles

4.1.1. Crystalline structure

The diffraction peaks of undoped TiO₂ and Cu-doped TiO₂ nanoparticles are shown in Figure 40. From the XRD patterns of undoped TiO₂, the prominent peaks have been allocated at 2θ of 25.35° (101), 38.10° (004), 48.05° (200), 54.55° (105), and 62.60° (204), which refers the anatase phase as a major phase, and brookite, as a minor phase with peaks have been allocated at 2θ of 31.11° refer to Anatase: ICDD card no. 00-064-0863 and Brookite: ICDD card no. 01-071-4943. The Cu diffraction peaks are not observed in the XRD pattern of Cu-doped TiO₂. This result indicates that copper oxide species are well dispersed on titanium structures (Aksay et al.; Xu, Dong, & Chen, 1998) and/or the CuO content was relatively low compared to the TiO₂ content in the nanocomposites (Lee, Hasan, Lintang, Shamsuddin, & Yuliati, 2016). Figure 40 clearly shows that the intensity of Cu-doped TiO₂ peaks is higher than undoped TiO₂, which indicates that CuO doping enhances the crystallinity and improves the structural quality of TiO₂. The XRD results indicate that the degree of crystallinity increased as doping increased. The reason is that Cu can help promote the anatase structure due to it is well-known as a promoter in the grain growth structure (Hanaor & Sorrell, 2011).

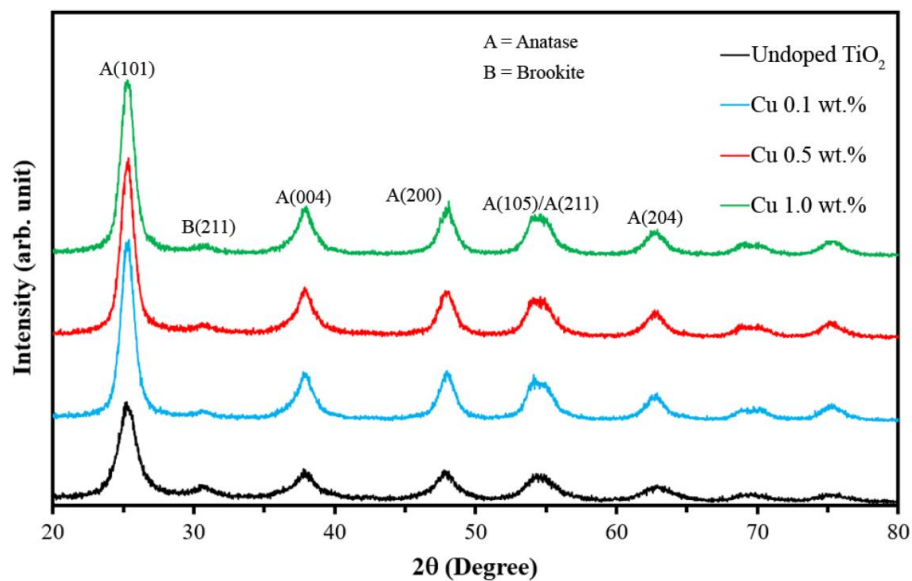


Figure 40 XRD patterns of undoped TiO₂ and Cu-doped TiO₂ nanoparticles.

From XRD data, the lattice parameter and crystallite size were calculated, as shown in Table 6. The lattice parameter results indicate that the unit cell is slightly shirked with increasing Cu doping content due to the replacement of the Ti⁴⁺ with the Cu²⁺. Because the ionic radius of Ti is 0.61 Å and of Cu is 0.57 Å (Shannon, 1976), the unit cell will be compressed. The crystallite size of all the samples is approximately 7 nm. Therefore, these nanoparticles form a single-grain particle.

Table 6 Lattice parameters of undoped and Cu-doped TiO₂ nanoparticles.

Nanoparticles	Anatase phase		Crystal size (nm)
	a=b (Å)	c (Å)	
TiO ₂	3.786	9.503	7.73
0.1%Cu-doped TiO ₂	3.787	9.496	7.86
0.5%Cu-doped TiO ₂	3.787	9.488	7.82
1.0%Cu-doped TiO ₂	3.788	9.484	7.34

4.1.2 Specific surface area

The specific surface area of undoped TiO₂ and Cu-doped TiO₂ nanoparticles, including Cu content from 0.1, 0.5 and 1.0%, is shown in Table 7. The results found that the Cu-doped TiO₂ nanoparticles contained a slightly lower surface area than the undoped TiO₂ nanoparticle. Moreover, the specific surface area was slightly decreasing with increasing Cu percentages. Since Cu and the TiO₂ agglomeration occupied the TiO₂ surface, the available adsorption surface area of the nanoparticles was reduced (S. D. Wu, Zhu, Li, & Wei, 2011).

Table 7 The specific surface area of undoped and Cu-doped TiO₂.

Nanoparticles	Specific surface area (m ² /g)
TiO ₂	182.32
0.1% Cu-doped TiO ₂	181.39
0.5% Cu-doped TiO ₂	180.20
1.0% Cu-doped TiO ₂	180.01

4.1.3 Surface morphology

TEM images of the undoped and Cu-doped TiO₂ nanoparticles are presented in Figure 41. The TEM images show no significant difference in the morphology between the undoped and Cu-doped TiO₂ nanoparticles. The undoped and Cu-doped TiO₂ nanoparticles had consistent particle sizes of approximately 10 nm showing similar particle sizes to the Cu-doped undoped TiO₂ nanoparticles, in agreement with the XRD result, which shows no difference in crystallite size between the undoped and TiO₂ nanoparticles.

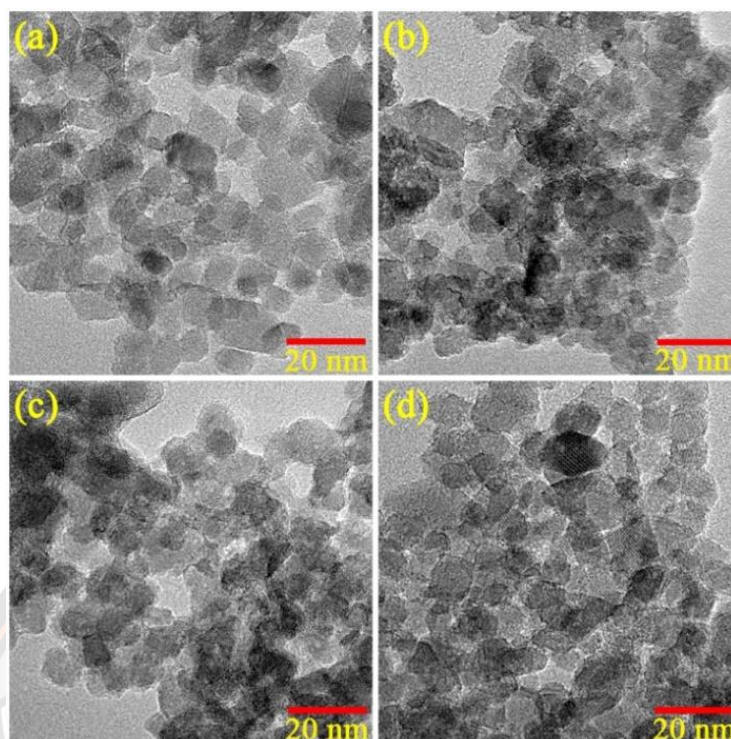


Figure 41 TEM images of (a) undoped, (b) 0.1 wt.% (c) 0.5 wt.%, and (d) 1.0 wt.% Cu-doped TiO₂ nanoparticles.

Figure 42 illustrates the scanning electron microscopy (SEM) images of undoped and Cu-doped TiO₂ nanoparticles at different Cu doping concentrations. The results demonstrate that the Cu-doped TiO₂ nanocomposites agglomerate with increasing CuO doping contents. Because Cu is known as a promoter, it can result in particle agglomeration when Cu forms on the surface of TiO₂ (Hanaor & Sorrell, 2011).

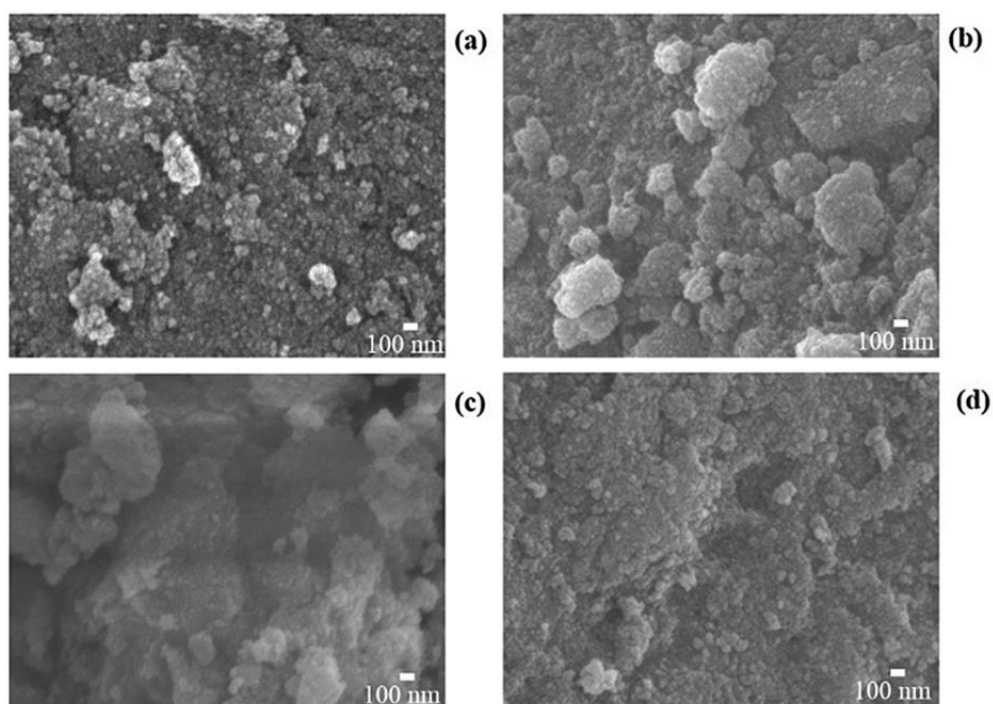


Figure 42 SEM images of (a) undoped, (b) 0.1 wt.% (c) 0.5 wt.%, and (d) 1.0 wt.% Cu-doped TiO₂ nanoparticles.

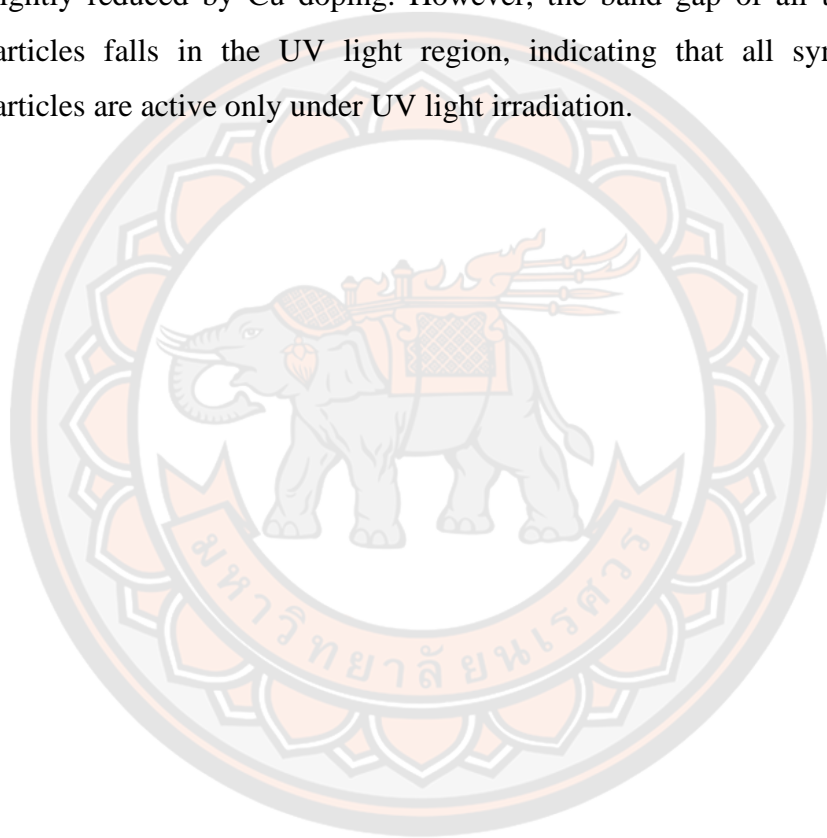
The elemental of the synthesized nanoparticles was examined using energy dispersive X-Ray (EDX) spectroscopy. The EDX data confirm the presence of Cu and TiO₂ in the sample, as shown in Table 8. However, due to the instrument's detection limit, the atomic ratio of Cu in TiO₂ determined from EDX spectra is found to have no significant Cu concentration.

Table 8 EDX analytical data of undoped and Cu-doped TiO₂.

Nanoparticles	Atomic percentages		
	Ti	O	Cu
TiO ₂	32.92%	67.08%	0.00%
0.1% Cu-doped TiO ₂	27.24%	72.12%	0.64%
0.5% Cu-doped TiO ₂	31.88%	67.32%	0.80%
1.0% Cu-doped TiO ₂	26.31%	72.85%	0.84%

4.1.4 Band gap energy

The band gap energy of the undoped and Cu-doped TiO₂ nanoparticles was calculated using a Tauc plot from the DRS spectrum, as shown in Figure 43. As the Tauc plot from the DRS spectrum, $h\nu$ is plotted against $[F(R)h\nu]^{1/2}$ as the x and y-axis, respectively. The tangent's intercept to the curve approximates the direct band gap energy of the nanoparticles. In addition, the band gap energy of the nanoparticles from the Tauc plot was summarized in Table 9. The results showed that the band gap was slightly reduced by Cu doping. However, the band gap of all the synthesized nanoparticles falls in the UV light region, indicating that all synthesized TiO₂ nanoparticles are active only under UV light irradiation.



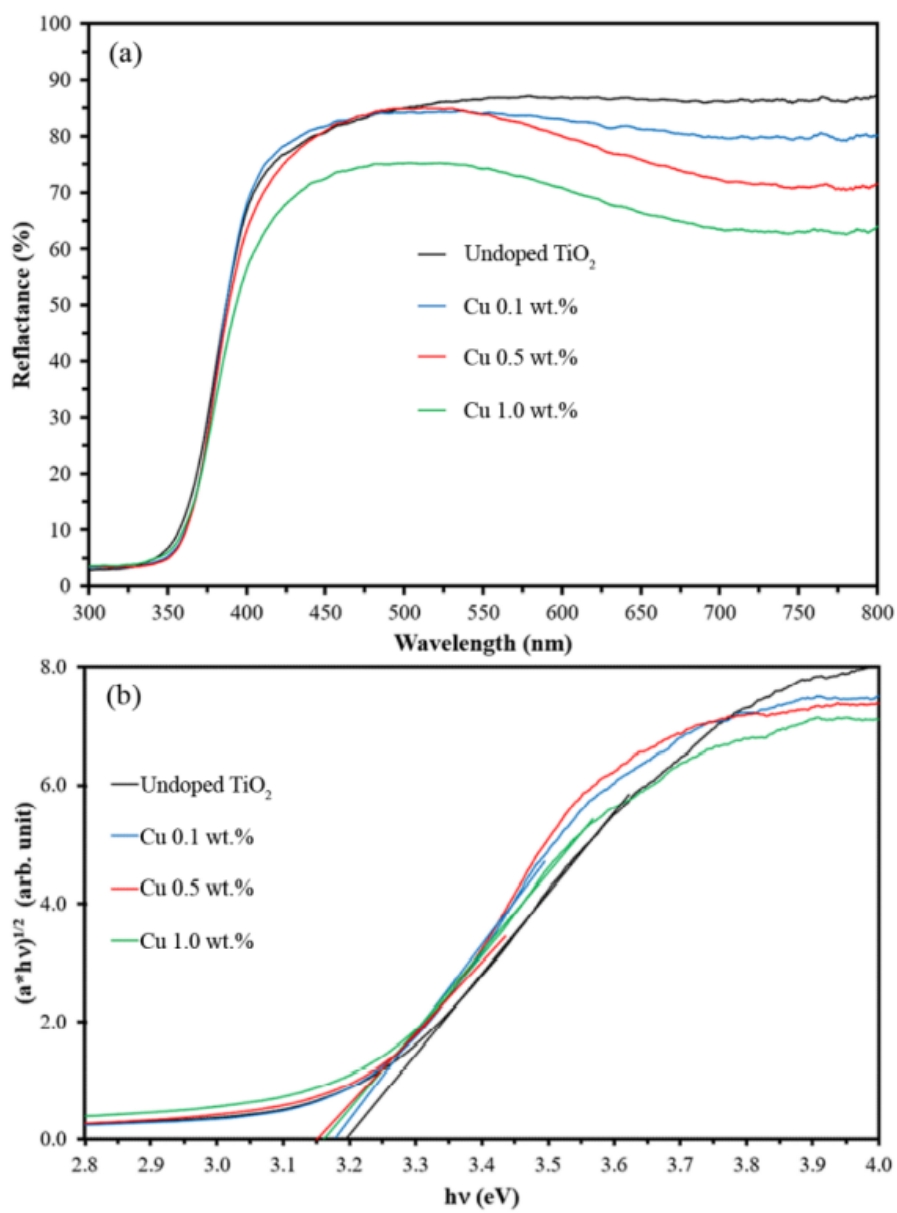


Figure 43 Reflection spectra (a) and Tauc plot (b) of Cu-doped TiO₂ nanoparticles.

Table 9 Band gap energy of undoped and Cu-doped TiO₂.

Nanoparticles	Band gap energy (eV)
TiO ₂	3.20
0.1% Cu-doped TiO ₂	3.15
0.5% Cu-doped TiO ₂	3.10
1.0% Cu-doped TiO ₂	3.12

4.2 Dyes degradation of Cu-doped TiO₂ nanoparticles

The MB degradation efficiency of undoped and Cu-doped TiO₂ nanoparticles under UV irradiation was calculated, as shown in Table 10. In addition, the data from Table 10 were plotted as shown in Figure 44. After 30 min in the dark, the Cu-doped TiO₂ nanoparticles obtained a high MB adsorption ability of 35–40%, which was more than the undoped TiO₂ nanoparticles (~20%) and P25 (~25%). The higher adsorption ability of Cu-doped TiO₂ nanoparticles is more than the undoped TiO₂ nanocomposites possibly contain Cu content as well-known excellent adsorption (Ding, Wan, Zheng, Wu, & Muhammad, 2021; Prajapati & Mondal, 2020). Even the specific surface of Cu-doped TiO₂ nanocomposites was slightly decreased compared to undoped TiO₂ nanocomposites. In addition, the surface charge of the Cu-doped TiO₂ maybe also cause an improvement in the MB adsorption ability. As reported in other research, the point of zero charges (PZC) of TiO₂ nanoparticles was approximately 6.5. Cu doping reduced the PZC value to approximately 6.0 (Nguyen Thi Thu et al., 2016). The pH value of the initial MB solution was measured to be 6.8, which was higher than the PZC of Cu-doped TiO₂ nanoparticles; the surface potential of Cu-doped TiO₂ nanoparticles represented a negative charge. MB dye is a positive charge that can be attracted by the negative surface charge of Cu-doped TiO₂ nanoparticles by the electrostatic interaction. This phenomenon caused to increase in the adsorption ability of the TiO₂ with Cu doping. Therefore, the adsorption ability of the Cu-doped TiO₂ nanoparticles is higher than the undoped TiO₂ nanoparticles, which may further improve MB degradation efficiency after irradiation.

Under UV-A irradiation, the MB degradation efficiency was sharply increased to 88% and reached 100% in 30 min for 0.1% Cu-doped TiO₂ nanoparticles. However, the increasing CuO content negatively affected the photocatalytic activity, as illustrated by the decrease in MB degradation efficiency at 30 min. The reason is that the increasing Cu content can cause high opacity and light scattering, reducing photon absorption (Yu, Hai, & Jaroniec, 2011). Therefore, this phenomenon possibly affected the generation of electrons-holes and recombination (Zhang et al., 2017). The MB degradation efficiency of Cu-doped TiO₂ nanoparticles was still higher than the undoped TiO₂ nanoparticles. Due to the Cu-doped TiO₂ nanoparticles can overcome the drawbacks of semiconductor photocatalysts, such as fast charge recombination (Wang et al., 2014). Figure 44 shows that the 0.1% Cu-doped TiO₂ nanoparticle is the best photocatalytic activity, and the MB degradation efficiency was as high as P25. In addition, the results indicated that the photocatalytic activity of TiO₂ can be improved by Cu doping.

Table 10 MB removal percentage of undoped and Cu-doped TiO₂.

Time (min)	P25		Undoped TiO ₂		0.1% Cu-doped TiO ₂		0.5% Cu-doped TiO ₂		1.0% Cu-doped TiO ₂	
	Abs.	% Removal	Abs.	% Removal	Abs.	% Removal	Abs.	% Removal	Abs.	% Removal
-30	0.6424	0.00	0.6300	0.00	0.6300	0.00	0.6300	0.00	0.6300	0.00
0	0.4759	25.92	0.4995	20.71	0.3854	38.83	0.3795	39.76	0.3858	38.76
10	0.0561	91.27	0.2971	52.84	0.0752	88.06	0.1221	80.62	0.184	70.79
20	0.0051	99.21	0.2297	63.54	0.0225	96.43	0.0703	88.84	0.1109	82.40
30	0.0091	98.58	0.1395	77.86	0.0015	99.76	0.0263	95.83	0.0493	92.17

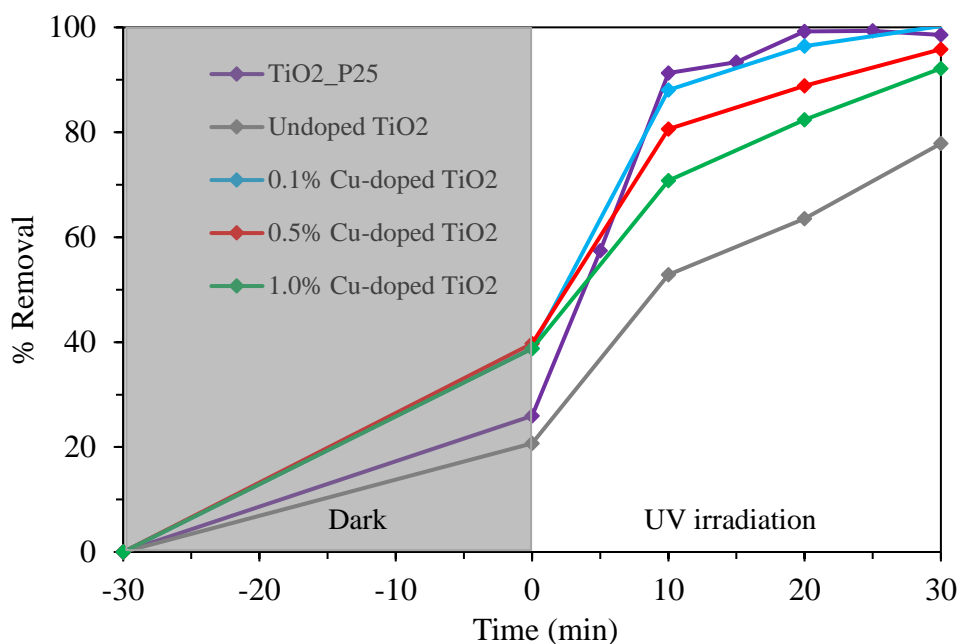


Figure 44 MB degradation of Cu-doped TiO₂ nanoparticles

4.3 Photokilling of Cu-doped TiO₂ nanoparticles

The photokilling activity of the undoped and Cu-doped TiO₂ nanoparticles was clarified against *E. coli*. Figure 45 shows the antibacterial activity of undoped and Cu-doped TiO₂ nanoparticles under UV-A irradiation. Moreover, the photo of the visible *E. coli* colony after UV-A radiation is shown in Figure 46. Figures 45 presents the visible bacteria count decreased over time after exposure to UV light within the undoped or Cu-doped TiO₂ nanoparticles, indicating that both undoped and Cu-doped TiO₂ nanoparticles showed antibacterial and bactericidal activities. While the control sample, the bacterial culture without the nanoparticles, the UV-A irradiation did not cause any bacteria death, as shown by the steady growth curve over the irradiation time. The best *E. coli* photokilling is the 0.1% Cu-doped TiO₂ nanoparticles, which showed complete killed in 180 minutes. The indicator strain was completely killed in -180 min for the 0.1 wt.% Cu-doped TiO₂ nanoparticles, whereas the undoped TiO₂ nanoparticles showed the lowest bacterial photokilling activity. In addition, the higher Cu doping of 0.5 wt.% and 1.0 wt.% Cu-doped TiO₂ nanoparticles reduced *E. coli* photokilling activity. The results suggest that the photokilling activity of TiO₂

nanoparticles can be enhanced by CuO doping. However, its photokilling activity did not follow dose-dependent. As a result, higher CuO content (more than 0.1%) negatively impacted photokilling activity performance. Moreover, the photo of the visible *E. coli* colony after UV-A radiation is clearly shown in Figure 46.

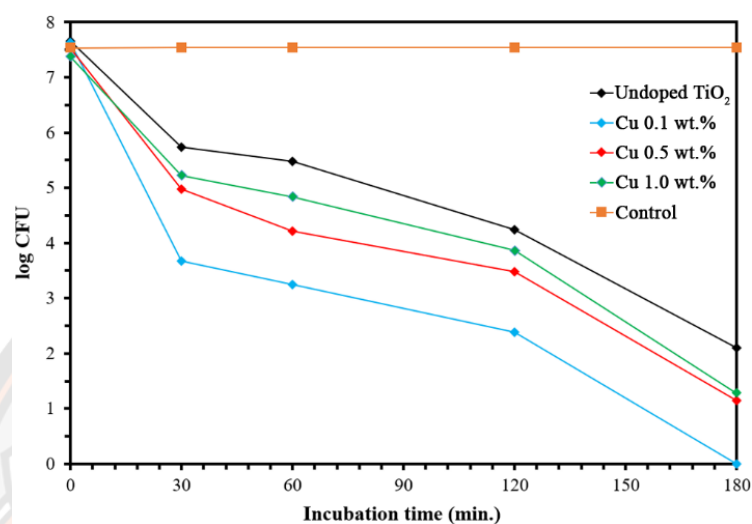


Figure 45 *E. coli* photokilling of Cu-doped TiO₂ nanoparticles.

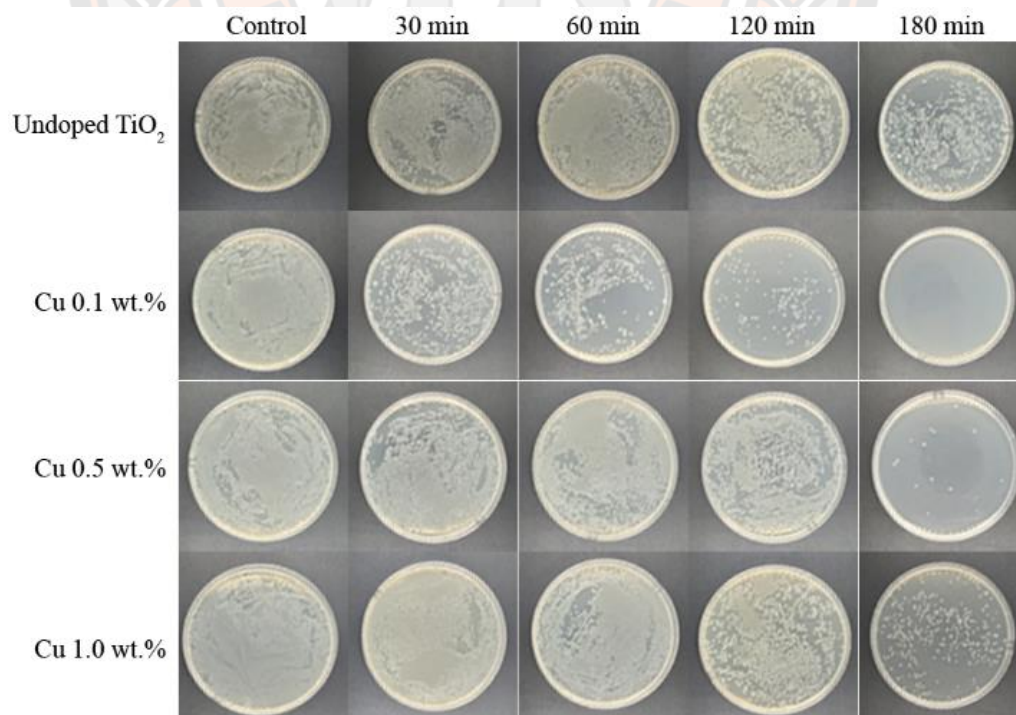


Figure 46 Photo of visible *E. coli* colony after UV-A radiation.

4.4 Characterization of Mn-doped TiO₂ nanoparticles

4.4.1 Crystalline structure

The XRD patterns of the undoped and Mn-doped TiO₂ nanoparticles, including Mn contents of 0 to 0.3%, are shown in Figure 47. In the undoped TiO₂ nanoparticles, the diffraction peaks at $2\theta = 25.3^\circ, 36.9^\circ, 37.8^\circ, 38.8^\circ, 48.1^\circ, 54.0^\circ, 55.1^\circ, 62.7^\circ$ and 68.8° were observed. These peaks correspond to the (101), (103), (004), (112), (200), (105), (211), (204) and (116) planes of anatase phase, respectively, JCPDS card: 04-0477 (Loan & Long, 2019). Although the anatase phase is a major phase, a very weak peak at $2\theta = 27.3^\circ$ was observed that corresponds to the diffraction peak from (110) plane of the rutile phase. For Mn-doped TiO₂, the characteristic diffraction peaks of the rutile phase increased with increasing Mn contents. On the other hand, for the 0.2 and 0.3% Mn-doped TiO₂, anatase is still a major phase, rutile is a minor phase, but a very weak peak of brookite at $2\theta = 31.1^\circ$ was observed that corresponding to the diffraction peak from (211) plane. The diffraction peaks for Mn or its oxide phases were not present in the XRD pattern. This result indicates the high dispersion of Mn on TiO₂ lattices.

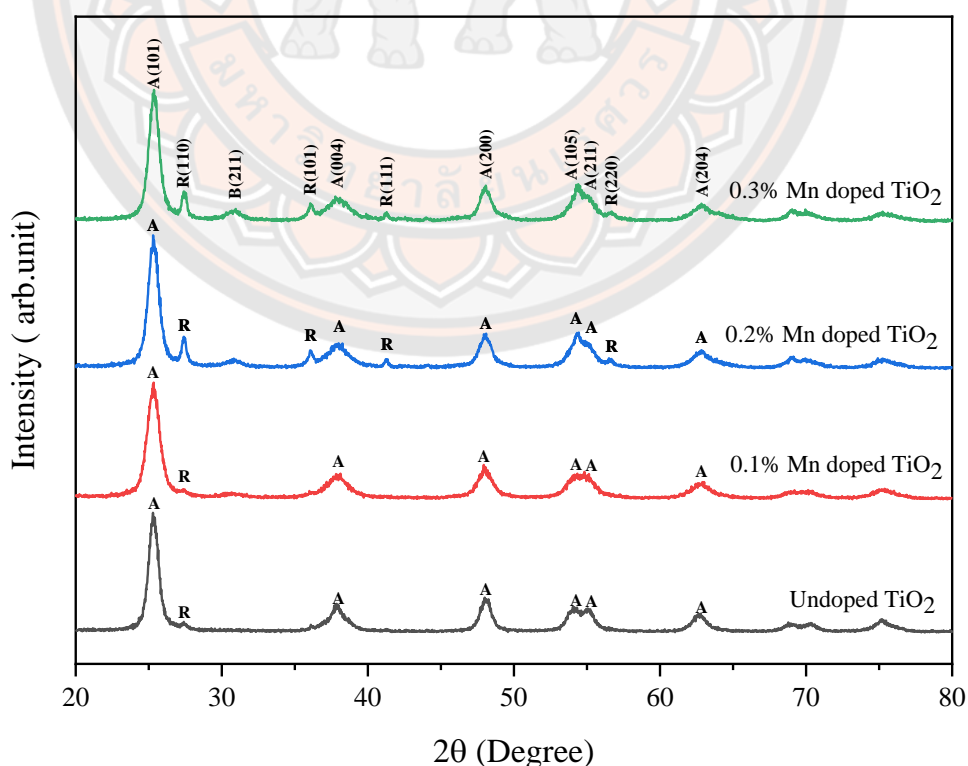


Figure 47 XRD patterns of undoped and Mn-doped TiO₂ nanoparticles.

The percentage of anatase and rutile phases of the nanoparticles was calculated by the Spurr equation shown in Table 11. The results show that rutile content in the Mn-doped TiO₂ sample increases from ~10% to ~20% when Mn content changes from 0.1% to 0.3%. As shown in Figure 48, when Mn-doped concentration is increased from 0.2 % to 0.3%, the intensity of the rutile phase is increased. These results indicate that the Mn doping content caused to change in the anatase-to-rutile transformation (ART), which is in good agreement with other research (Devi, Kumar, Murthy, & Kottam, 2009; Loan & Long, 2019).

Table 11 Percentage of anatase and rutile phases of undoped and Mn-doped TiO₂.

Nanoparticles	2θ	I _A	2θ	I _R	% Anatase	% Rutile
TiO ₂	25.3	976	27.4	91	89.5	10.5
0.1% Mn-doped TiO ₂	25.3	942	27.4	87	89.6	10.4
0.2% Mn-doped TiO ₂	25.3	1092	27.4	270	76.2	23.8
0.3% Mn-doped TiO ₂	25.4	1080	27.4	256	77.0	23.0

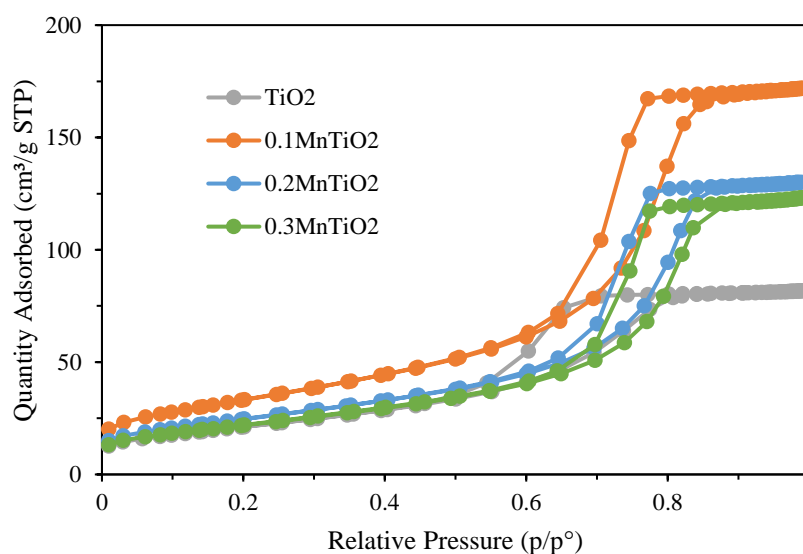
The lattice parameters of both anatase and rutile phases of the undoped and Mn-doped TiO₂ were calculated from the XRD data, as shown in Table 12. As the results, the lattice parameters data indicate that the unit cell of undoped and Mn-doped TiO₂ nanoparticles is nearly identical. The average crystallite size was determined using diffraction peak (101) based on the FWHM (Full Width at Half Maximum). It was calculated from the Debye-Scherrer formula, as shown in Table 12. The results indicate that the crystallite size of Mn-doped TiO₂ nanoparticles is decreased compared to the undoped TiO₂ nanoparticle; this result is the same as other previous works (Devi et al., 2009).

Table 12 Lattice parameters of undoped and Mn-doped TiO₂.

Nanoparticles	Anatase phase		Rutile phase		Crystal size (nm)
	a=b (Ao)	c (Ao)	a=b (Ao)	c (Ao)	
TiO ₂	3.79	9.53	4.61	2.94	9.38
0.1% Mn doped TiO ₂	3.79	9.40	4.60	2.96	7.44
0.2% Mn doped TiO ₂	3.78	9.59	4.60	2.96	8.62
0.3% Mn doped TiO ₂	3.78	9.40	4.59	2.95	8.85

4.4.2 Specific surface area

The N₂ adsorption-desorption isotherms of undoped and Mn-doped TiO₂ nanoparticles are shown in Figure 48. The results show that all the nanoparticles show the typical isotherms identified as type IV with the hysteresis loop of H1 type, suggesting that all the nanoparticles possess a mesoporous structure with a relatively narrow pore size distribution. Figure 49 represents the pore size distribution curves from the desorption branch of the isotherms by the BJH method. The results show that the pore size of the Mn-doped TiO₂ nanoparticles is larger than the undoped TiO₂ nanoparticles.

**Figure 48** N₂ adsorption-desorption isotherms of undoped and Mn-doped TiO₂.

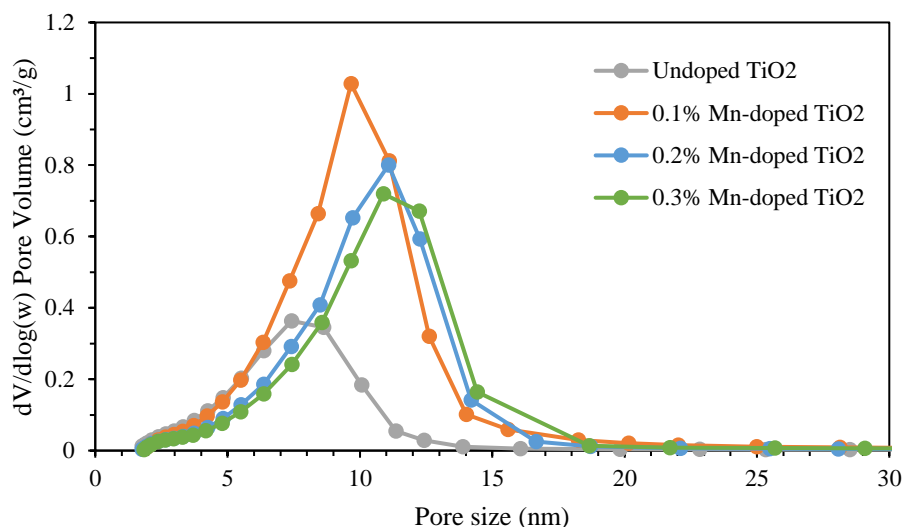


Figure 49 Pore size distribution of undoped and Mn-doped TiO₂ nanoparticles.

The BET summarizes data of the nanoparticles based on the nitrogen adsorption/desorption isotherm shown in Table 13. The pore sizes of Mn-doped TiO₂ nanoparticles increased from 7.41 to 11.08 nm when compared with the undoped TiO₂ nanoparticles. Moreover, the pore volume of the Mn-doped TiO₂ nanoparticles was also enlarged than the undoped TiO₂ nanoparticles (from 0.12 to 0.26 cm³/g). The Mn-doped TiO₂ nanoparticles contained a higher specific surface area than the undoped TiO₂ nanoparticle. The 0.1% Mn-doped is the highest specific surface area related to it, containing the smallest crystal size as the XRD result. These results agree with previous works on the pore size, pore volume and specific surface area of Mn-doped TiO₂ nanoparticles are higher than the undoped TiO₂ nanoparticles (Rashad et al., 2013; Xue et al., 2008).

Table 13 The BET summarizes data of undoped and Mn-doped TiO₂.

Nanoparticles	Specific surface area (m ² /g)	Pore size (nm)	Pore volume (cm ³ /g)
TiO ₂	77.22	7.41	0.12
0.1% Mn-doped TiO ₂	120.16	9.66	0.26
0.2% Mn-doped TiO ₂	89.36	11.08	0.20
0.3% Mn-doped TiO ₂	79.65	10.88	0.19

4.4.3 X-ray photoelectron spectroscopy (XPS)

X-ray photoelectron spectroscopy (XPS) was carried out to investigate the chemical states of atoms in the Mn-doped TiO₂ nanoparticles, as shown in Figure 50. As presented in Fig. 2a, the Ti 2p levels of all samples had two symmetrical spin-orbit doublet peaks of Ti 2p_{3/2} and Ti 2p_{1/2} located at 458.6 and 464.3, which correspond to the Ti⁴⁺ oxidation state. In addition, a single peak of the O 1s core level corresponded to the chemical bonding state of the O atoms (e.g., O²⁻, O⁻). Fig. 2c reveals Mn 2p peaks of Mn-doped TiO₂ nanoparticles, which exhibits the XPS peaks from metallic Mn at 637.7 eV (Nesbitt & Banerjee, 1998) and multivalence of Mn species: Mn²⁺ (639.8 eV), Mn³⁺ (640.6 eV), Mn⁴⁺ (642.7 eV) and Mn⁷⁺ (644.9 eV). The XPS results prove that Mn can provide multivalence ion in the TiO₂ structure. Base on theoretical prediction, Mn⁴⁺ corresponds to substitutional Mn and the host Ti atoms. On the other hand, the other peaks (Mn²⁺, Mn³⁺ and Mn⁷⁺) were compatible to satellite peaks and caused the atomic and/or lattice disorder that results to increasing rutile/anatase phase ratio.

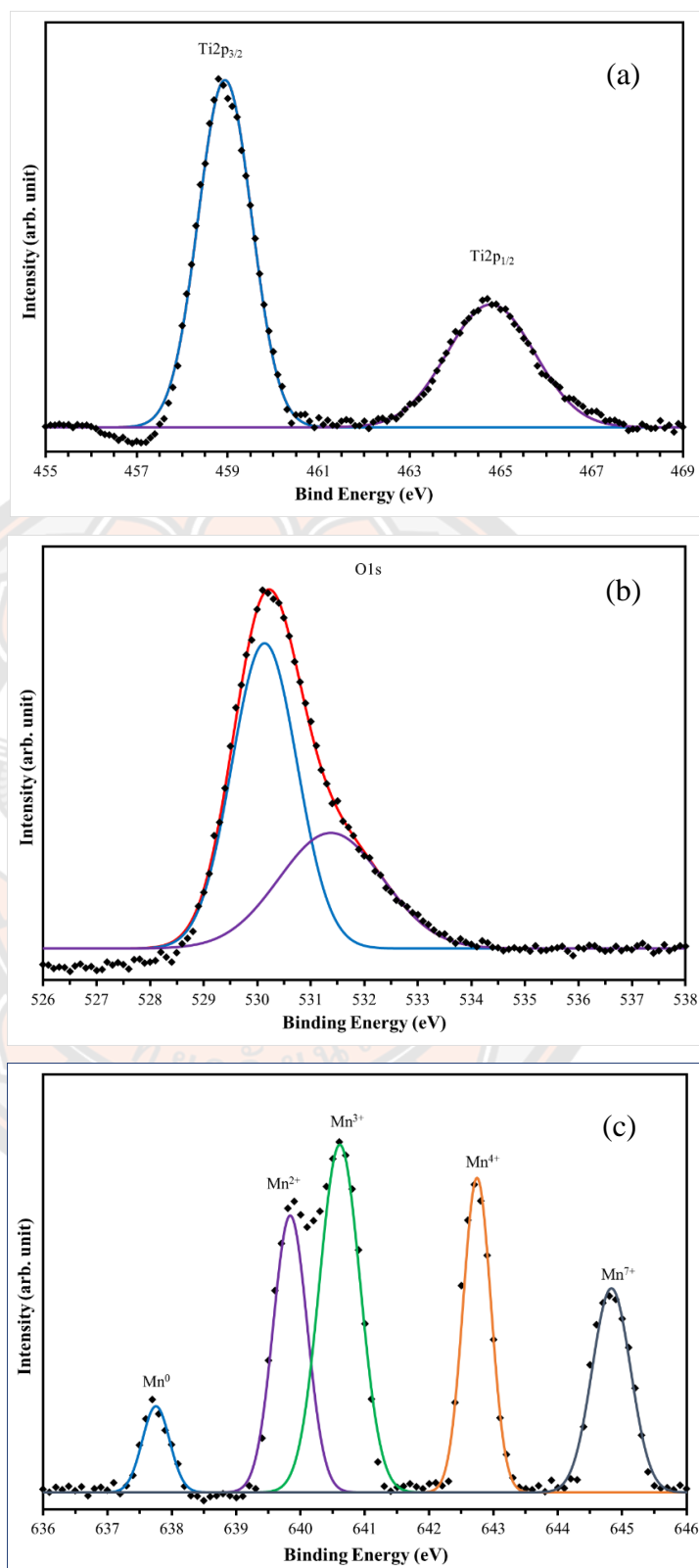


Figure 50 XPS spectra; (a) Ti 2p, (b) O 1s and (c) Mn 2p of Mn-doped TiO₂ nanoparticle.

4.4.4 Surface morphology

TEM images of the undoped and 0.2% Mn-doped TiO₂ nanoparticles are presented in Figure 51. Both TEM images show no significant difference in the morphology between the undoped and 0.2% Mn-doped TiO₂ nanoparticles. The undoped and 0.2% Mn-doped TiO₂ nanoparticles had particle sizes of approximately 10 nm, which agrees with the XRD results.

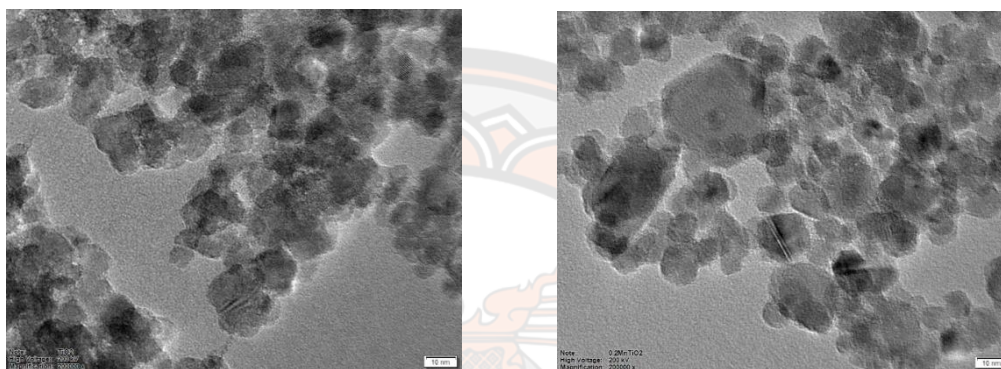
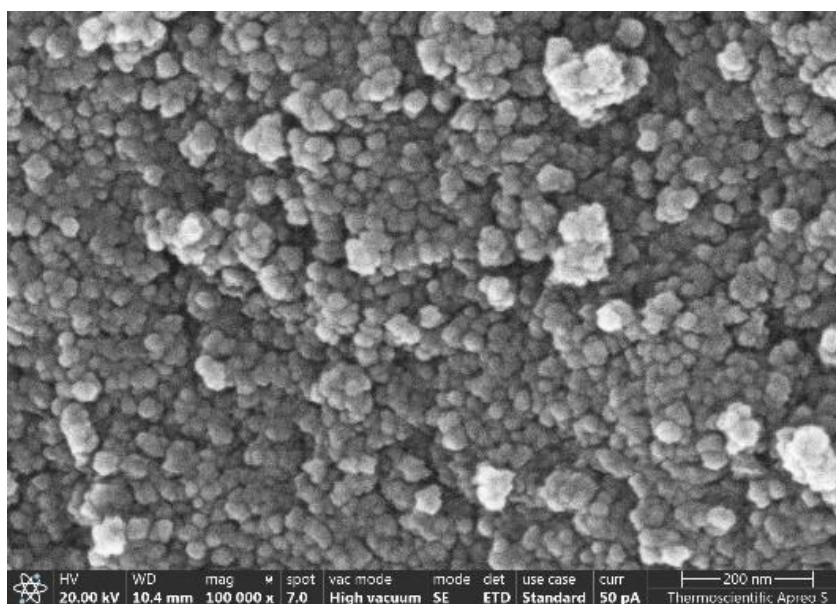
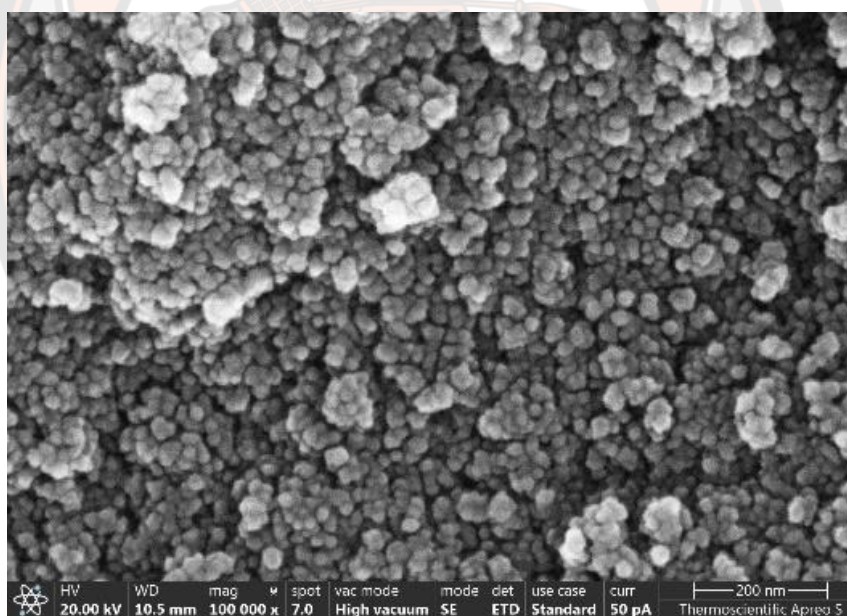


Figure 51 TEM images of (a) undoped and (b) 0.2% Mn-doped TiO₂ nanoparticles.

The scanning electron microscopy (SEM) images of undoped and 0.2% Mn-doped TiO₂ nanoparticles are shown in Figure 52. SEM images of these samples indicate no specific morphology changes due to doping. The SEM image of the nanoparticles shows that the particles have nanoscale sizes and generally seem spherical.



(a)



(b)

Figure 52 SEM images of (a) undoped TiO_2 and (b) 0.2% Mn-doped TiO_2 nanoparticles.

The elemental composition of the undoped and Mn-doped TiO_2 nanoparticles was also investigated by EDX, as shown in Figure 53. The results showed that the dopant elements Mn were found in the spectra, supporting the presence of Mn-doped TiO_2

nanoparticle. The quantitative analysis results are listed in Figure 53, describing the weight percentage of the sample's compositional elements, which indicates good compatibility with the dopant concentration used for synthesizing TiO₂ nanoparticles.

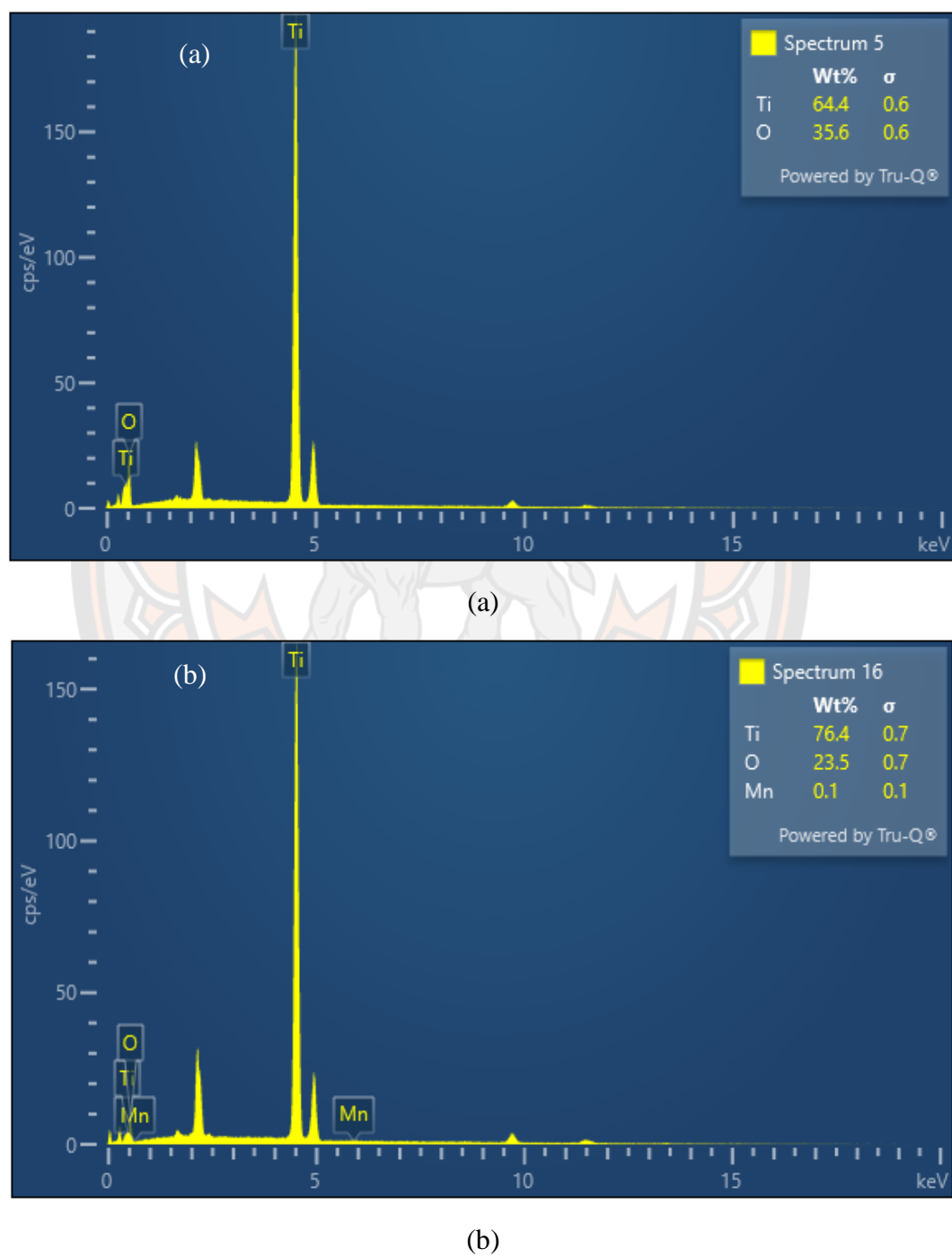
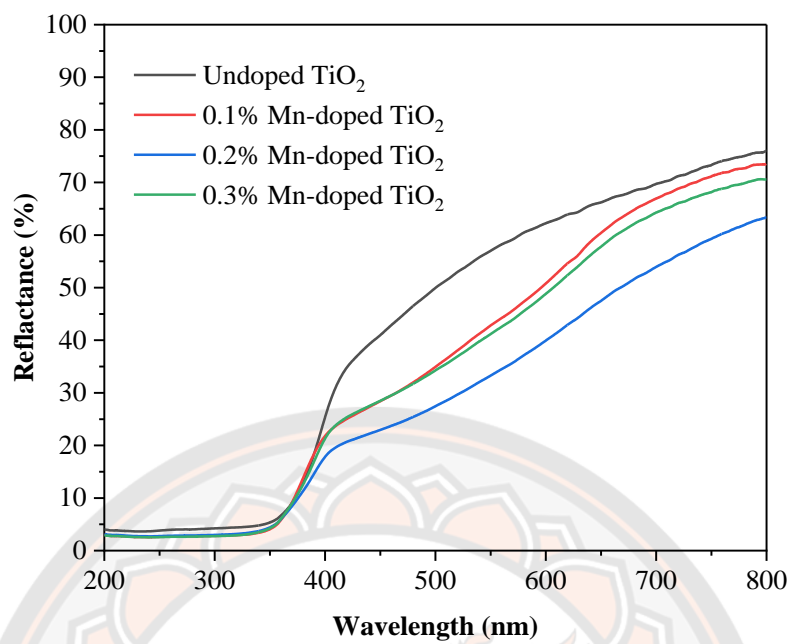


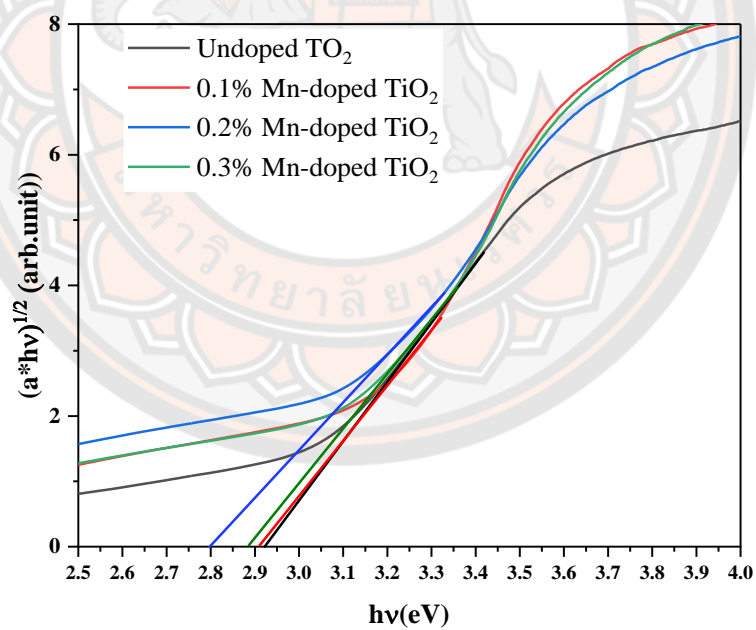
Figure 53 EDX spectra of (a) undoped TiO₂ and (b) 0.2% Mn-doped TiO₂ nanoparticles.

4.4.5 Band gap energy

The band gap energy was calculated based on Kubelka – Munk relationship using a Tauc plot from the DRS spectrum. As the Tauc plot from the DRS spectrum, $h\nu$ is plotted against $[F(R)h\nu]^{1/2}$ as x and y-axis, respectively. The tangent's intercept to the curve approximates the direct band gap energy of the nanoparticles, as shown in Figure 54. The band gap energy of the nanoparticles is summarized in Table 14. The band gap of Mn-doped TiO₂ with a difference Mn content of 0.1%, 0.2%, and 0.3% obtained is 2.91, 2.80, and 2.88, respectively. In comparison, the band gap of undoped TiO₂ is 2.92 eV. The results indicated that Mn-doped enhanced the narrow band gap. Among all the samples, the band gap of 0.2% Mn-doped TiO₂ nanoparticles is the narrowest. The band gap of all the synthesized nanoparticles falls in the visible light region, indicating that all synthesized TiO₂ nanoparticles are active under visible light irradiation. TiO₂ is well known that the anatase phase has a band gap of 3.2 eV and the rutile phase has a band gap of 3.0 eV (Serpone, 2006). The synthesized TiO₂ nanoparticles in this research had a lower band gap energy than 3.0 eV, approximately 2.92 eV, which may be caused by a combination of anatase and rutile phases. Moreover, another characteristic, particle size properties, may contribute to band gap properties (Amalraj & Pius, 2015). The band gap of TiO₂ that lower 3.0 eV (i.e., 2.9 eV, 2.95 eV, 2.98 eV) was indicated in other researches (Aini et al., 2019; Muditana et al., 2021; Yakob, Naknun, Hironmas, Dim, & Termtanun, 2021).



(a)



(b)

Figure 54 Reflection spectra (a) and Tauc plot (b) of Mn-doped TiO₂ nanoparticles.

Table 14 Band gap energy of undoped and Mn-doped TiO₂.

Nanoparticles	Band gap energy (eV)
TiO ₂	2.92
0.1% Mn-doped TiO ₂	2.91
0.2% Mn-doped TiO ₂	2.80
0.3% Mn-doped TiO ₂	2.88

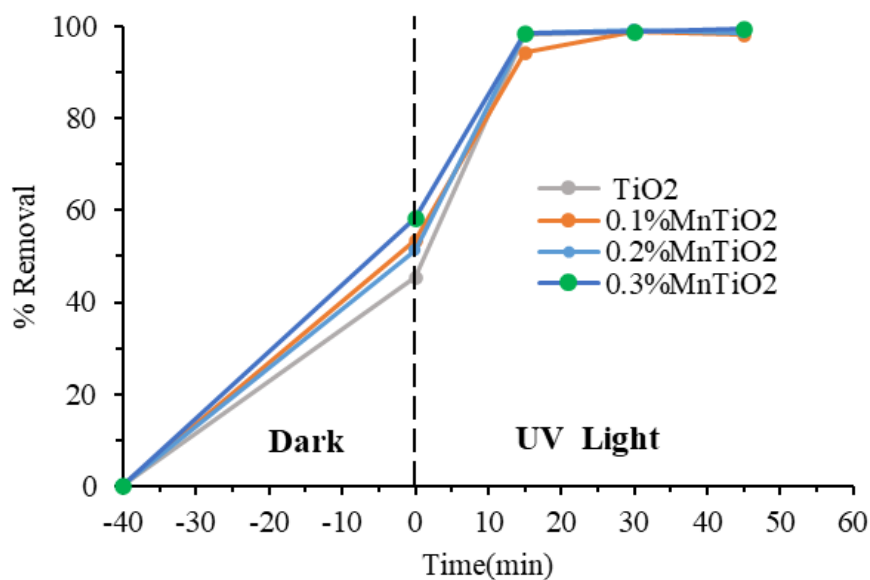
4.5 Dyes degradation of Mn-doped TiO₂ nanoparticles

The MB photocatalytic efficiency of the undoped and Mn-doped TiO₂ nanoparticles under UV light was calculated as shown in Table 15. In addition, the data from Table 15 were plotted as presented in Figure 55. The results found that after 40 minutes in the dark, the Mn-doped TiO₂ nanocomposite obtained a high MB adsorption ability of 45–58%, which is higher than the undoped TiO₂ nanoparticle (~40%). The decrease in particle size on Mn-doped TiO₂ nanoparticles results in more specific surface areas for high adsorption efficiency (Midityana et al., 2021). Moreover, the surface charge of the Mn-doped TiO₂ possibly also caused the improvement in the MB adsorption ability. As reported in the literatures, the point of zero charges (PZC) of TiO₂ nanoparticles was approximately 6.5 (Nguyen Thi Thu et al., 2016). Mn doping causes to reduce the PZC value was approximately 5.9 (Ma et al., 2019). The pH value of the initial MB solution was measured to be 6.8, which was more than the PZC of Mn-doped TiO₂; the surface potential of Mn-doped TiO₂ nanoparticles represented a negative charge. The cationic MB dye with a positive charge favoured the electrostatic interaction with the opposite charge surface of Mn-doped TiO₂ nanoparticles. This phenomenon leads to an increase in adsorption ability in the dark.

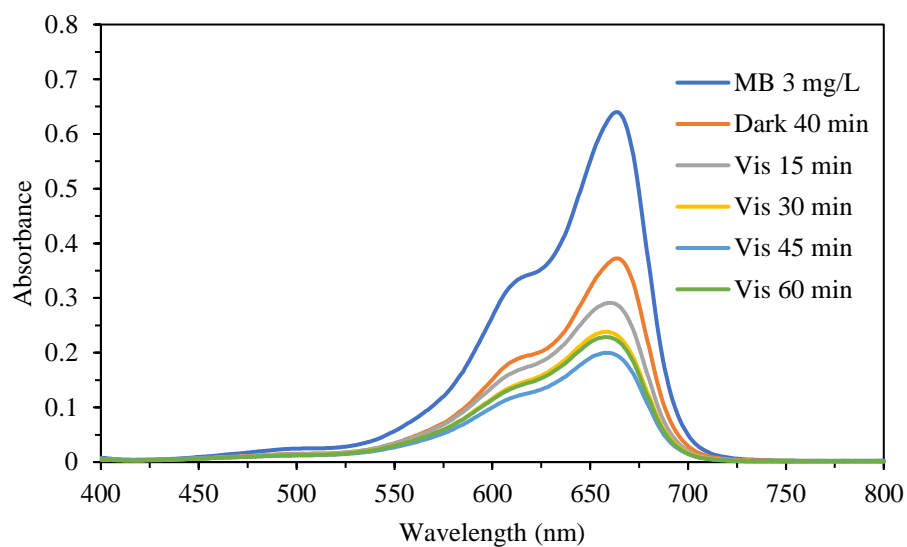
Under UV irradiation, the results clearly indicated that the MB degradation efficiency was sharply increased by nearly 100% in 15 min for both undoped and Mn-doped TiO₂ nanoparticles.

Table 15 MB photodegradation of Mn-doped TiO₂ under UV-A irradiation.

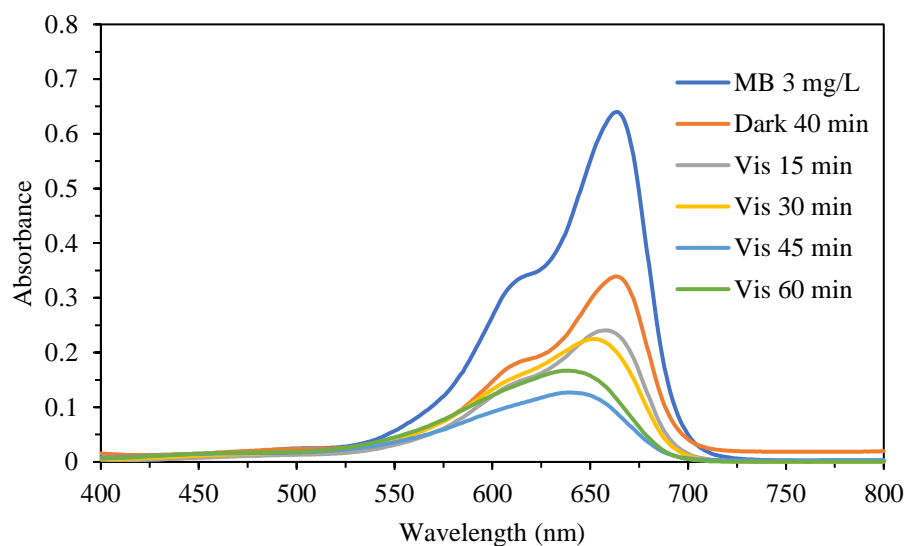
Time (min)	Undoped TiO ₂		0.1% Mn-doped TiO ₂		0.2% Mn-doped TiO ₂		0.3% Mn-doped TiO ₂	
	Abs.	% Removal	Abs.	% Removal	Abs.	% Removal	Abs.	% Removal
-40	0.6410	0.00	0.6410	0.00	0.6410	0.00	0.6410	0.00
0	0.3497	45.36	0.2976	53.50	0.3118	51.28	0.2672	58.32
15	0.0099	98.46	0.0359	94.40	0.0081	98.74	0.0091	98.58
30	0.0067	98.95	0.0074	98.85	0.0057	99.11	0.0073	98.86
45	0.0072	98.88	0.0111	98.27	0.0080	98.75	0.0029	99.55

**Figure 55** MB degradation of Mn-doped TiO₂ under UV-A irradiation.

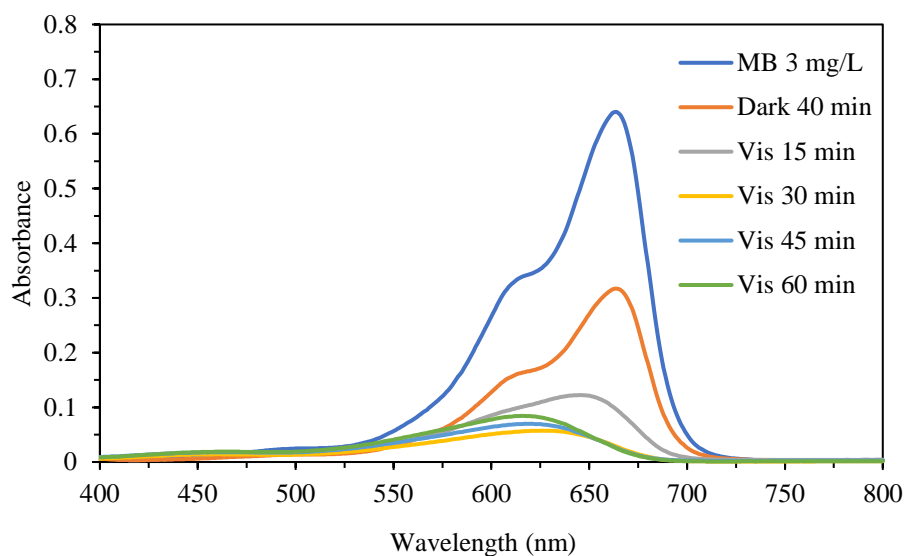
The photocatalytic activity of undoped and Mn-doped TiO₂ nanoparticles was performed by MB photodegradation under visible irradiation using the UV-Vis spectrophotometer. The absorbance spectrum of MB during degradation under visible irradiation by undoped and Mn-doped TiO₂ nanoparticles was presented in Figure 56.



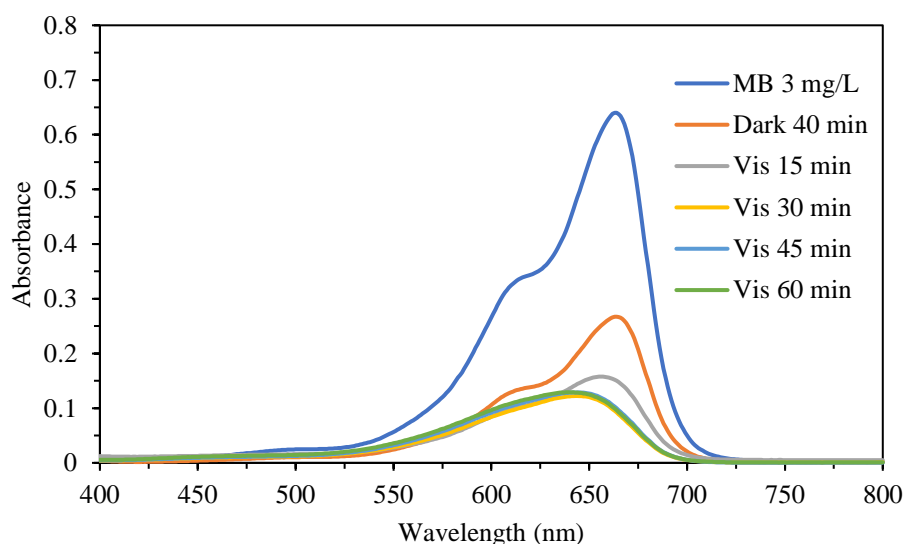
(a)



(b)



(c)



(d)

Figure 56 Absorbance spectrum of MB during degradation under visible irradiation by (a) undoped TiO₂, (b) 0.1% Mn-doped TiO₂, (c) 0.2% Mn-doped TiO₂ and (d) 0.3% Mn-doped TiO₂.

According to the absorbance spectrum, the maximum absorbance at 664 nm was calculated for removal percentage, as shown in Table 16. The photodegradation data as removal percentage was also plotted and presented in Figure 57. As the results, it is essential to note that the undoped TiO₂ nanoparticles achieved only ~40% of MB

removal in the dark adsorption, whereas the Mn-doped TiO₂ nanoparticles achieved ~47-58% of MB removal. After dark adsorption, these results indicated that the Mn-doped TiO₂ nanoparticles exhibited higher photocatalytic degradation under visible light. The best MB degradation efficiency of 96% was observed in 0.2% Mn-doped TiO₂, followed by 0.3% Mn-doped TiO₂, 0.1% Mn-doped TiO₂, and undoped TiO₂ nanoparticles, respectively. Moreover, the increase in photocatalytic efficiency with Mn doping is due to the decrease in particle size on Mn-doped TiO₂ nanoparticles, which results in higher specific surface areas for catalytic reactions. It is found that the increase in photocatalytic efficiency with Mn doping is due to Mn doping into Ti lattice sites giving narrow bands, which can help generate electrons and holes under irradiation of light of various wavelengths. For Mn doping concentrations of more than 0.2%, the photocatalytic efficiency is decreased due to more crystal defects, which may serve as recombination electrons and holes (Chandra Sekhar et al., 2018).

Table 16 Photodegradation of MB under visible light by undoped and Mn-doped TiO₂.

Time (min)	Undoped TiO ₂		0.1% Mn-doped TiO ₂		0.2% Mn-doped TiO ₂		0.3% Mn-doped TiO ₂	
	Abs.	% Removal	Abs.	% Removal	Abs.	% Removal	Abs.	% Removal
-40	0.6400	0.00	0.6400	0.00	0.6400	0.00	0.6400	0.00
0	0.3724	41.81	0.3390	47.03	0.3170	50.47	0.2672	58.32
15	0.2870	55.16	0.2323	63.70	0.0956	85.06	0.1499	76.58
30	0.2310	63.91	0.1983	69.02	0.0281	95.61	0.0919	85.64
45	0.1944	69.63	0.0878	86.28	0.0256	96.00	0.0995	84.45
60	0.2218	65.34	0.1128	82.38	0.0248	96.13	0.0960	85.00

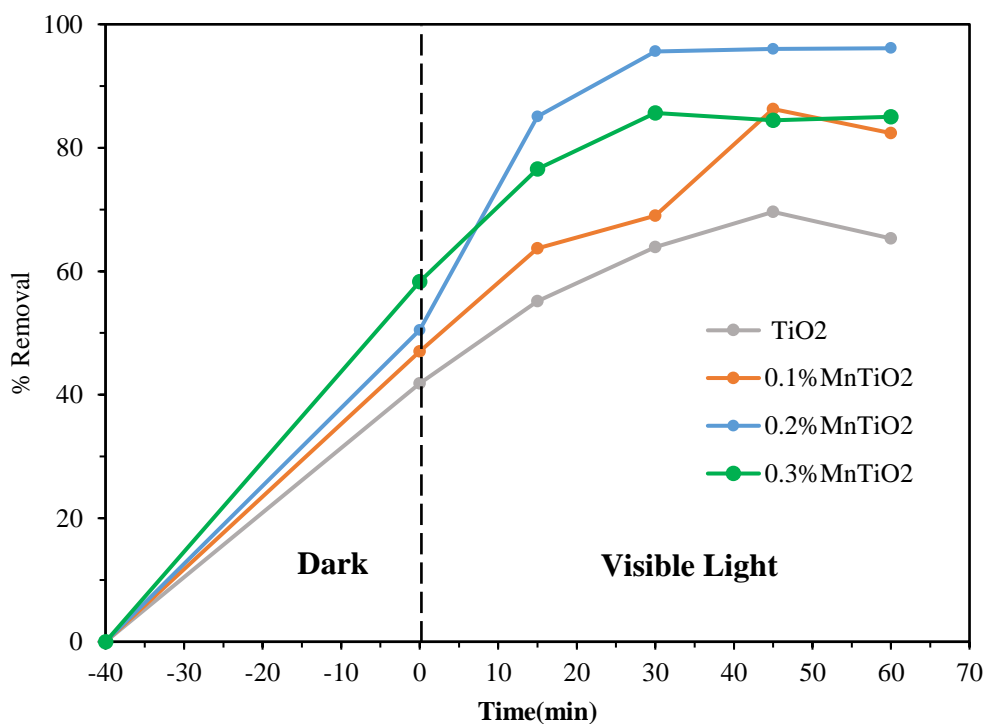


Figure 57 MB degradation of Mn-doped TiO₂ under visible irradiation.

4.6 Drugs degradation of Mn-doped TiO₂ nanoparticles

The photocatalytic activity of undoped and Mn-doped TiO₂ nanoparticles on salbutamol was examined. The various concentrations of salbutamol ranged from 0.1 to 20 mg/L to create the calibration curve. The absorbance spectrum of salbutamol with different concentrations was measured and suggested in Figure 58.

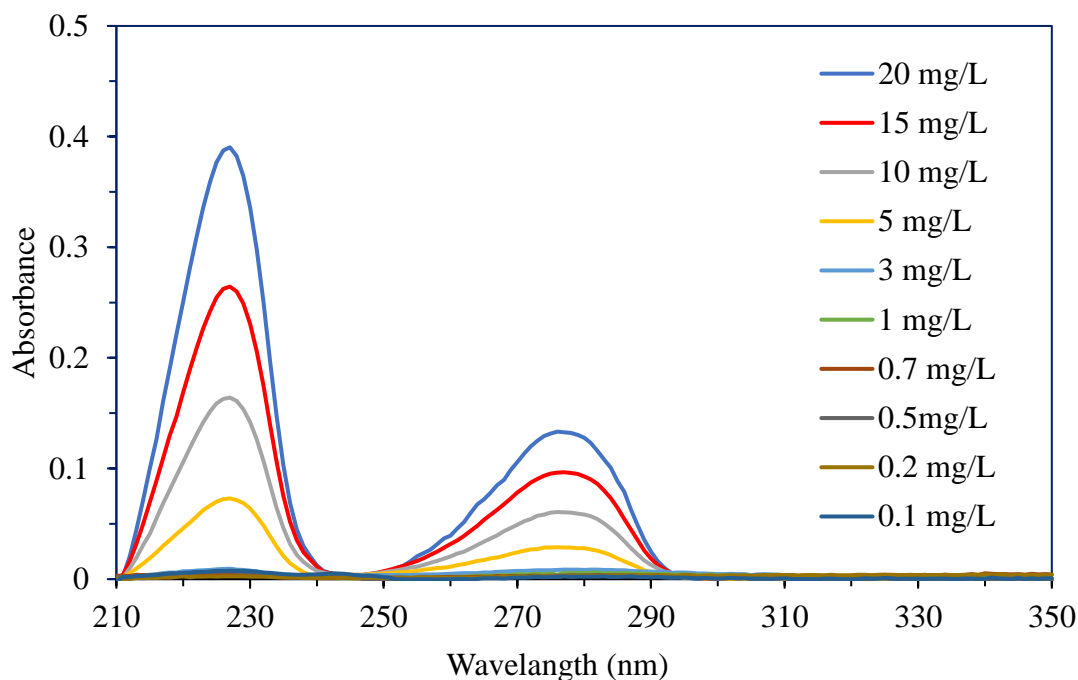
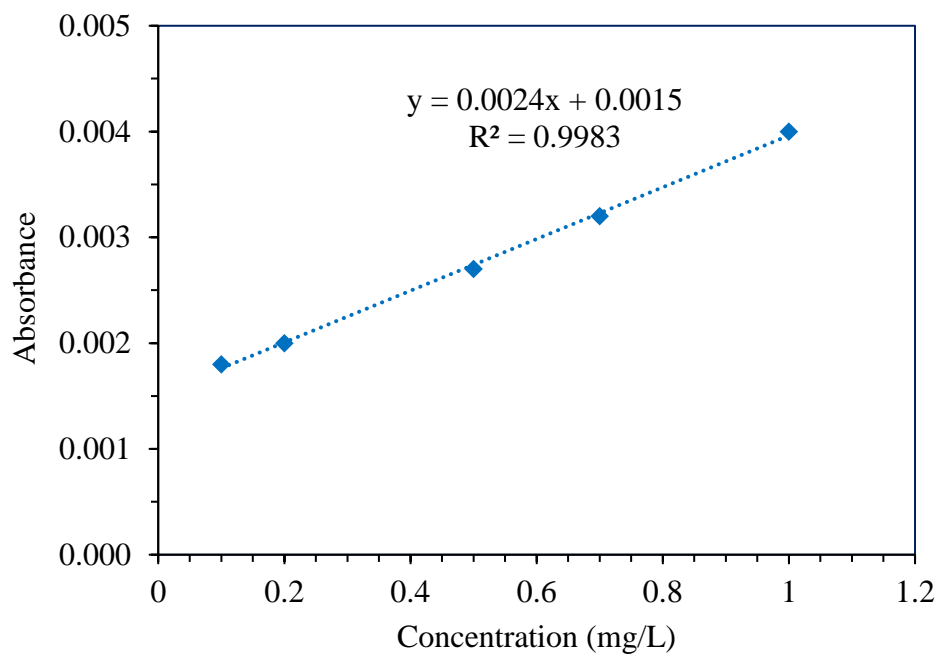


Figure 58 Absorbance spectrum after subtracting baseline of salbutamol with different concentrations.

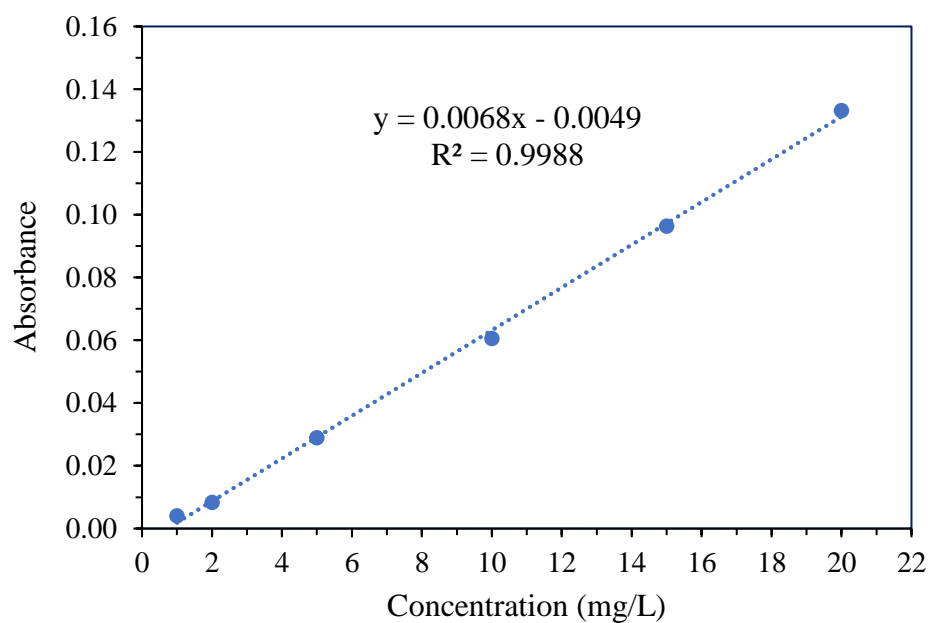
The obtained results show two absorption peaks at the wavelength around 224 and 276 nm. However, the absorbance value at the wavelength 276 nm was used to study, referring to the other research (Deepak et al., 2013 and Dodson et al., 2011) due to the minimum detection limit (200 nm) of UV-Vis spectroscopy. The absorbance value at the wavelength 276 nm is shown in Table 17. Moreover, the calibration curve of salbutamol was created from a chart of absorbance value against the concentration. It was separated into two range concentrations, 0.1-1 and 1-20 mg/L, as shown in Figure 59. According to the calibration curve of salbutamol, the straight line with high regression coefficient value (R^2) was obtained from the separation of the concentration 0.1-1 and 1- 20 mg/L.

Table 17 Absorbance value of salbutamol in different concentrations at the wavelength of 276 nm.

SAL Concentration (mg/L)	Absorbance
0.1	0.0018
0.2	0.0020
0.5	0.0027
0.7	0.0032
1	0.0040
2	0.0083
5	0.0289
10	0.0606
15	0.0964
20	0.1332



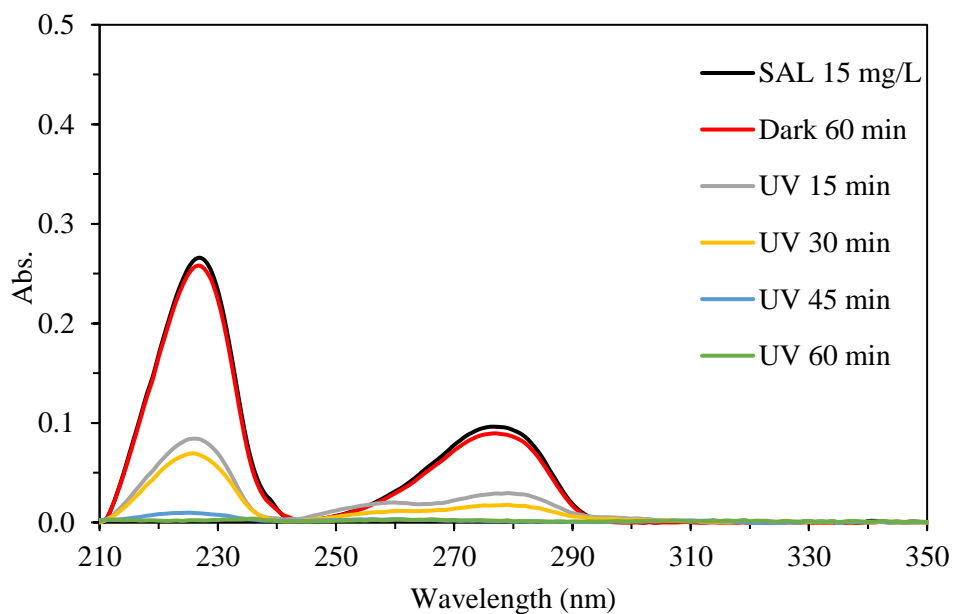
(a)



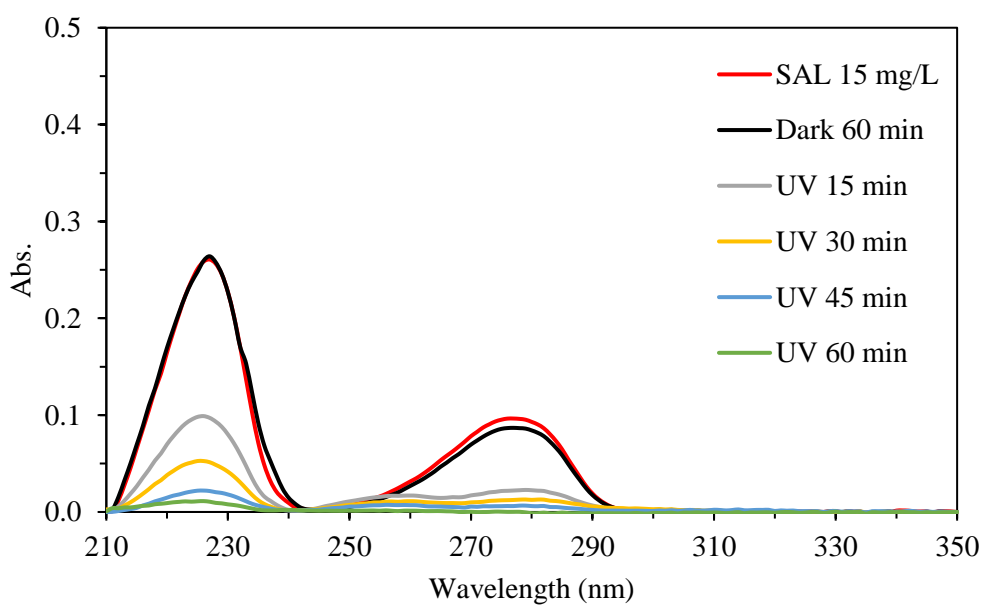
(b)

Figure 59 Calibration curve to determine the concentration of salbutamol (a) 0.1-1 and (b) 1-20 mg/L.

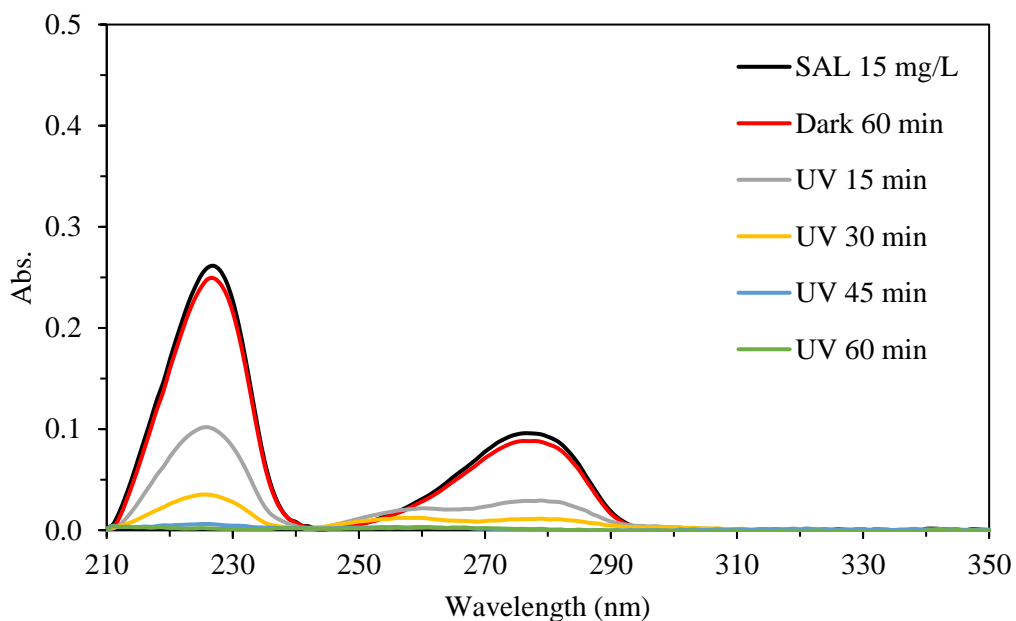
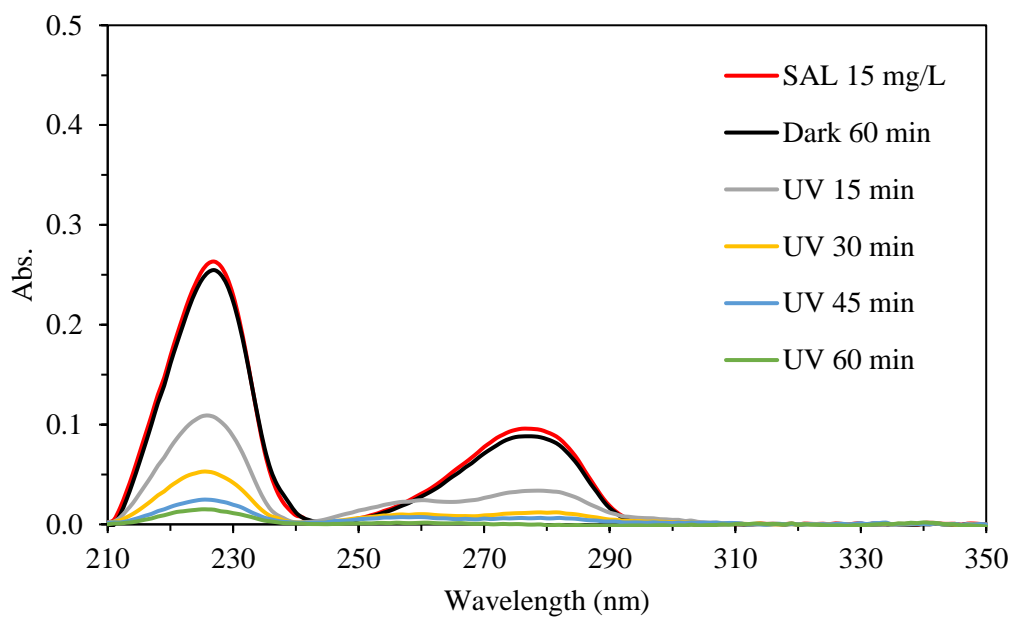
The absorbance spectrum of salbutamol was illustrated during degradation under UV-A irradiation by undoped and Mn-doped TiO_2 nanoparticles, as shown in Figure 60.



(a)



(b)



(d)

Figure 60 Absorbance spectrum after subtracting baseline of SAL during degradation under UV-A irradiation by (a) undoped TiO₂, (b) 0.1% Mn-doped TiO₂, (c) 0.2% Mn-doped TiO₂ and (d) 0.3% Mn-doped TiO₂.

According to the absorbance spectrum, the absorbance value at a wavelength of 276 nm was calculated for salbutamol concentration, referring to the calibration curve. The removal percentage was also calculated, as indicated in Table 18.

The results indicated no difference in the photocatalytic degradation of undoped and Mn-doped TiO₂ nanoparticles. Both undoped and Mn-doped showed higher excellent salbutamol photodegradation, nearly 100% degradation. The photodegradation activity was also plotted, as shown in Figure 61.



Table 18 SAL photodegradation of Mn-doped TiO₂ under UV-A irradiation.

Time (min)	Undoped TiO ₂			0.1% Mn-doped TiO ₂			0.2% Mn-doped TiO ₂			0.3% Mn-doped TiO ₂		
	Abs.	Concentration (mg/L)	% Removal	Abs.	Concentration (mg/L)	% Removal	Abs.	Concentration (mg/L)	% Removal	Abs.	Concentration (mg/L)	% Removal
-60	0.0961	14.85	0.00	0.0964	14.90	0.00	0.0958	14.81	0.00	0.0958	14.81	0.00
0	0.0890	13.81	7.00	0.0866	13.46	9.66	0.0881	13.68	7.66	0.0882	13.69	7.54
15	0.0284	4.89	67.07	0.0218	3.93	73.61	0.0332	5.61	62.15	0.0288	4.96	66.50
30	0.0169	3.21	78.41	0.0122	2.51	83.16	0.0113	2.38	83.90	0.0110	2.33	84.26
45	0.0025	0.43	97.11	0.0034	0.77	94.83	0.0038	0.95	93.56	0.0030	0.63	95.78
60	0.0019	0.17	98.85	0.0025	0.42	97.18	0.0026	0.46	96.88	0.0029	0.58	96.12

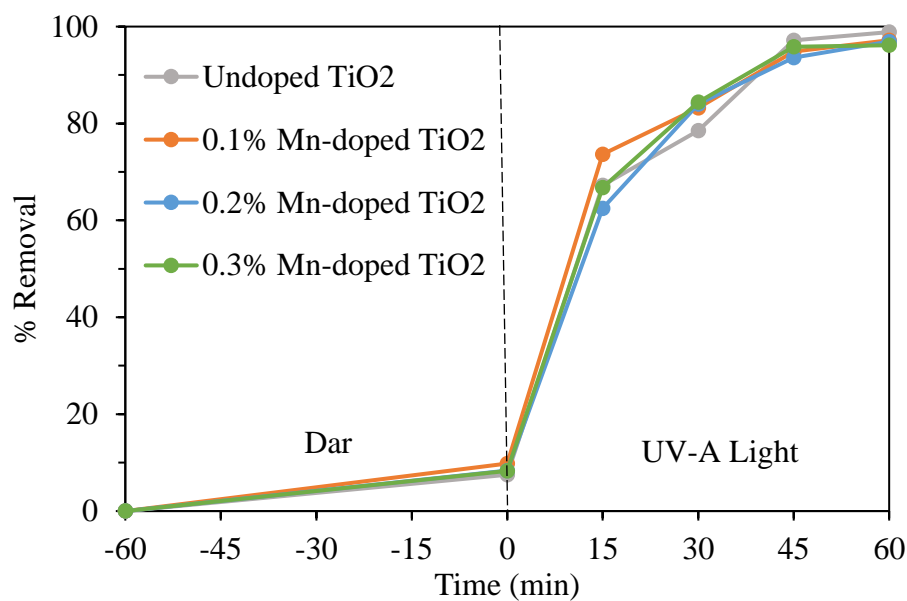
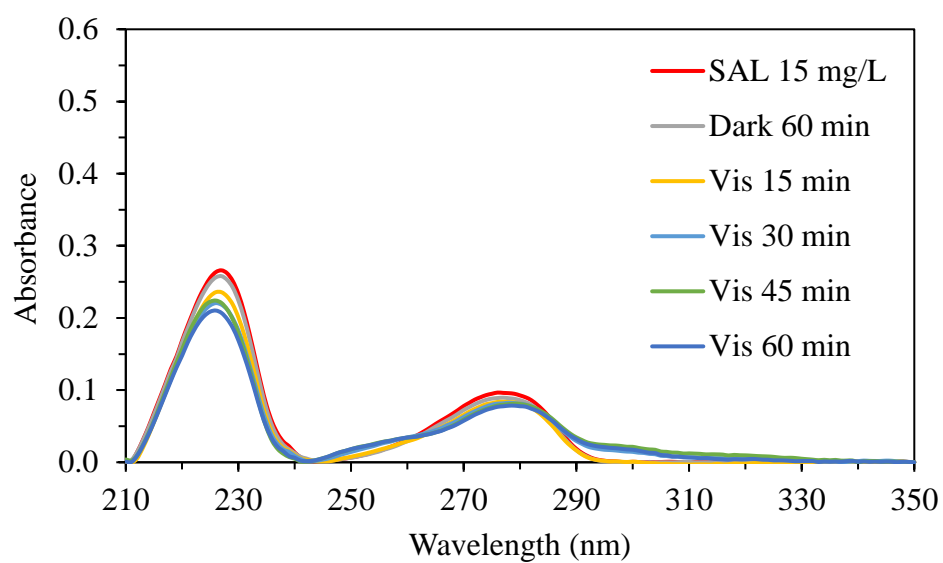
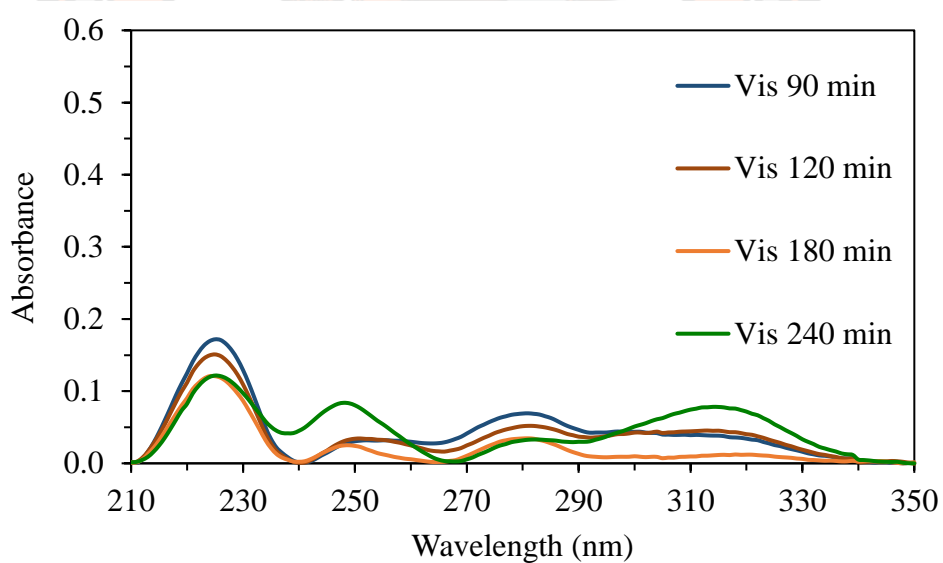


Figure 61 SAL degradation of the undoped and Mn-doped TiO₂ under UV-A irradiation.

Salbutamol photodegradation under visible irradiation was measured using the UV-Vis spectrometer. After subtracting the baseline, the absorbance spectrum of salbutamol was illustrated during degradation under visible irradiation by undoped and Mn-doped TiO₂ nanoparticles, as shown in Figure 62-65.

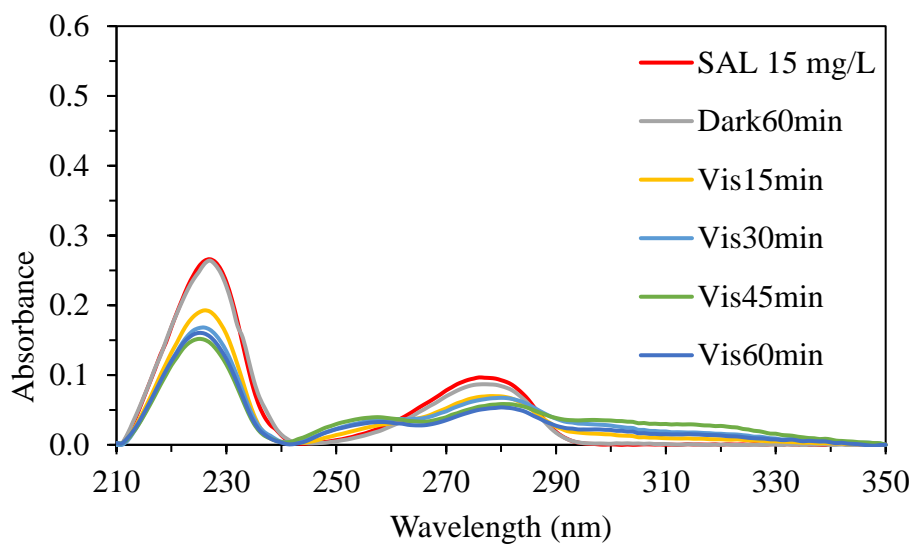


(a)

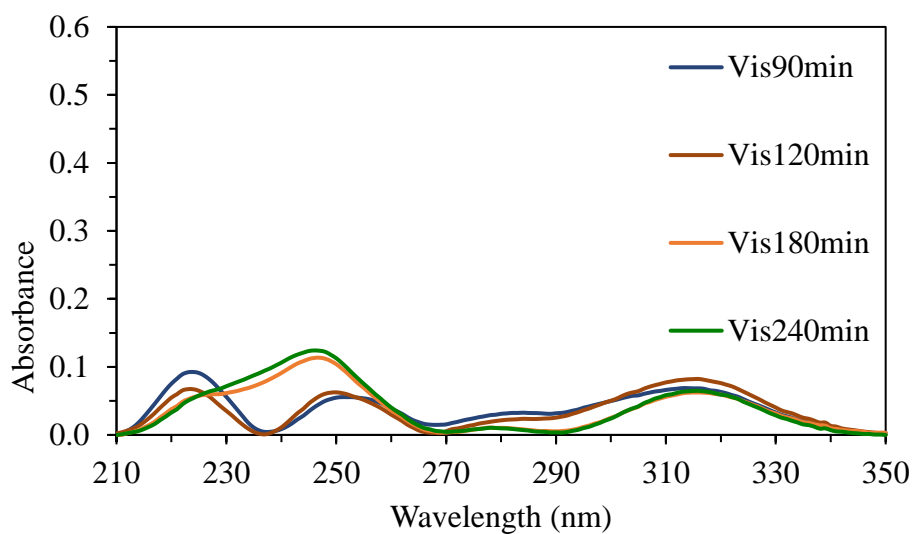


(b)

Figure 62 Absorbance spectrum after subtracting baseline of SAL during degradation by undoped TiO₂ nanoparticles under visible irradiation (a) 0-60 min and (b) 90-240 min.

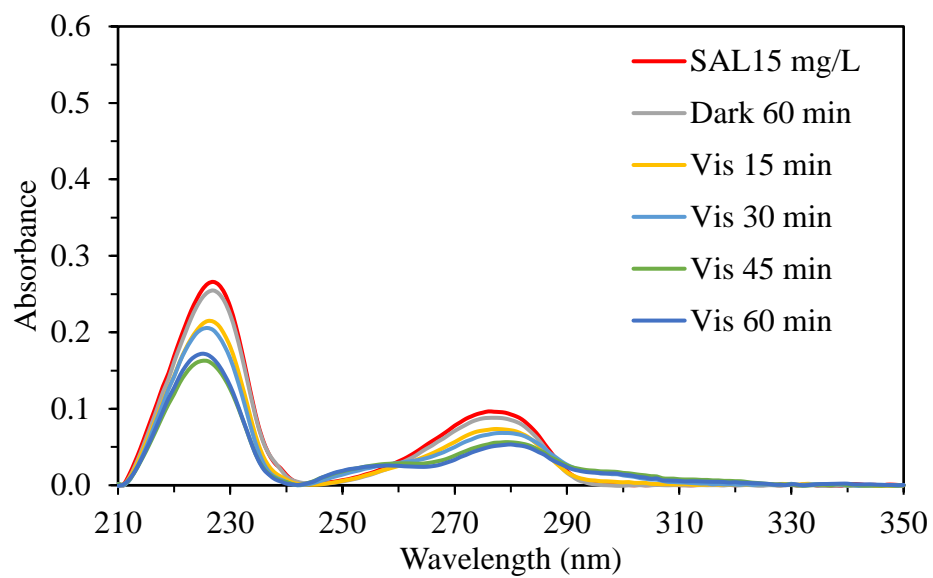


(a)

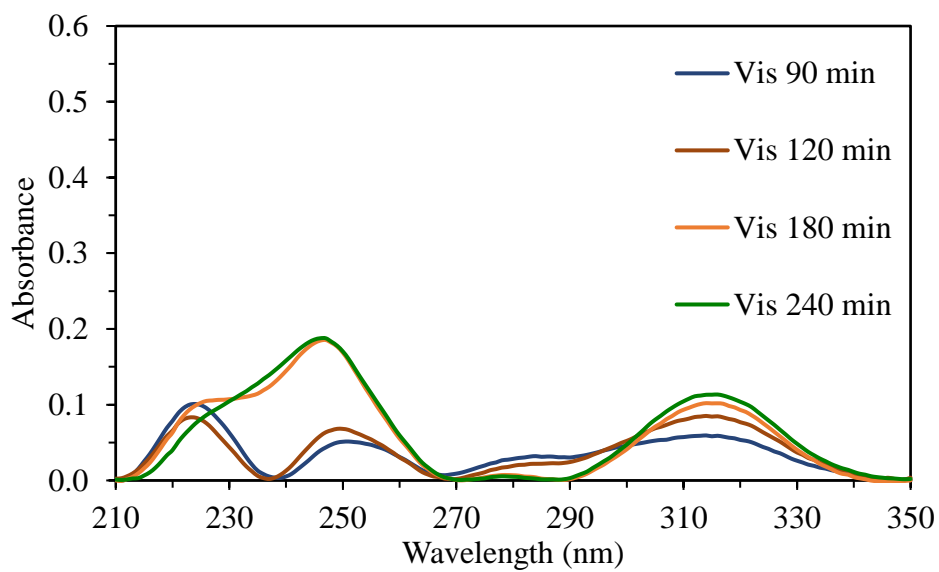


(b)

Figure 63 Absorbance spectrum after subtracting baseline of SAL during degradation by 0.1% Mn-doped TiO₂ nanoparticles under visible irradiation (a) 0-60 min and (b) 90-240 min.

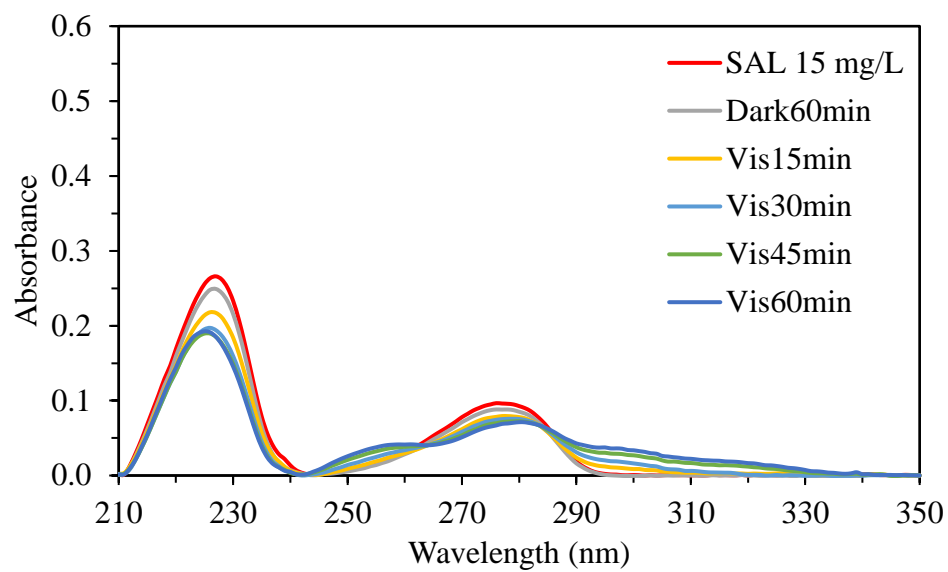


(a)

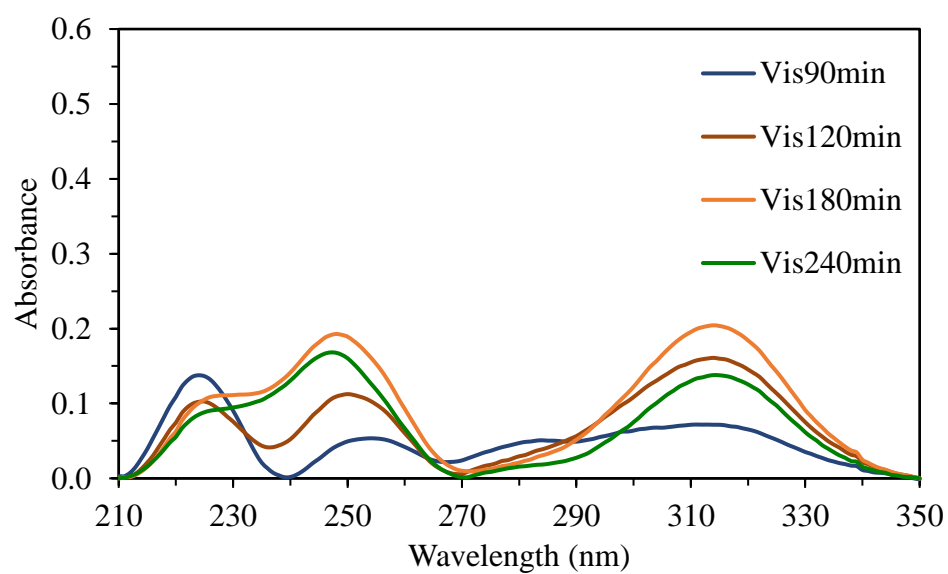


(b)

Figure 64 Absorbance spectrum after subtracting baseline of SAL during degradation by 0.2% Mn-doped TiO₂ nanoparticles under visible irradiation (a) 0-60 min and (b) 90-240 min.



(a)



(b)

Figure 65 Absorbance spectrum after subtracting baseline of SAL during degradation by 0.3% Mn-doped TiO₂ nanoparticles under visible irradiation (a) 0-60 min and (b) 90-240 min.

The results from the UV-Vis spectrometer were calculated in concentration and removal percentage using the maximum absorbance at a wavelength of 276, as shown in Table 19. The photodegradation efficiency was also plotted, as presented in Figure 66. From the results in the dark adsorption, only approximately 7 - 10% of salbutamol removal on undoped and Mn-doped TiO₂ nanoparticles. After dark adsorption, these results indicated that the undoped and Mn-doped TiO₂ nanoparticles exhibited higher photocatalytic degradation under visible light. It can be noted that the photodegradation efficiency of Mn-doped TiO₂ nanoparticles is higher than the undoped TiO₂ nanoparticles. The highest SAL degradation efficiency of 95% was observed in 0.2%Mn-doped TiO₂ within 3 hours of irradiation, followed by 0.1%Mn-doped TiO₂, 0.3%Mn-doped TiO₂, and undoped TiO₂ nanoparticles, respectively.

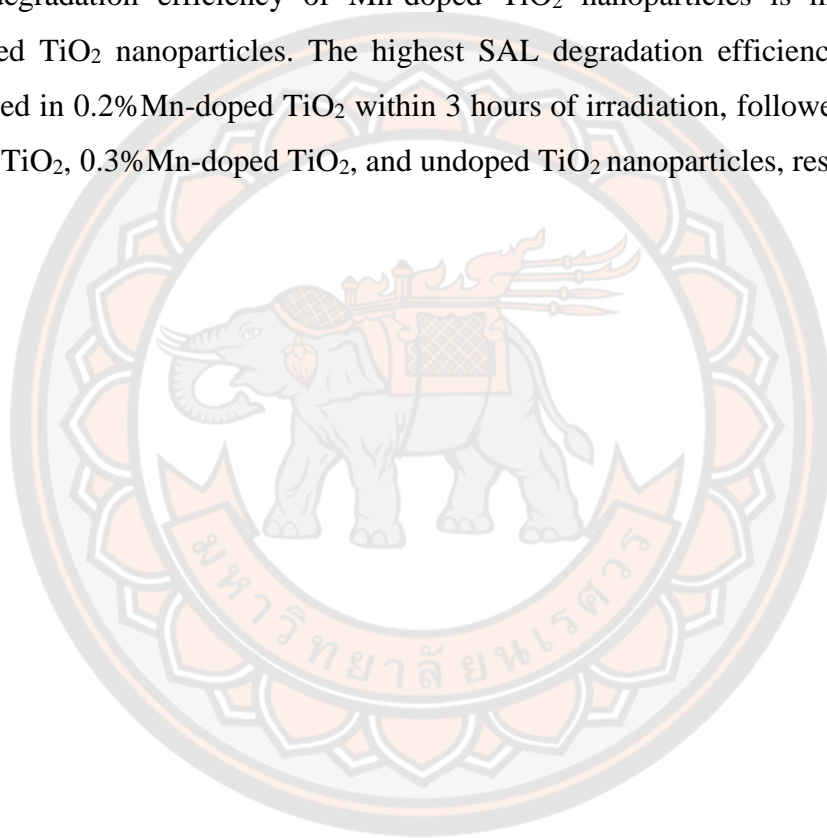


Table 19 SAL photodegradation of Mn-doped TiO₂ under visible irradiation.

Time (min)	Undoped TiO ₂			0.1% Mn-doped TiO ₂			0.2% Mn-doped TiO ₂			0.3% Mn-doped TiO ₂		
	Abs.	Concentration (mg/L)	% Removal	Abs.	Concentration (mg/L)	% Removal	Abs.	Concentration (mg/L)	% Removal	Abs.	Concentration (mg/L)	% Removal
-60	0.0966	14.93	0.00	0.0966	14.93	0.00	0.0966	14.93	0.00	0.0966	14.93	0.00
0	0.0890	13.81	7.47	0.0866	13.46	9.84	0.0881	13.68	8.37	0.0882	13.69	8.28
15	0.0836	13.02	12.79	0.0686	10.81	27.57	0.0726	11.39	23.69	0.0783	12.24	18.01
30	0.0812	12.66	15.18	0.0641	10.15	32.03	0.0663	10.47	29.86	0.0744	11.66	21.88
45	0.0788	12.30	17.59	0.0547	8.77	41.25	0.0536	8.60	42.36	0.0699	11.00	26.30
60	0.0769	12.03	19.41	0.0502	8.11	45.69	0.0497	8.04	46.17	0.0669	10.56	29.26
90	0.0633	10.03	32.84	0.0261	4.56	69.44	0.0223	4.00	73.20	0.0394	6.51	56.39
120	0.0446	7.28	51.26	0.0166	3.16	78.81	0.0136	2.72	81.79	0.0202	3.70	75.23
180	0.0303	5.17	65.35	0.0088	2.02	86.49	0.0055	1.53	89.77	0.0142	2.81	81.16
240	0.0248	4.36	70.77	0.0087	2.01	86.56	0.0043	1.35	90.97	0.0103	2.23	85.03

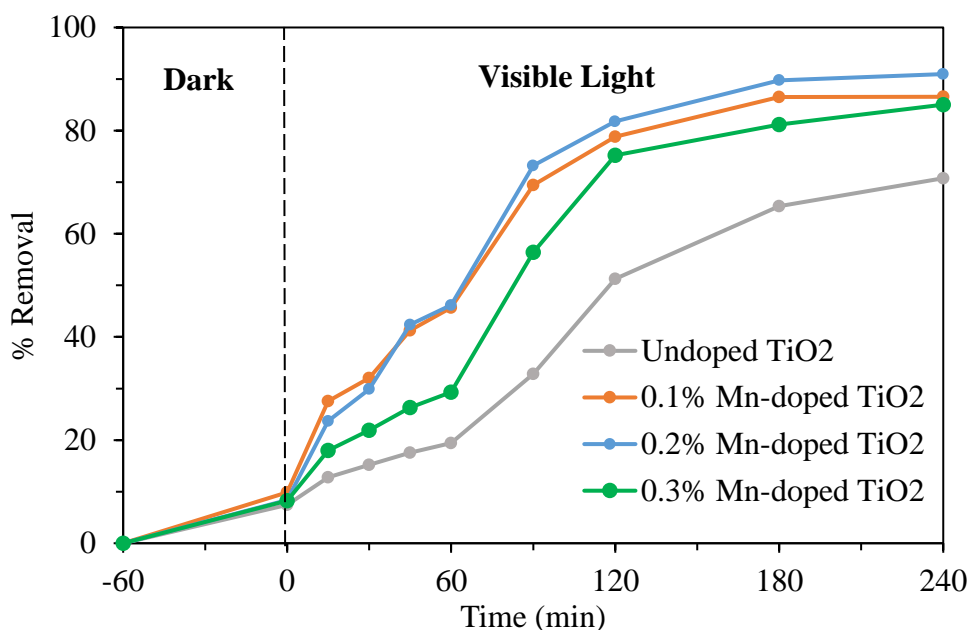


Figure 66 SAL degradation of the undoped and Mn-doped TiO₂ under visible irradiation.

LC-MS was used to evaluate the photocatalytic SAL degradation of 0.2% Mn-doped TiO₂ nanoparticles. The results from LC-MS shown as Figure 67. The obtained results from the LC-MS were calculated in removal percentage, as shown in Table 20. From the results in the dark adsorption, only ~8% of salbutamol removal. Under visible irradiation, the 0.2% Mn-doped TiO₂ nanoparticles exhibited the highest photodegradation efficiency 96%, within 180 minutes. It can be noted that the photocatalytic efficiency of 0.2% Mn-doped TiO₂, which measuring by UV-Vis spectroscopy and LC-MS measurement, results are nearly the same as shown in Figure 68.

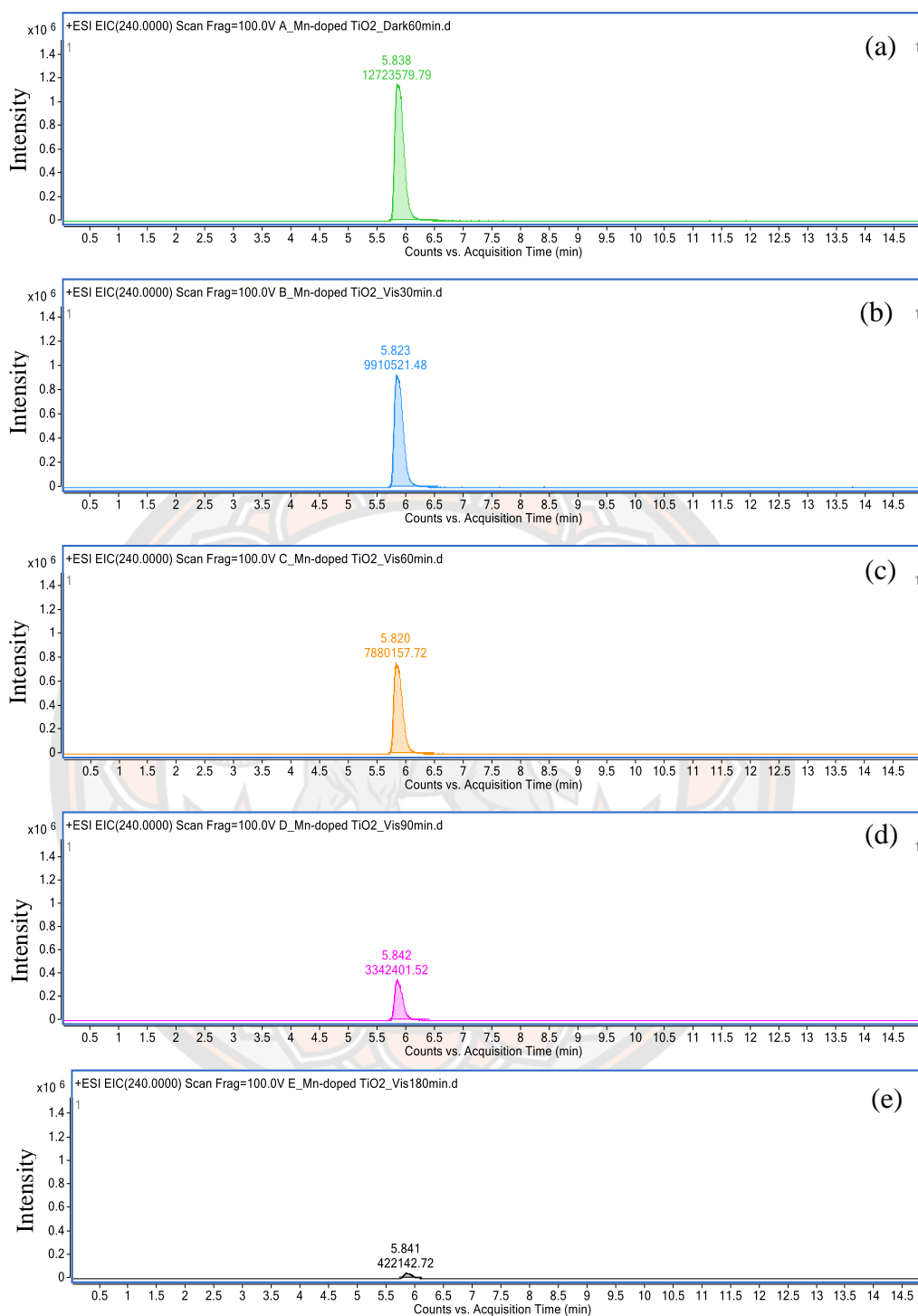
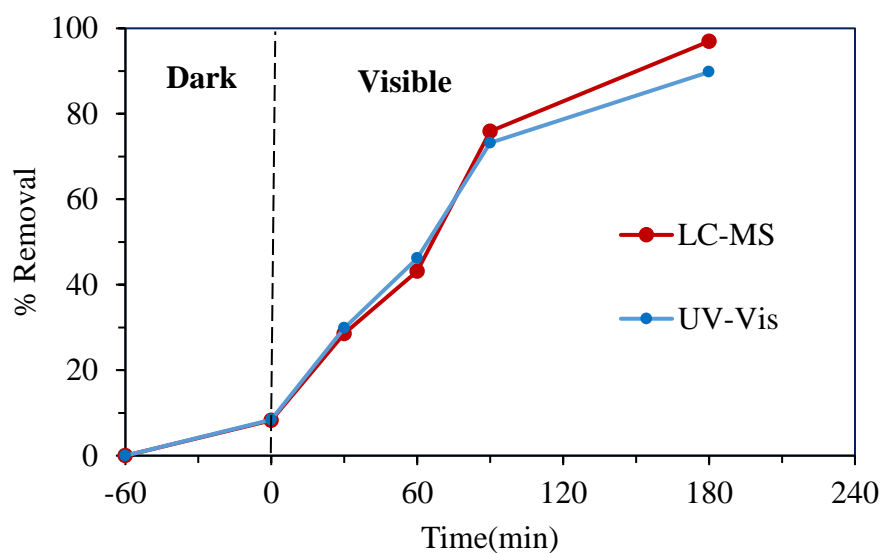


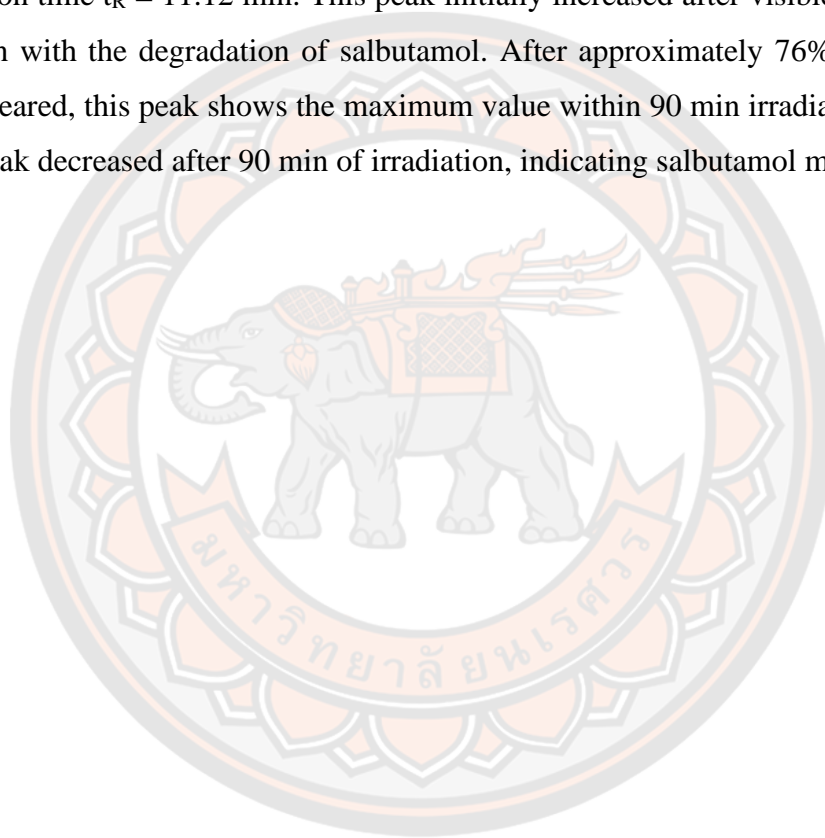
Figure 67 LC-MS chromatograms for peak area of SAL (a) in dark 60 min and after visible irradiation (b) 30, (c) 60, (d) 90, and (e) 180 min of 0.2% Mn-doped TiO₂.

Table 20 SAL degradation of 0.2% Mn-doped TiO₂ data by LC-MS measuring.

Time (min)	0.2% Mn-doped TiO ₂	
	Area	% Removal
-60	13,868,701.97	0.00
0	12723579.79	8.26
30	9910521.48	28.54
60	7880157.72	43.18
90	3342401.52	75.90
180	422142.72	96.96

**Figure 68** SAL degradation of the 0.2% Mn-doped TiO₂ under visible irradiation by LC-MS and UV-Vis spectroscopy measuring.

Liquid chromatography-mass spectrometry (LC-MS) was employed to study the intermediate products of salbutamol during photocatalytic degradation. Figure 69 presents the LC-MS chromatogram from the salbutamol solution taken during photocatalytic degradation experiments. It can be seen that the main peak at the retention time $t_R = 5.83$ min, due to salbutamol, decreases gradually and has a very small peak after 180 min. Other peaks appear during the degradation experiment, which can be assigned to the intermediates of the salbutamol degradation at the retention time $t_R = 11.12$ min. This peak initially increased after visible irradiation for 30 min with the degradation of salbutamol. After approximately 76% of salbutamol disappeared, this peak shows the maximum value within 90 min irradiation. However, this peak decreased after 90 min of irradiation, indicating salbutamol mineralization.



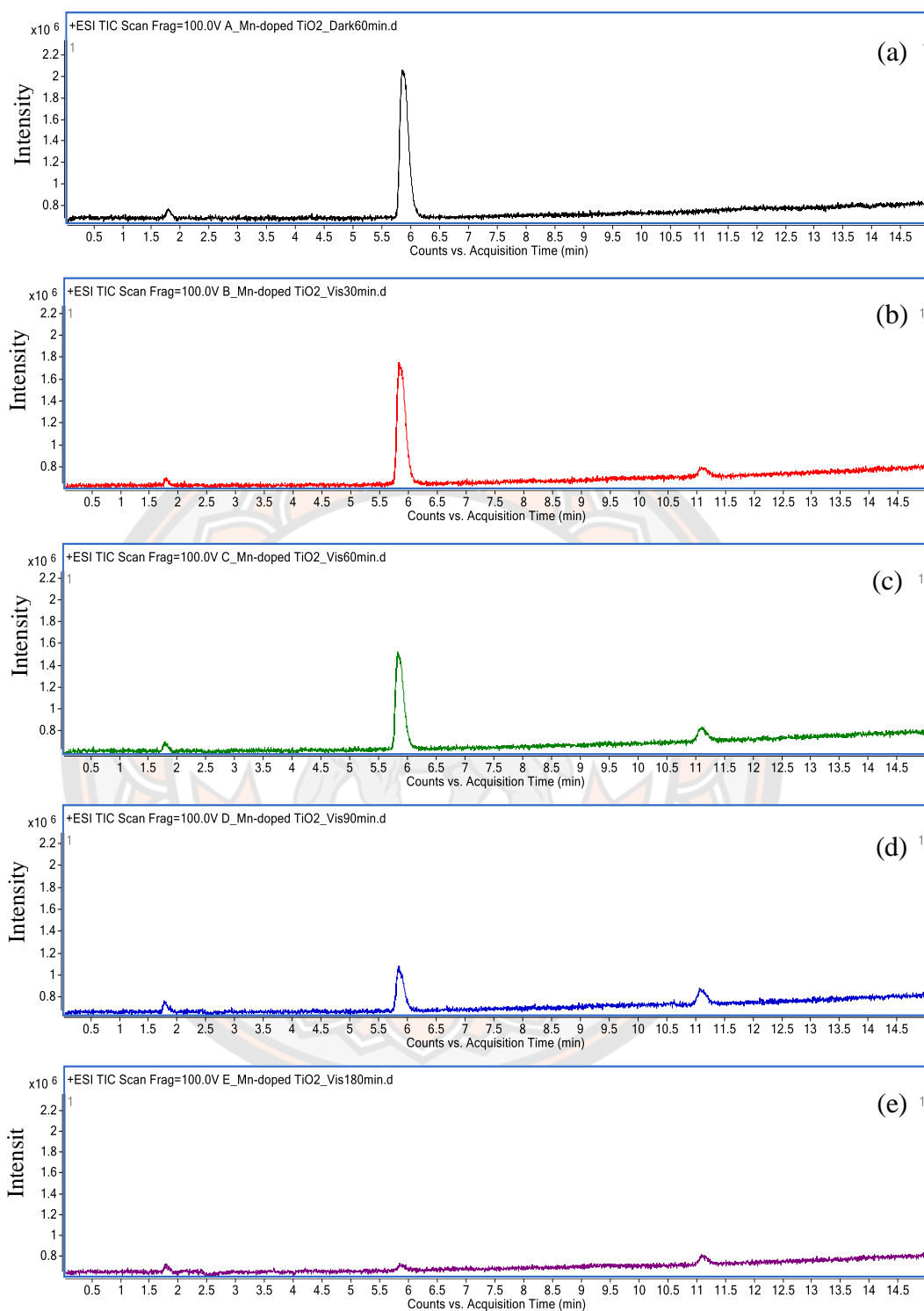


Figure 69 LC-MS chromatograms of SAL (a) in dark 60 min and after visible irradiation (b) 30, (c) 60, (d) 90, and (e) 180 min of 0.2% Mn-doped TiO₂.

The intermediate compounds of salbutamol degradation were determined by LC-MS. After dark adsorption, the product ions and protonated salbutamol was shown in Figure 70. The highest intensity (1.1×10^6) of protonated salbutamol was found at m/z 240. The protonated salbutamol was lost a water and formed the product ion at m/z 222; the latter was lost an isobutene and formed the product ion at m/z 166. The fragment ion m/z 148 was formed by the loss of a water from m/z 166. The fragment structures of salbutamol are listed in Figure 70. The intensity of protonated salbutamol at m/z 240 was decreased to 0.9×10^6 and 0.8×10^6 at 30 and 60 min irradiation times.

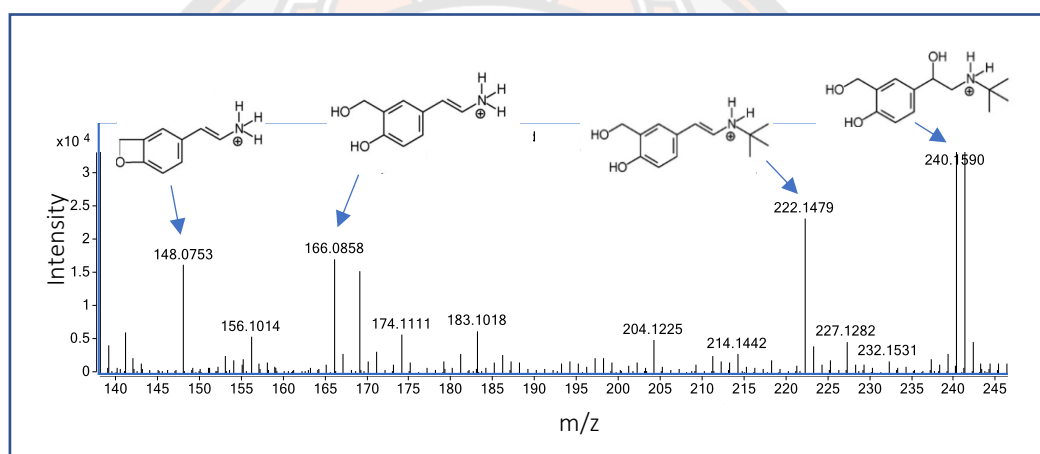
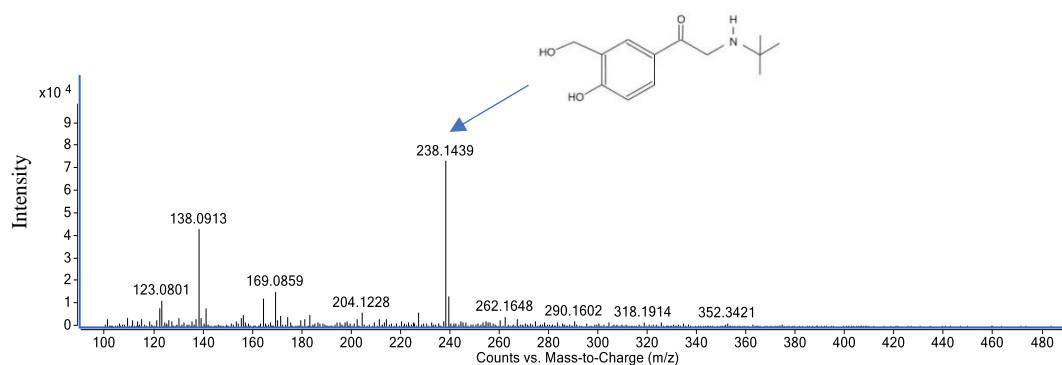
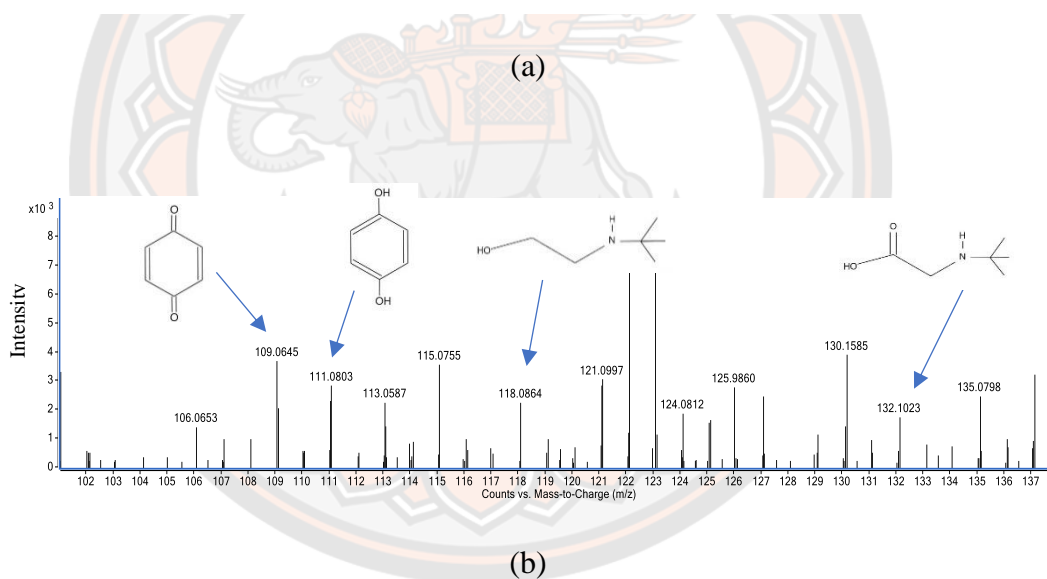
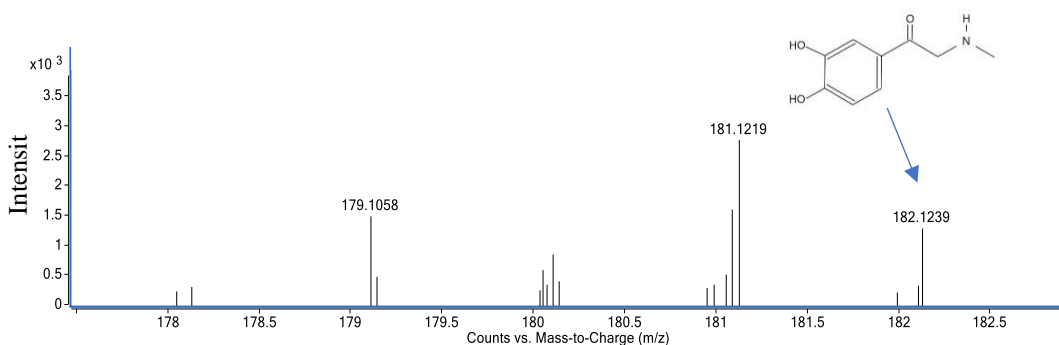


Figure 70 LC-MS spectra of salbutamol after dark adsorption

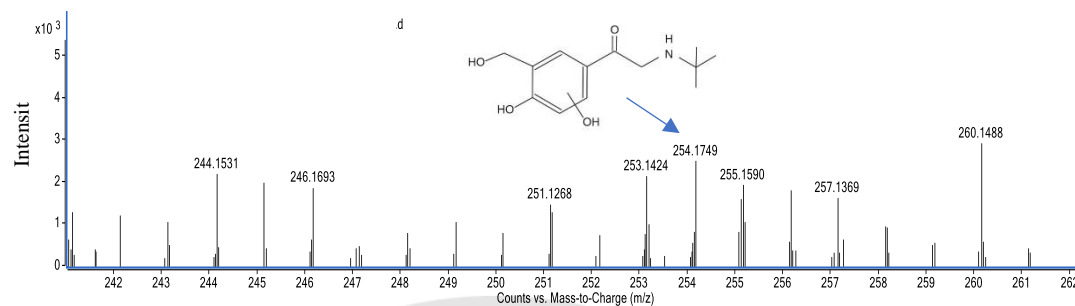
The protonated salbutamol was lost a methylic group to form the 2-(tert-butylamino)-1-(3,4-dihydroxyphenyl)ethanone at m/z 224 and it was then degraded into the species at m/z 182 which identified as 2-(methylamine)-1-(3,4-dihydroxyphenyl)ethanone. In addition, the lower molecular weights at m/z 109, 110, 118 and 132 was also observed and they were labelled to be 1,4-benzoquinone, hydroquinone, 2-(tert-butylamino)-ethanol and 2-(tert-butylamino)-acetic acid respectively (Sakkas et al., 2007).

The molecular ion at m/z 238 was recognized as 2-(tert-butylamino)-1-(4-hydroxyl-3-hydroxymethylphenyl)ethanone, which was transformed from the hydroxyl oxidation on the side chain of salbutamol (Zhou, Wang, Zhang, Ji, & Yang, 2017). Consequently, the product at m/z 254 was observed from the hydroxyl addition

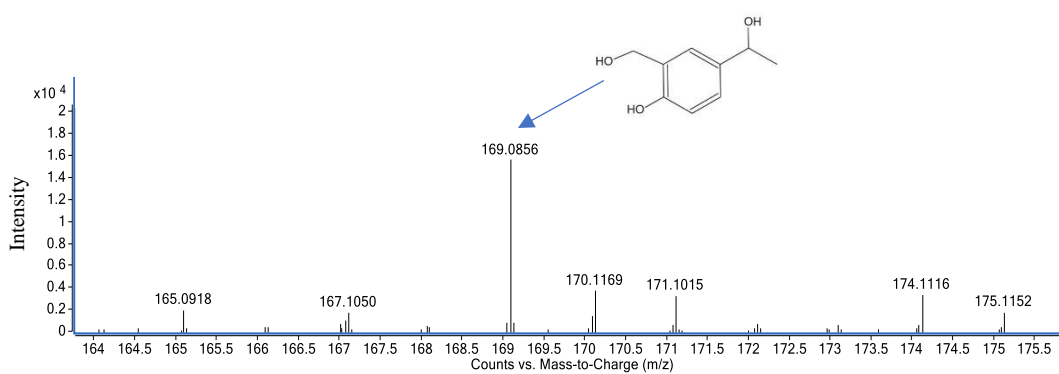
on the ring. The molecular ion at m/z 169 was detected as 1-(4-hydroxyl-3-hydroxymethylphenyl)ethanol which was due to the loss of tert-butylamino. The hydroxymethyl was then lost and the product of 1-(4-hydroxylphenyl)ethanol was generated at m/z 139. The observation of intermediate products during salbutamol photocatalytic degradation are listed in Figure 71 and summarized in Table 21.



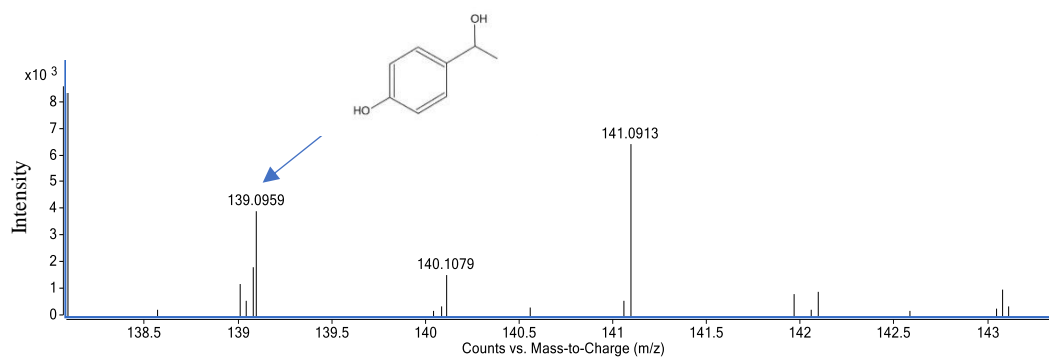
(c)



(d)



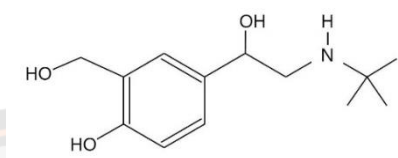
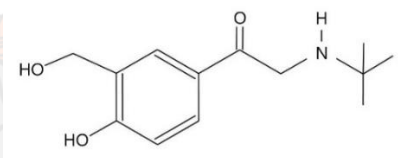
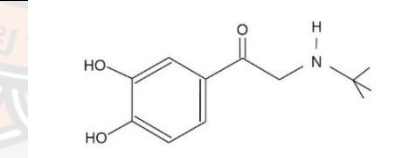
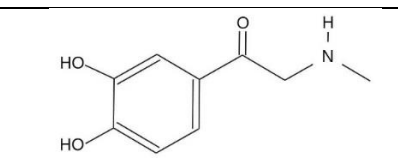
(e)

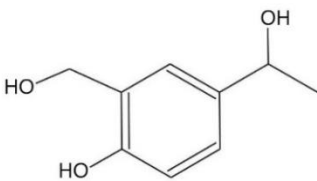
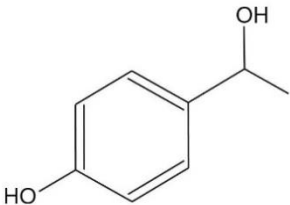
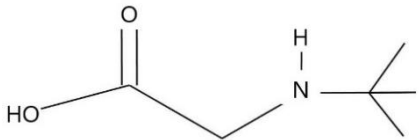



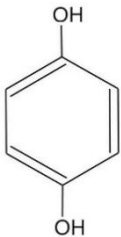

(f)

Figure 71 Mass spectrum of identified intermediates at various m/z fragments.

Table 21 Products during photocatalytic degradation of salbutamol.

m/z [M+H] ⁺	t _R (min)	Molecular weight (M _w)	Structure	Ref.
240	5.83	239	 <p>2-(tert-Butylamino)-1-(4-hydroxy-3-hydroxymethylphenyl)ethanol</p>	(Sakkas et al., 2007; Zhou et al., 2017)
238	11.08	237	 <p>2-(tert-Butylamino)-1-(4-hydroxy-3-hydroxymethylphenyl) ethanone</p>	(Zhou et al., 2017)
224	4.64	223	 <p>2-(tert-Butylamino)-1-(4-hydroxy-3-methylphenyl)ethanol</p>	(Sakkas et al., 2007)
182	4.68	181	 <p>2-(Methylamino)-1-(3,4-dihydroxyphenyl)ethanone</p>	(Sakkas et al., 2007)

m/z [M+H] ⁺	t _R (min)	Molecular weight (M _w)	Structure	Ref.
169	6.02	168	 <p>1-(4-hydroxyl-3-hydroxymethylphenyl)ethanol</p>	(Zhou et al., 2017)
139	10.36	138	 <p>1-(4-hydroxyphenyl)ethanol</p>	(Zhou et al., 2017)
132	4.73	131	 <p>2-(tert-Butylamino)-acetic acid</p>	(Sakkas et al., 2007)
118	6.03	117	 <p>2-(tert-Butylamino)-ethanol</p>	(Sakkas et al., 2007)

m/z [M+H] ⁺	t _R (min)	Molecular weight (M _w)	Structure	Ref.
111	12.46	110	 hydroquinone	(Sakkas et al., 2007)
109	11.63	108	 para benzoquinone	(Sakkas et al., 2007)

From all above results, the photocatalytic degradation of salbutamol involved the generation of intermediate compounds and their mineralization to carbon dioxide. The mineralization of intermediate products was verified by COD measurement; the COD concentration was approximately 77 mg/L after the dark adsorption and the concentration was decreased to 15.5 and 7.8 mg/L after 180 and 240 min irradiations respectively. The nitrogen in salbutamol molecule was eventually degraded to ammonium and nitrate ions (Sakkas et al., 2007). The potential photodegradation pathway of salbutamol is shown in Figure 72.

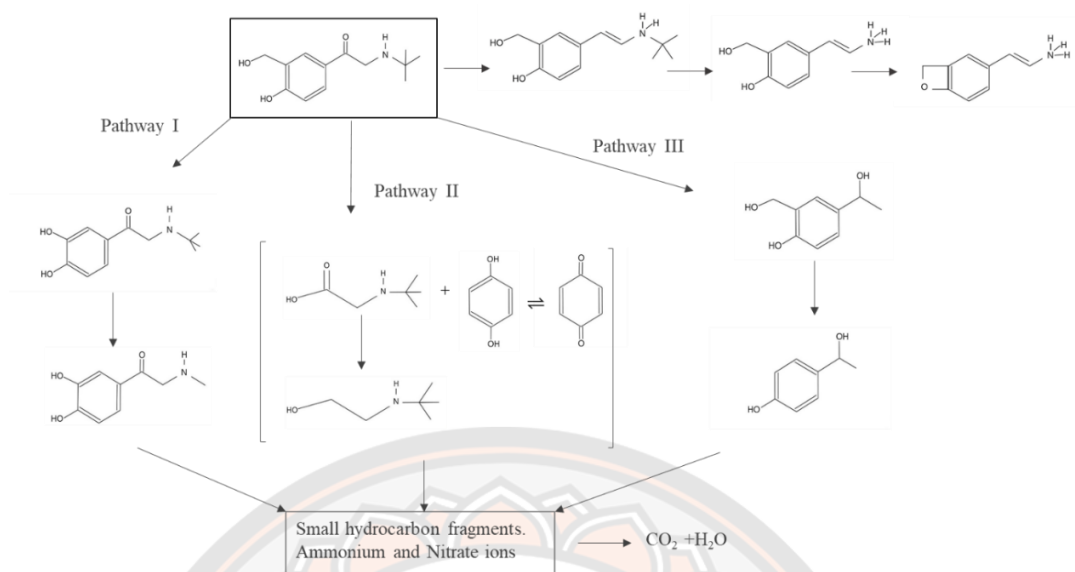


Figure 72 Possible photocatalytic degradation scheme of salbutamol.

4.7 Photokilling of Mn-doped TiO₂ nanoparticles

The photokilling activity of the undoped and Mn-doped TiO₂ nanoparticles was examined against *E. coli* under visible irradiation within 0, 1, 2, 3, and 4 hours, as shown in Figure 73. The results revealed that undoped and Mn-doped TiO₂ nanoparticles could inhibit *E. coli* under visible light. While the control sample, the bacterial culture without nanoparticles, the visible irradiation did not cause any bacteria death, as shown by the steady growth curve over the irradiation time. The results indicate that 0.2% Mn-doped TiO₂ nanoparticles are the best *E. coli* photokilling activity, completely killing *E. coli* under visible light within 4 hours. The undoped TiO₂ nanoparticles showed lower bacterial photokilling activity, including the lower Mn doping of 0.3 wt.% and 0.1 wt.% Mn-doped TiO₂ nanoparticles reduced *E. coli* photokilling activity. These results suggest that Mn doping enhanced the *E. coli* photokilling activity of TiO₂ nanoparticles. However, its photokilling activity will be good with Mn doping enough dosage. In addition, the photo of the visible *E. coli* colony after exposure to visible light is clearly shown in Figure 74.

Table 22 Average *E. coli* number of undoped and Mn-doped TiO₂ under visible light.

Time (min)	Log CFU/mL				
	Control	Undoped TiO ₂	0.1% Mn-doped TiO ₂	0.2% Mn-doped TiO ₂	0.3% Mn-doped TiO ₂
0	7.74	7.74	7.56	7.64	7.71
30	7.75	5.73	5.56	4.87	5.67
60	7.77	4.26	4.08	3.03	4.33
120	7.77	3.48	3.43	2.62	3.78
180	7.77	2.68	2.60	1.56	2.74
240	7.78	2.56	2.06	0.00	2.37

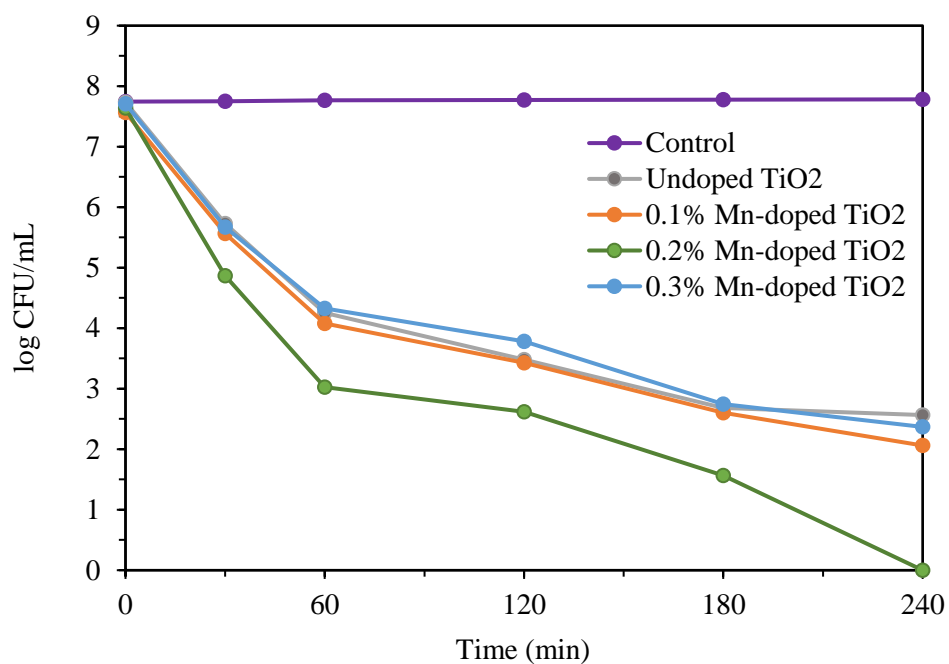


Figure 73 Antibacterial activity of undoped and Mn-doped TiO₂ nanoparticles.

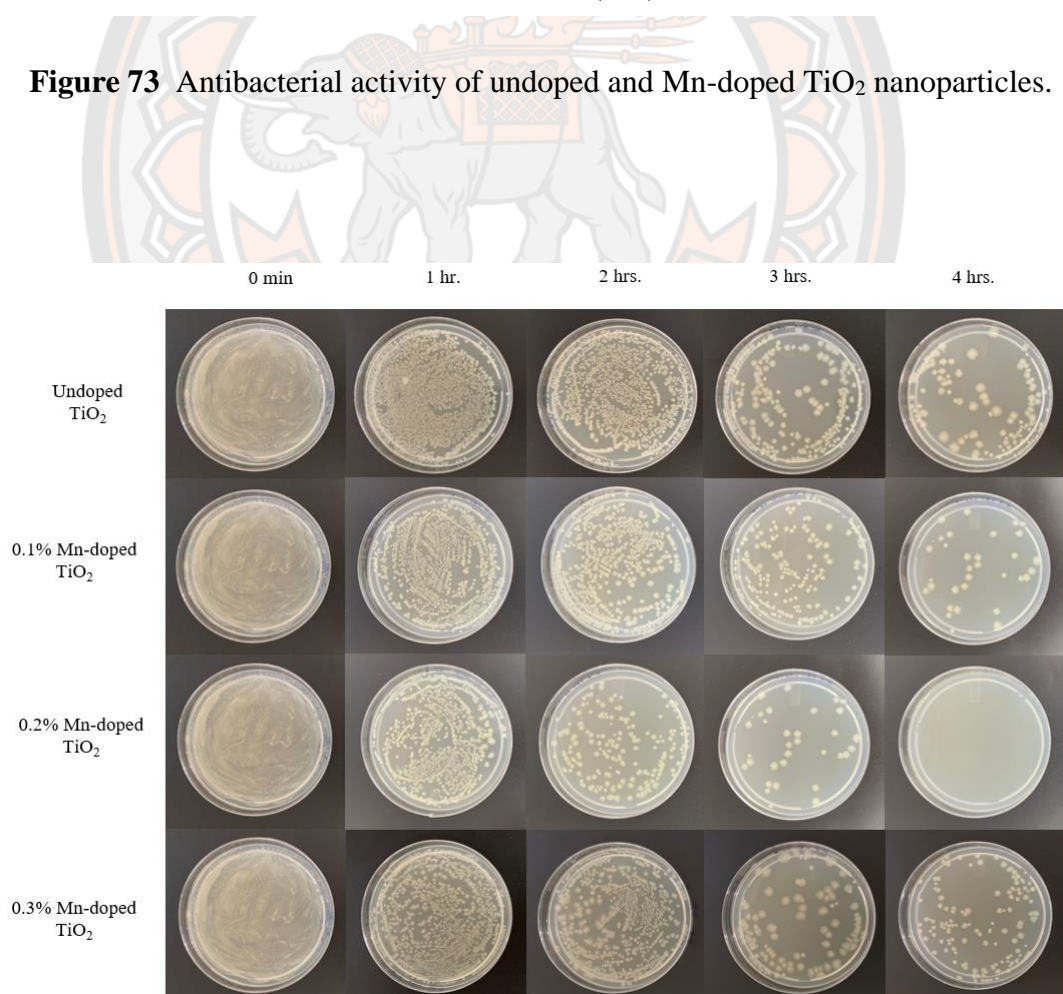


Figure 74 *E. coli* colony after visible irradiation of undoped and Mn-doped TiO₂.

CHAPTER V

CONCLUSIONS

The main objective of this research is to improve the photocatalytic degradation and antimicrobial activities of TiO₂ by doping Cu and Mn, ranging from 0.1 to 1.0% and 0.1 to 0.3%, respectively. The photocatalytic activity of the synthesized nanoparticles was investigated by measuring the degradation of dye (MB) and drugs (SAL) under UV-A and visible irradiation. For photokilling activity of the undoped and metal-doped TiO₂ nanoparticles was performed against *E. coli* under UV-A and visible irradiation. According to the results, the conclusion can be as the following.

The Cu-doped TiO₂ nanoparticles were synthesized by a hydrothermal method and characterized. In the XRD results, the Cu-doped TiO₂ nanoparticles exhibit the anatase phase in which the intensity peaks higher than undoped TiO₂. The CuO doping enhances the crystallinity and improves the structural quality of TiO₂. The TEM image of undoped and Cu-doped TiO₂ shows similar particle sizes of approximately 10 nm in agreement with the XRD results, which shows no difference in crystallite size between the undoped and TiO₂ nanoparticles. The specific surface area of Cu-doped TiO₂ nanoparticles contained a slightly lower surface area than the undoped TiO₂ nanoparticle at approximately 180-182 m²/g. In addition, the specific surface area was slightly decreased with increasing Cu percentages. However, the Cu-doped TiO₂ nanoparticles were agglomerated with increasing Cu doping contents shown in the SEM image. In addition, the band gap energy of TiO₂ was slightly reduced from 3.2 to 3.10 by Cu doping. However, the band gap of undoped and Cu-doped nanoparticles falls in the UV light region, indicating that all synthesized TiO₂ nanoparticles are active only under UV light irradiation.

The photocatalytic on MB degradation results indicate that the photocatalytic of TiO₂ can be improved by Cu doping. The results found that the highest photocatalytic activity was observed in the 0.1% Cu-doped TiO₂ nanoparticles under UV-A light, which showed MB degradation of approximately 100% under UV-A irradiation within 30 minutes. Furthermore, both undoped and Cu-doped TiO₂ nanoparticles demonstrated antibacterial and bactericidal activities. In comparison, the bacterial

culture without the nanoparticles and the UV-A irradiation did not cause any bacteria death. The best *E. coli* photokilling was observed in 0.1% Cu-doped TiO₂ nanoparticles, which showed complete killed in 180 minutes. The results concluded that the photokilling activity of TiO₂ nanoparticles could be improved by Cu doping.

On the other hand, the Mn-doped TiO₂ nanoparticles were synthesized using a sol-gel method. The anatase phase and rutile phase were observed on the undoped and Mn-doped TiO₂ nanoparticles. However, the major phase is the anatase phase and a very weak peak of the rutile phase was observed. The percentage of the rutile phase increase with Mn doping from ~10% to ~20%. These results indicate that the Mn doping content caused to change in the anatase-to-rutile transformation (ART). The Mn-doped TiO₂ nanoparticles contained a higher specific surface area than the undoped TiO₂ nanoparticles and the pore sizes and pore volume of Mn-doped TiO₂ nanoparticles also enlarged compared to the undoped TiO₂ nanoparticles. Due to the SEM image, there was no specific morphology changed from Mn doping. The narrow band gap energy of Mn-doped TiO₂ was observed; 2.91, 2.80, and 2.88 eV was for 0.1%, 0.2% and 0.3% Mn doping respectively. The band gap of Mn-doped TiO₂ nanoparticles fell in the visible light region, indicating that the nanoparticles were active under visible light irradiation.

The photocatalytic activity of Mn-doped TiO₂ nanoparticles indicated that the Mn-doped TiO₂ nanoparticles could effectively degraded MB and SAL under visible irradiation; the best photocatalytic activity was observed in 0.2% Mn-doped TiO₂ (of 97% MB removal in 60 minutes and 95% SAL removal in 180 minutes) and followed by 0.1% and 0.3% Mn-doped TiO₂ respectively. Similarly, the 0.2% Mn-doped TiO₂ obtained the best *E. coli* photokilling activity; the complete killing of *E. coli* was observed in 4 hours under visible light.

From this study, it can be seen that both Cu and Mn doping enhanced the photocatalytic activity of TiO₂ for various pollutants removal. The significant advantage of Cu and Mn doped TiO₂ nanoparticles was that the nanoparticles were able to active under lower energy requirement rather than pure TiO₂ such as UV-A and visible light. However, further study is necessary to develop a universal water treatment system using photocatalysis process and solar energy.

The suggestion of this thesis is to bring it to use as a real application, especially in Hospital wastewater, a primary source of pharmaceuticals and complex chemical composition which harmful to the environment and human health. It may be used as a pilot-scale treatment unit to treat the real wastewater effluents of hospitals.





REFERENCES

- Aini, N., Chasanah, S. N., Khalifah, S. N., Arifah, A., Prasetyo, A., & Suendo, V. (2019). *Preparation and Properties of TiO₂. 997V0. 003O2 Photocatalyst Supported on Indonesian Natural Zeolite Using Sonochemical Method*. Paper presented at the IOP Conference Series: Materials Science and Engineering.
- Ajiboye, T. O., Babalola, S. O., & Onwudiwe, D. C. (2021). Photocatalytic Inactivation as a Method of Elimination of E. coli from Drinking Water. *Applied Sciences*, *11*(3), 1313.
- Aksay, I., Alagna, L., Ali-Adib, Z., Angeloni, A., Armes, S., Arnold Jr, F., . . . Babushkin, O. Cumulative Author Index 1994. *Diamond*, *500*(145), 217.
- Almasi, A., Dargahi, A., Mohammadi, M., Azizi, A., Karami, A., Baniamerian, F., & Saeidimoghadam, Z. (2016). Application of response surface methodology on cefixime removal from aqueous solution by ultrasonic/photooxidation. *International journal of pharmacy and technology*, *8*(3), 16728-16736.
- Amalraj, A., & Pius, A. (2015). Photocatalytic degradation of monocrotophos and chlorpyrifos in aqueous solution using TiO₂ under UV radiation. *Journal of Water Process Engineering*, *7*, 94-101.
- Bayomie, O. S., Kandeel, H., Shoeib, T., Yang, H., Youssef, N., & El-Sayed, M. M. (2020). Novel approach for effective removal of methylene blue dye from water using fava bean peel waste. *Scientific reports*, *10*(1), 1-10.
- Bhati, I., Punjabi, P. B., & Ameta, S. C. (2010). Photocatalytic degradation of fast green using nanosized CeCrO₃. *Macedonian Journal of Chemistry and Chemical Engineering*, *29*(2), 195-202.
- Binas, V., Sambani, K., Maggos, T., Katsanaki, A., & Kiriakidis, G. (2012). Synthesis and photocatalytic activity of Mn-doped TiO₂ nanostructured powders under UV and visible light. *Applied Catalysis B: Environmental*, *113*, 79-86.
- Bound, J. P., & Voulvoulis, N. (2006). Predicted and measured concentrations for selected pharmaceuticals in UK rivers: implications for risk assessment. *Water research*, *40*(15), 2885-2892.
- Bubacz, K., Choina, J., Dolat, D., & Morawski, A. W. (2010). Methylene Blue and Phenol Photocatalytic Degradation on Nanoparticles of Anatase TiO₂. *Polish Journal of Environmental Studies*, *19*(4).
- Calamari, D., Zuccato, E., Castiglioni, S., Bagnati, R., & Fanelli, R. (2003). Strategic survey of therapeutic drugs in the rivers Po and Lambro in northern Italy. *Environmental science & technology*, *37*(7), 1241-1248.
- Chandra Sekhar, M., Purusottam Reddy, B., Prabhakar Vattikuti, S., Shanmugam, G., Ahn, C.-H., & Park, S.-H. (2018). Structural, magnetic, and catalytic properties of Mn-doped titania nanoparticles synthesized by a sol-gel process. *Journal of Cluster Science*, *29*(6), 1255-1267.
- Coico, R. (2006). Gram staining. *Current protocols in microbiology*(1), A. 3C. 1-A. 3C. 2.
- Cullity, B. D., & Graham, C. D. (2011). *Introduction to magnetic materials*: John Wiley & Sons.
- Damasceno, L., Ventura, R., Ortuño, J., & Segura, J. (2000). Derivatization procedures for the detection of β 2-agonists by gas chromatographic/mass spectrometric analysis. *Journal of mass spectrometry*, *35*(11), 1285-1294.

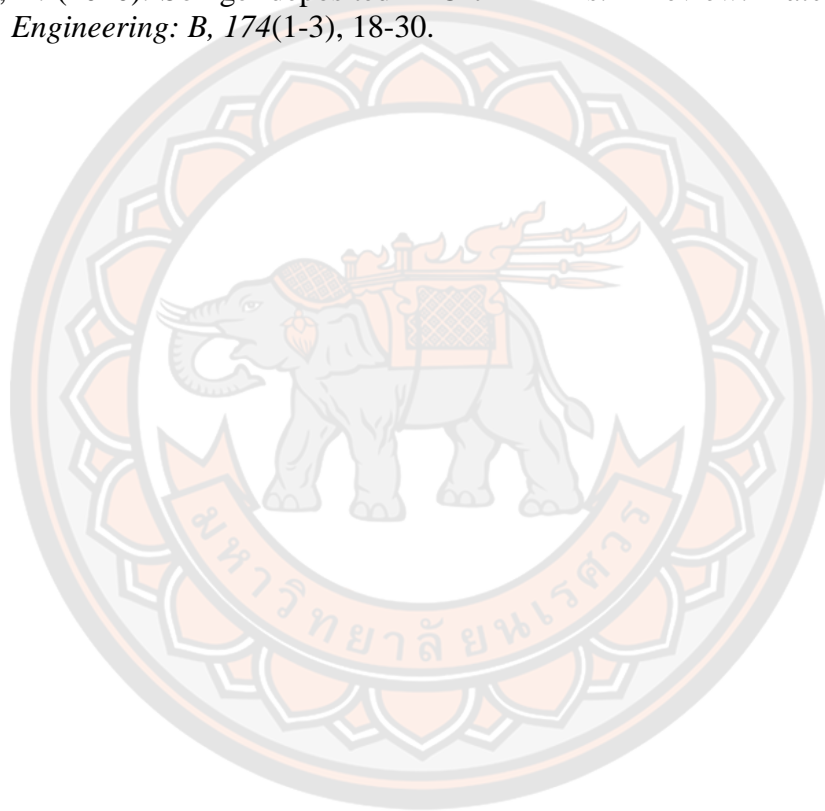
- De Vietro, N., Tursi, A., Beneduci, A., Chidichimo, F., Milella, A., Fracassi, F., . . . Chidichimo, G. (2019). Photocatalytic inactivation of *Escherichia coli* bacteria in water using low pressure plasma deposited TiO₂ cellulose fabric. *Photochemical & Photobiological Sciences*, 18(9), 2248-2258.
- Deng, Q., Xia, X., Guo, M., Gao, Y., & Shao, G. (2011). Mn-doped TiO₂ nanopowders with remarkable visible light photocatalytic activity. *Materials Letters*, 65(13), 2051-2054.
- Devi, L. G., Kumar, S. G., Murthy, B. N., & Kottam, N. (2009). Influence of Mn²⁺ and Mo⁶⁺ dopants on the phase transformations of TiO₂ lattice and its photocatalytic activity under solar illumination. *Catalysis Communications*, 10(6), 794-798.
- Ding, W., Wan, X., Zheng, H., Wu, Y., & Muhammad, S. (2021). Sulfite-assisted oxidation/adsorption coupled with a TiO₂ supported CuO composite for rapid arsenic removal: Performance and mechanistic studies. *Journal of Hazardous Materials*, 413, 125449.
- Dinh, V.-P., Le, H. M., Nguyen, V.-D., Dao, V.-A., Hung, N. Q., Tuyen, L. A., . . . Tan, L. (2019). Insight into the adsorption mechanisms of methylene blue and chromium (III) from aqueous solution onto pomelo fruit peel. *RSC advances*, 9(44), 25847-25860.
- Dodson, L. G., Vogt, R. A., Marks, J., Reichardt, C., & Crespo-Hernández, C. E. (2011). Photophysical and photochemical properties of the pharmaceutical compound salbutamol in aqueous solutions. *Chemosphere*, 83(11), 1513-1523.
- Frontistis, Z., Mantzavinos, D., & Meriç, S. (2018). Degradation of antibiotic ampicillin on boron-doped diamond anode using the combined electrochemical oxidation-Sodium persulfate process. *Journal of environmental management*, 223, 878-887.
- Ganesh, I., Gupta, A., Kumar, P., Sekhar, P., Radha, K., Padmanabham, G., & Sundararajan, G. (2012). Preparation and Characterization of Ni-Doped TiO₂ Materials for photocurrent and photocatalytic applications. *The Scientific World Journal*, 2012.
- Gnanasekaran, L., Hemamalini, R., Saravanan, R., Ravichandran, K., Gracia, F., & Gupta, V. K. (2016). Intermediate state created by dopant ions (Mn, Co and Zr) into TiO₂ nanoparticles for degradation of dyes under visible light. *Journal of Molecular Liquids*, 223, 652-659.
- Göbel, A., Thomsen, A., McArdeell, C. S., Joss, A., & Giger, W. (2005). Occurrence and sorption behavior of sulfonamides, macrolides, and trimethoprim in activated sludge treatment. *Environmental science & technology*, 39(11), 3981-3989.
- Gupta, V., Suhas, Ali, I., & Saini, V. (2004). Removal of rhodamine B, fast green, and methylene blue from wastewater using red mud, an aluminum industry waste. *Industrial & engineering chemistry research*, 43(7), 1740-1747.
- Hanaor, D. A., & Sorrell, C. C. (2011). Review of the anatase to rutile phase transformation. *Journal of Materials science*, 46(4), 855-874.
- Ikram, M., Umar, E., Raza, A., Haider, A., Naz, S., Ul-Hamid, d. A., . . . Ali, S. (2020). Dye degradation performance, bactericidal behavior and molecular docking analysis of Cu-doped TiO₂ nanoparticles. *RSC advances*, 10(41), 24215-24233.
- Jiang, Y., Li, F., Liu, Y., Hong, Y., Liu, P., & Ni, L. (2016). Construction of TiO₂ hollow nanosphere/g-C₃N₄ composites with superior visible-light photocatalytic

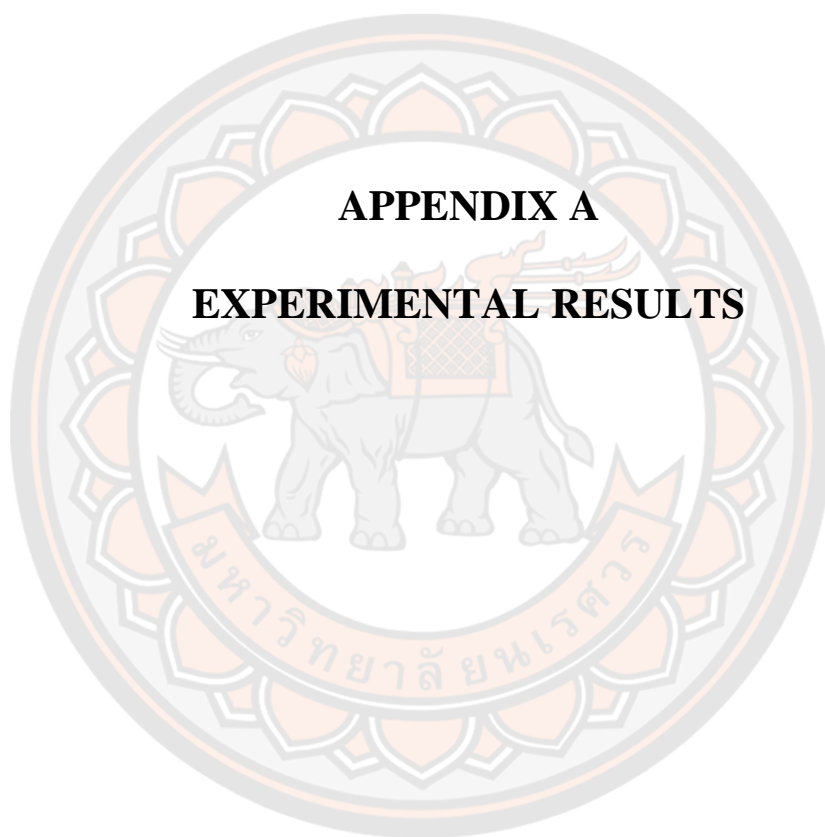
- activity and mechanism insight. *Journal of Industrial and Engineering Chemistry*, 41, 130-140.
- Kubelka, P., & Munk, F. (1931). A contribution to the optics of pigments. *Z. Tech. Phys*, 12(593), 193.
- Kümmerer, K. (2009). Antibiotics in the aquatic environment—a review—part I. *Chemosphere*, 75(4), 417-434.
- Le-Minh, N., Khan, S., Drewes, J., & Stuetz, R. (2010). Fate of antibiotics during municipal water recycling treatment processes. *Water research*, 44(15), 4295-4323.
- Lee, S. C., Hasan, N., Lintang, H. O., Shamsuddin, M., & Yuliati, L. (2016). *Photocatalytic removal of 2, 4-dichlorophenoxyacetic acid herbicide on copper oxide/titanium dioxide prepared by co-precipitation method*. Paper presented at the IOP Conference Series: Materials Science and Engineering.
- Li, J., Xu, Z., Liu, M., Deng, P., Tang, S., Jiang, J., . . . He, L. (2017). Ag/N-doped reduced graphene oxide incorporated with molecularly imprinted polymer: an advanced electrochemical sensing platform for salbutamol determination. *Biosensors and Bioelectronics*, 90, 210-216.
- Li, Z., Fang, Y., Zhan, X., & Xu, S. (2013). Facile preparation of squarylium dye sensitized TiO₂ nanoparticles and their enhanced visible-light photocatalytic activity. *Journal of Alloys and Compounds*, 564, 138-142.
- Loan, T. T., & Long, N. N. (2019). Influence of Mn⁽⁺²⁾ Doping on Structural Phase Transformation and Optical Property of TiO₍₂₎: Mn⁽⁺²⁾ Nanoparticles. *Communications in Physics*, 29(3), 251.
- López, R., & Gómez, R. (2012). Band-gap energy estimation from diffuse reflectance measurements on sol–gel and commercial TiO₂: a comparative study. *Journal of sol-gel science and technology*, 61(1), 1-7.
- Low, J., Cheng, B., & Yu, J. (2017). Surface modification and enhanced photocatalytic CO₂ reduction performance of TiO₂: a review. *Applied Surface Science*, 392, 658-686.
- Luna, A. L., Valenzuela, M. A., Colbeau-Justin, C., Vázquez, P., Rodriguez, J. L., Avendaño, J. R., . . . José, M. (2016). Photocatalytic degradation of gallic acid over CuO–TiO₂ composites under UV/Vis LEDs irradiation. *Applied Catalysis A: General*, 521, 140-148.
- Ma, J., Zhao, Q., Wei, D., Liu, H., Wang, X., Chen, Z., & Wang, J. (2019). Simple construction of core–shell MnO₂@ TiO₂ with highly enhanced U (vi) adsorption performance and evaluated adsorption mechanism. *Inorganic Chemistry Frontiers*, 6(4), 1011-1021.
- Mahapatra, K., Ramteke, D., & Paliwal, L. (2012). Production of activated carbon from sludge of food processing industry under controlled pyrolysis and its application for methylene blue removal. *Journal of Analytical and Applied Pyrolysis*, 95, 79-86.
- Miditana, S. R., Tirukkovalluri, S. R., Raju, I. M., Alim, S. A., Jaishree, G., & Chippada, M. (2021). Gemini surfactant assisted synthesis of mesoporous Mn/Mg bimetal doped TiO₂ nanomaterial: characterization and photocatalytic activity studies under visible light irradiation. *Sustainable Environment Research*, 31(1), 1-12.
- Nesbitt, H., & Banerjee, D. (1998). Interpretation of XPS Mn (2p) spectra of Mn

- oxyhydroxides and constraints on the mechanism of MnO₂ precipitation. *American Mineralogist*, 83(3-4), 305-315.
- Nguyen Thi Thu, T., Nguyen Thi, N., Tran Quang, V., Nguyen Hong, K., Nguyen Minh, T., & Le Thi Hoai, N. (2016). Synthesis, characterisation, and effect of pH on degradation of dyes of copper-doped TiO₂. *Journal of Experimental Nanoscience*, 11(3), 226-238.
- Nidheesh, P. V. (2017). Graphene-based materials supported advanced oxidation processes for water and wastewater treatment: a review. *Environmental Science and Pollution Research*, 24(35), 27047-27069.
- Nilsson, R., Nordlinder, R., Wass, U., Meding, B., & Belin, L. (1993). Asthma, rhinitis, and dermatitis in workers exposed to reactive dyes. *Occupational and Environmental Medicine*, 50(1), 65-70.
- Paul, S., Chetri, P., & Choudhury, A. (2014). Effect of manganese doping on the optical property and photocatalytic activity of nanocrystalline titania: Experimental and theoretical investigation. *Journal of Alloys and Compounds*, 583, 578-586.
- Prajapati, A. K., & Mondal, M. K. (2020). Comprehensive kinetic and mass transfer modeling for methylene blue dye adsorption onto CuO nanoparticles loaded on nanoporous activated carbon prepared from waste coconut shell. *Journal of Molecular Liquids*, 307, 112949.
- Rashad, M., Elsayed, E., Al-Kotb, M., & Shalan, A. (2013). The structural, optical, magnetic and photocatalytic properties of transition metal ions doped TiO₂ nanoparticles. *Journal of Alloys and Compounds*, 581, 71-78.
- Rauf, M. A., & Ashraf, S. S. (2012). Survey of recent trends in biochemically assisted degradation of dyes. *Chemical engineering journal*, 209, 520-530.
- Russo, V., Masiello, D., Trifuoggi, M., Di Serio, M., & Tesser, R. (2016). Design of an adsorption column for methylene blue abatement over silica: From batch to continuous modeling. *Chemical engineering journal*, 302, 287-295.
- Sakkas, V., Calza, P., Medana, C., Villioti, A., Baiocchi, C., Pelizzetti, E., & Albanis, T. (2007). Heterogeneous photocatalytic degradation of the pharmaceutical agent salbutamol in aqueous titanium dioxide suspensions. *Applied Catalysis B: Environmental*, 77(1-2), 135-144.
- Sangpour, P., Hashemi, F., & Moshfegh, A. Z. (2010). Photoenhanced degradation of methylene blue on cosputtered M: TiO₂ (M= Au, Ag, Cu) nanocomposite systems: a comparative study. *The Journal of Physical Chemistry C*, 114(33), 13955-13961.
- Serpone, N. (2006). Is the band gap of pristine TiO₂ narrowed by anion-and cation-doping of titanium dioxide in second-generation photocatalysts? In (Vol. 110, pp. 24287-24293): ACS Publications.
- Shannon, R. D. (1976). Revised effective ionic radii and systematic studies of interatomic distances in halides and chalcogenides. *Acta crystallographica section A: crystal physics, diffraction, theoretical and general crystallography*, 32(5), 751-767.
- Shao, G., Deng, Q., Wan, L., Guo, M., Xia, X., & Gao, Y. (2010). Molecular design of TiO₂ for gigantic red shift via sublattice substitution. *Journal of nanoscience and nanotechnology*, 10(11), 7092-7096.
- Sood, S., Umar, A., Mehta, S. K., & Kansal, S. K. (2015). Highly effective Fe-doped TiO₂ nanoparticles photocatalysts for visible-light driven photocatalytic

- degradation of toxic organic compounds. *Journal of colloid and interface science*, 450, 213-223.
- Ternes, T. A. (1998). Occurrence of drugs in German sewage treatment plants and rivers. *Water research*, 32(11), 3245-3260.
- Tseng, H.-C., & Chen, Y.-W. (2019). Facile synthesis of Ag/TiO₂ by Photoreduction method and its degradation activity of methylene blue under UV and visible light irradiation. *Modern Research in Catalysis*, 9(01), 1.
- Ullah, A., Zahoor, M., Din, W. U., Muhammad, M., Khan, F. A., Sohail, A., . . . Murthy, H. (2022). Removal of methylene blue from aqueous solution using black tea wastes: used as efficient adsorbent. *Adsorption Science & Technology*, 2022.
- Umar, K., Aris, A., Ahmad, H., Parveen, T., Jaafar, J., Majid, Z. A., . . . Talib, J. (2016). Synthesis of visible light active doped TiO₂ for the degradation of organic pollutants—methylene blue and glyphosate. *Journal of Analytical Science and Technology*, 7(1), 1-8.
- United, I. (2019). No time to wait—securing the future from drug-resistant infections. *Report to the Secretary General of the Nations*.
- Walthall, W., & Stark, J. (1999). The acute and chronic toxicity of two xanthene dyes, fluorescein sodium salt and phloxine B, to *Daphnia pulex*. *Environmental pollution*, 104(2), 207-215.
- Wang, H., Zhang, L., Chen, Z., Hu, J., Li, S., Wang, Z., . . . Wang, X. (2014). Semiconductor heterojunction photocatalysts: design, construction, and photocatalytic performances. *Chemical Society Reviews*, 43(15), 5234-5244.
- Wei, N., Cui, H., Song, Q., Zhang, L., Song, X., Wang, K., . . . Tian, J. (2016). Ag₂O nanoparticle/TiO₂ nanobelt heterostructures with remarkable photo-response and photocatalytic properties under UV, visible and near-infrared irradiation. *Applied Catalysis B: Environmental*, 198, 83-90.
- Wu, J., Li, C., Chen, X., Zhang, J., Zhao, L., Huang, T., . . . Zhou, X. (2017). Photocatalytic oxidation of gas-phase Hg⁰ by carbon spheres supported visible-light-driven CuO–TiO₂. *Journal of Industrial and Engineering Chemistry*, 46, 416-425.
- Wu, S. D., Zhu, Y. Q., Li, C., & Wei, Y. L. (2011). A novel CuO-TiO₂ composite photocatalyst and its degradation of methyl orange under UV irradiation. Paper presented at the Advanced Materials Research.
- Xu, B., Dong, L., & Chen, Y. (1998). Influence of CuO loading on dispersion and reduction behavior of CuO/TiO₂ (anatase) system. *Journal of the Chemical Society, Faraday Transactions*, 94(13), 1905-1909.
- Xue, M., Huang, L., Wang, J.-Q., Wang, Y., Gao, L., Zhu, J.-h., & Zou, Z.-G. (2008). The direct synthesis of mesoporous structured MnO₂/TiO₂ nanocomposite: a novel visible-light active photocatalyst with large pore size. *Nanotechnology*, 19(18), 185604.
- Yakob, Y., Naknun, K., Hirunmas, P., Dim, P. E., & Termtanun, M. (2021). Mo and Mn Co-doping for Isoproturon Degradation Under Visible Light. *Engineering Journal*, 25(2), 277-283.
- Yan, C., Yang, Y., Zhou, J., Liu, M., Nie, M., Shi, H., & Gu, L. (2013). Antibiotics in the surface water of the Yangtze Estuary: occurrence, distribution and risk assessment. *Environmental pollution*, 175, 22-29.

- Yang, L., Lin, Y., Jia, J., Xiao, X., Li, X., & Zhou, X. (2008). Light harvesting enhancement for dye-sensitized solar cells by novel anode containing cauliflower-like TiO₂ spheres. *Journal of Power Sources*, 182(1), 370-376.
- Yu, J., Hai, Y., & Jaroniec, M. (2011). Photocatalytic hydrogen production over CuO-modified titania. *Journal of colloid and interface science*, 357(1), 223-228.
- Zhang, G., Du, X., Wang, Y., Wang, H., Wang, W., & Fu, Z. (2017). Controllable synthesis of SnS₂ nanostructures with high adsorption and photocatalytic activities. *Materials Science in Semiconductor Processing*, 64, 77-84.
- Zhou, L., Wang, Q., Zhang, Y., Ji, Y., & Yang, X. (2017). Aquatic photolysis of β 2-agonist salbutamol: kinetics and mechanism studies. *Environmental Science and Pollution Research*, 24(6), 5544-5553.
- Znaidi, L. (2010). Sol-gel-deposited ZnO thin films: A review. *Materials Science and Engineering: B*, 174(1-3), 18-30.





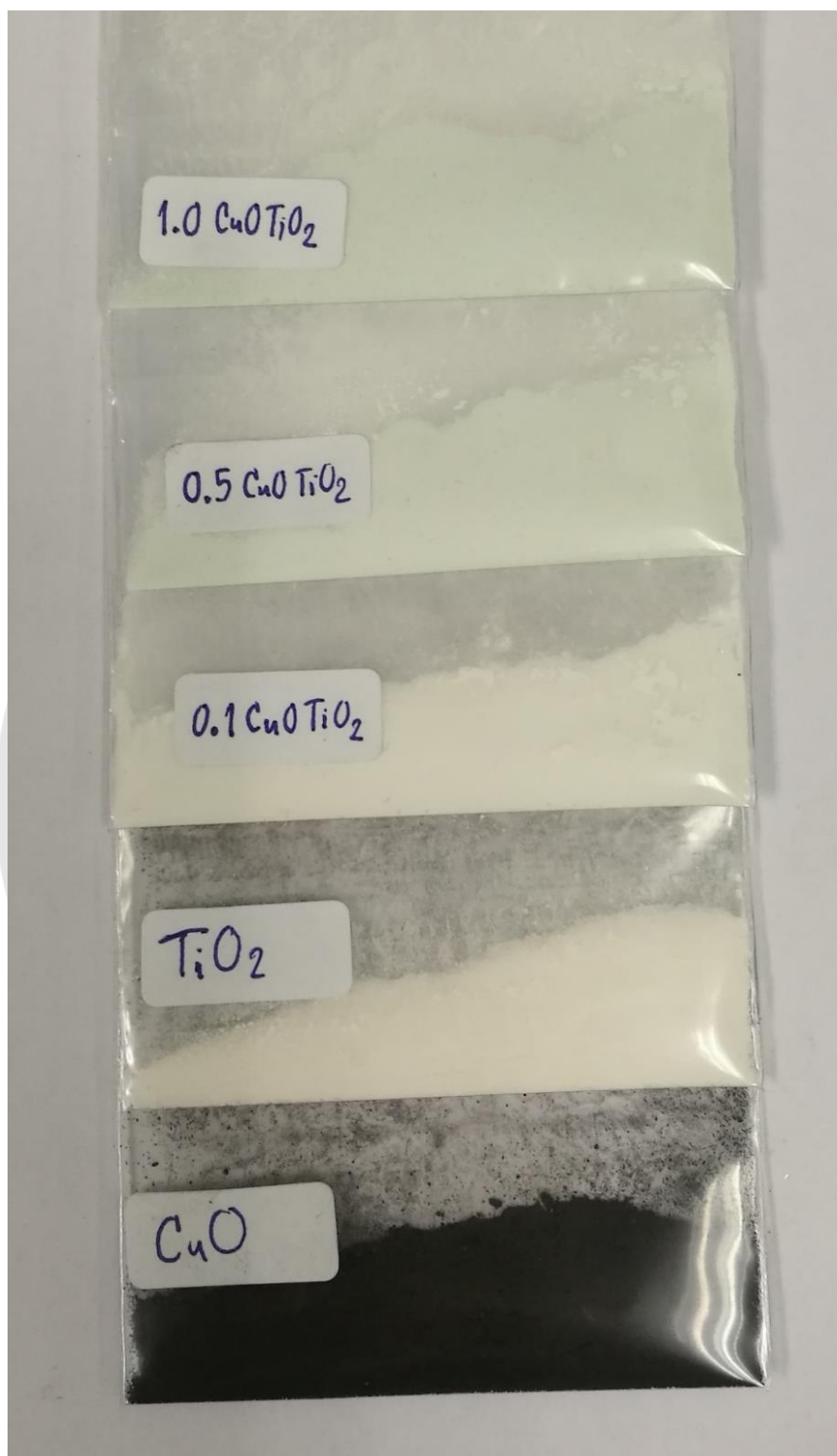


Figure 75 The powder of CuO, undoped and Cu-doped TiO₂ nanoparticles.

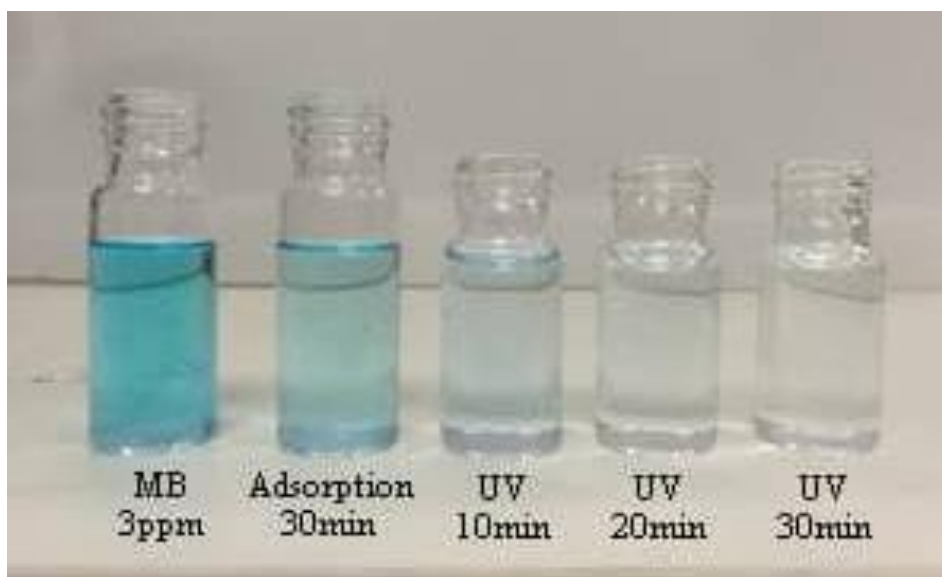


Figure 76 Photograph of the MB degradation color change of 0.1% Cu-doped TiO₂ after UV irradiation for various times.

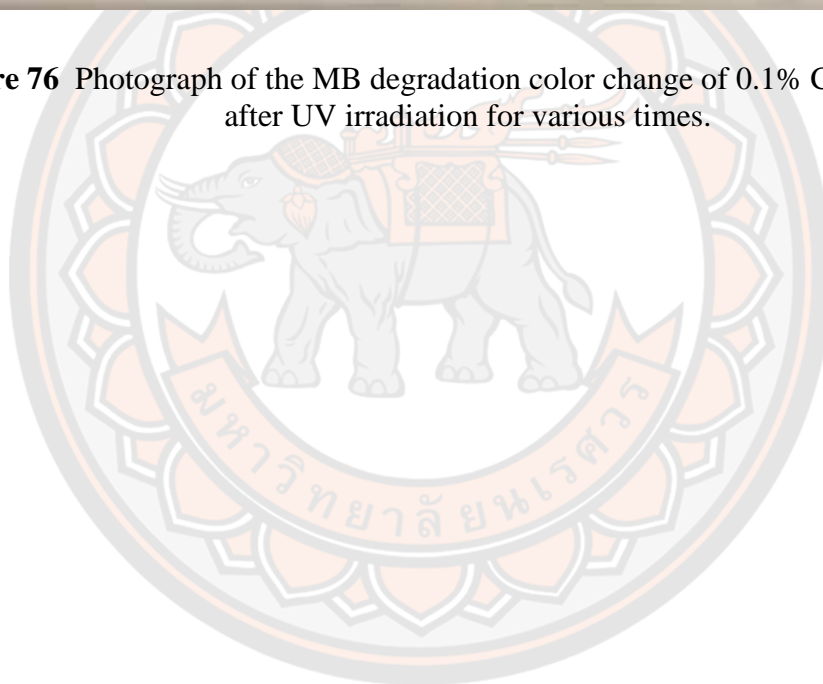
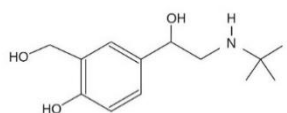
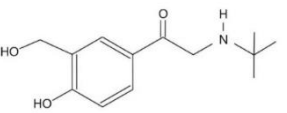
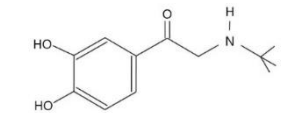
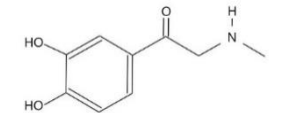
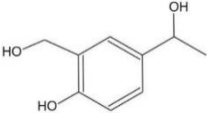
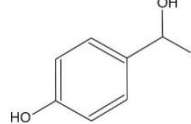
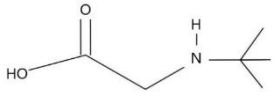




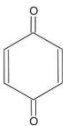


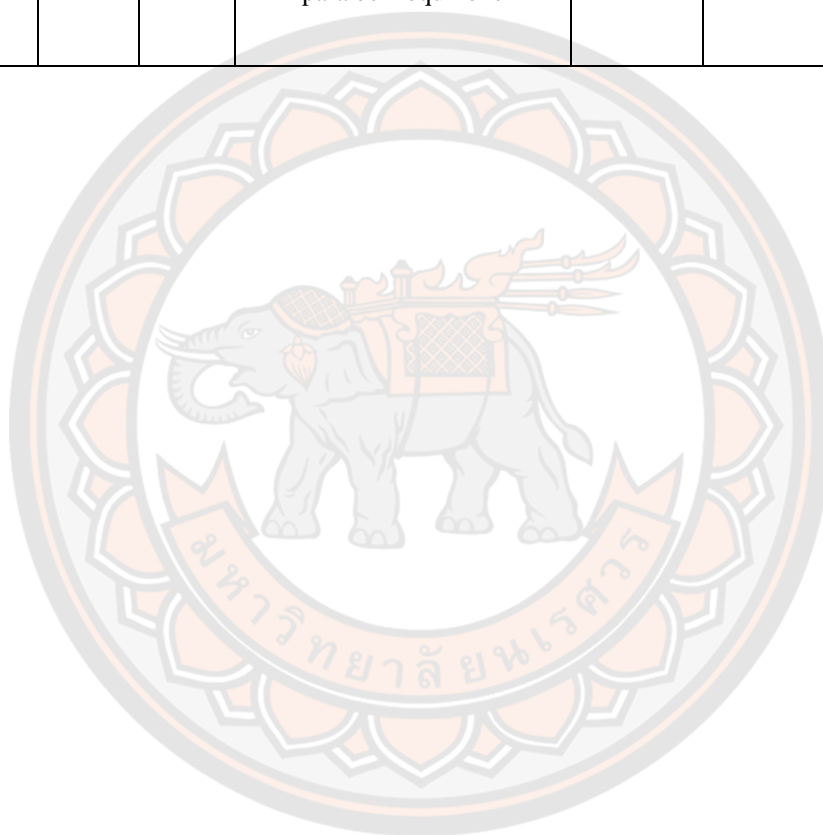
Figure 77 The powder of undoped and Mn-doped TiO_2 nanoparticles.

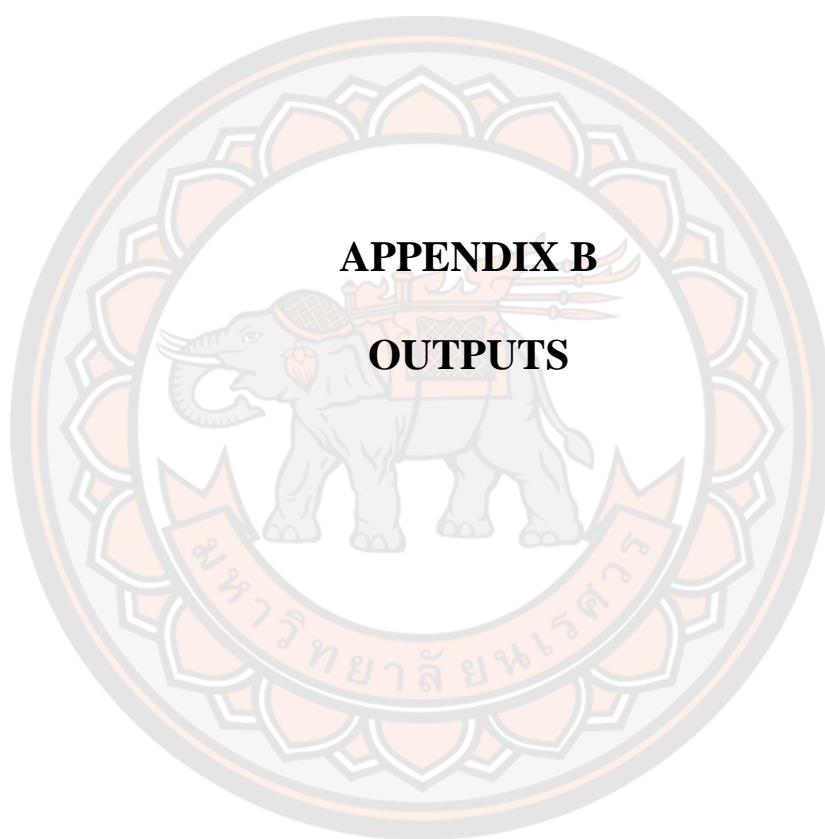
Table 23 The intensity of products during photocatalytic degradation of salbutamol.

m/z [M+H] ⁺	t _R (min)	M _w	Structure	Peak intensity		
				60 min	90 min	180 min
240	5.83	239	 2-(tert-Butylamino)-1-(4-hydroxyl-3-hydroxymethylphenyl)ethanol	8.0×10 ⁵	3.5×10 ⁵	0.5×10 ⁵
238	11.08	237	 2-(tert-Butylamino)-1-(4-hydroxyl-3-hydroxymethylphenyl)ethanone	1.1×10 ⁵	1.2×10 ⁵	0.8×10 ⁵
224	4.64	223	 2-(tert-Butylamino)-1-(4-hydroxyl-3-methylphenyl)ethanol	0.6×10 ³	0.7×10 ³	1.2×10 ³
182	4.68	181	 2-(Methylamino)-1-(3,4-dihydroxyphenyl)ethanone	2.5×10 ³	3.0×10 ³	4.0×10 ³

m/z [M+H] ⁺	t _R (min)	M _w	Structure	Peak intensity		
				60 min	90 min	180 min
169	6.02	168	 <p>1-(4-hydroxyl-3-hydroxymethylphenyl) ethanol</p>	1.3×10 ⁴	1.4×10 ⁴	1.5×10 ⁴
139	10.36	138	 <p>1-(4-hydroxyphenyl) ethanol</p>	4.0×10 ⁴	3.9×10 ⁴	4.1×10 ⁴
132	4.73	131	 <p>2-(tert-Butylamino)-acetic acid</p>	1.5×10 ³	1.2×10 ³	2.2×10 ³
118	6.03	117	 <p>2-(tert-Butylamino)-ethanol</p>	5.0×10 ³	3.0×10 ³	3.0×10 ³
111	12.46	110	 <p>hydroquinone</p>	3.0×10 ³	4.0×10 ³	2.0×10 ³

m/z [M+H] ⁺	t _R (min)	M _w	Structure	Peak intensity		
				60 min	90 min	180 min
109	11.63	108	 para benzoquinone	5.0×10 ³	4.0×10 ³	4.0×10 ³





Publication

- Y. Mingmongkol, D.T.T. Trinh, P. Phuinthiang, D. Channei, K. Ratananikom, A. Nakaruk, W. Khanitchaidecha. (2022). Enhanced Photocatalytic and Photokilling Activities of Cu-Doped TiO₂ Nanoparticles. *Nanomaterials*, 12, 1198
- Y. Mingmongkol, D.T.T. Trinh, P. Phuinthiang, D. Channei, A. Nakaruk, W. Khanitchaidecha. (2021). Decomposition of dye pigment via photocatalysis process using CuO- TiO₂ nanocomposite. *Materials Today: Proceedings*, 47, 3441-3444.
- Y. Mingmongkol, K. Ratananikom, D. Channei, A. Nakaruk, W. Khanitchaidecha. (2021). Effects of Aeration and Quantity of Effective Microorganisms (EM) Balls for Water Quality Restoration. *Naresuan University Engineering Journal*, 16(2), 18-23.
- Y. Mingmongkol, A. Polnok, P. Phuinthiang, D. Channei, K. Ratananikom, A. Nakaruk, W. Khanitchaidecha. (2022). Photocatalytic degradation of pharmaceutical agent salbutamol using visible driven Mn-doped TiO₂ (Preparation for reviewer)

Conference

- Y. Mingmongkol, Decomposition of dye pigment via photocatalysis process using CuO- TiO₂ nanocomposite, 5th International Conference on Smart Materials and Nanotechnology (SmartMat@2020), Pattaya, Thailand, 1- 4 December 2020, (Oral presentation)
- Y. Mingmongkol, Photocatalytic decomposition of cationic and anionic dyes over Mn-doped TiO₂, NRIC 18 Phitsanulok, Thailand, 26 July 2022 (Poster presentation)